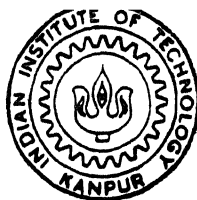


KINETIC SIMULATION OF MULTISPECIES FUSION PLASMAS

by

S. PANDIMANI



NUCLEAR ENGINEERING AND TECHNOLOGY PROGRAMME

INDIAN INSTITUTE OF TECHNOLOGY KANPUR

JUNE, 1994

KINETIC SIMULATION OF MULTISPECTRUM FUSION PLASMAS

A Thesis Submitted
in Partial Fulfilment of the Requirements
for the Degree of
DOCTOR OF PHILOSOPHY

By
S. PANDIMANI

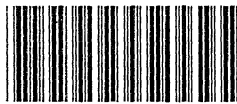
to the
NUCLEAR ENGINEERING AND TECHNOLOGY PROGRAMME
INDIAN INSTITUTE OF TECHNOLOGY, KANPUR
JUNE, 1994

27 JUN 1996

CENTRAL LIBRARY
KAMPUR

~~121720~~
Doc. No. A.

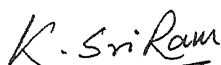
NETP-1994-D-PAN-KIN



A121720

Certificate

It is certified that the work contained in the thesis entitled "KINETIC SIMULATION OF MULTISPECIES FUSION PLASMAS", by S. Pandimani, has been carried out under our supervision and that this work has not been submitted elsewhere for a degree.



Prof. K. Sri Ram
Nuclear Engineering and
Technology Programme
Indian Institute of Technology
Kanpur, INDIA



Prof. M. S. Kalra
Nuclear Engineering and
Technology Programme
Indian Institute of Technology
Kanpur, INDIA

June 1994

Synopsis

Kinetic simulations based on the Boltzmann equation with Fokker-Planck collision term have been quite useful in modeling multispecies plasmas. Numerical simulations of fusion plasmas often deal with many ion species at different temperatures and also the electrons whose characteristic velocity and time scales are very different. Further, highly peaked non-Maxwellian distributions which arise out of auxiliary heating and reaction products are also encountered in the simulation of fusion plasmas. Such physical scenarios naturally add to complications in the numerical modeling process. Therefore it is desirable to represent different species including electrons on their characteristic velocity scales to facilitate the study of energy transfer, auxiliary heating, interaction with the fusion reaction products and of other physical situations of practical interest.

Fokker-Planck equations are solved to obtain the distribution functions, in general, by the finite difference method. Relatively less work has been done using finite element method for solving Fokker-Planck equations. Further, modeling species with highly peaked initial distributions, their subsequent interaction with other species and their evolution can be effectively dealt with by adapting the numerical grid. This leads to improvements in the accuracy of solutions, and in the calculation of such parameters as reactivities, etc.

Some of the contributions of the present work can be listed as given below:

1. Multi-velocity and time scale Fokker-Planck equations in 2-D velocity space (v, θ) , where v is the speed and θ the pitch angle, are introduced. These equations are derived by using individual velocity cut-offs for ions and electrons.

Therefore electrons can also be treated together with ions as a general species with less number of grid points.

2. Multispecies Fokker-Planck equations both in 1-D and 2-D are solved by Galerkin finite element method using conventional finite elements. Relative performance of various finite elements is studied. The Fokker-Planck equations are also solved by the finite difference method.
3. A method is presented to redistribute the nodes optimally on the numerical grid. Redistribution is based on the local discretization errors.
4. The Fokker-Planck collision operators which have singularities at the boundaries are approximated analytically.
5. The Fokker-Planck models are used to calculate reactivities $\langle \sigma v \rangle$ accurately during fast ion heating.

detailed outline of the present work is given in the following paragraphs.

Chapter 1 presents a review of literature on the numerical solution of Fokker-Planck equations. A significant amount of work reported in literature is on the finite difference method rather than on the finite element approach. A brief review of the area of optimal node distribution is also presented. Further, some studies relating to the $\langle \sigma v \rangle$ calculations and source and loss mechanisms that have been considered in the simulations are also reviewed briefly. This chapter ends with an outline of the work presented in subsequent chapters.

Chapter 2 contains the governing equations and approximation of collision operators at the boundaries. Multispecies Fokker-Planck equations in (v, θ) co-ordinates are written in their general form. These equations are recast into a dimensionless form by using velocity and time constants which are chosen based on the characteristic velocity and time scales of different species. This formulation facilitates the treatment of electrons as a general species with the same computational effort. In the case of Maxwellian background species, the Fokker-Planck coefficients are presented in their simplified forms. The singularities present in the collision operators

at the boundaries ($v = 0$, $\theta = 0$ and π) are removed analytically. One-dimensional Fokker-Planck equations as derived from the 2-D equations are also presented.

Chapter 3 is concerned with numerical solutions of multispecies 1-D Fokker-Planck equations. The equations are first solved by the Galerkin finite element method with the standard isoparametric finite elements namely, the linear, quadratic and cubic elements. Time stepping is done by the one step Θ -methods ($\Theta = 1/2$ – Crank-Nicolson method, $\Theta = 1$ – Backward implicit method). Computational aspects pertaining to the Fokker-Planck coefficients, use of higher order quadrature, velocity scale refinement, time step control strategy etc. are discussed. The spatial and temporal convergence of various finite elements and the time stepping schemes are studied. The results show that the quadratic and cubic elements are better than the linear elements in terms of accuracy and convergence. Multispecies calculations include treating electrons as a general species. The advantage of using multi-velocity scales is emphasized. Further, the 1-D Fokker-Planck equations are solved by the finite difference method. Their solutions are compared with finite element solutions. The collision operator without singularity at $v = 0$ is also implemented. The results indicate that the analytical approximation improves the accuracy of the solutions at the boundary $v = 0$.

Chapter 4 deals with 1-D finite difference approach mainly from the view point of optimal distribution of grid points. The node redistribution is intended to reduce the maximum of local discretization error. Higher order approximations for the derivatives are also considered and compared with standard central finite difference discretization. The discretization errors are compared with the exact values for some initial distributions. It is found that the maximum errors for Maxwellian and Gaussian distributions can be reduced considerably by (in most cases by more than an order of magnitude) the redistribution of nodes. The grid redistribution is illustrated with the relaxation of a Gaussian distribution to Maxwellian at various time intervals.

Chapter 5 is mainly on the numerical solution of Fokker-Planck equations in 2-D, (v, θ) space. First, the equations are solved by the Galerkin finite element method using five different types of quadrilateral elements, viz. linear, complete quadratic and cubic, and incomplete quadratic and cubic elements. Relative merits of these

ments are investigated. As in 1-D, the time stepping is done by the one step methods. Secondly, for purpose of comparison and to study the implementation of the analytical approximation at the boundaries, the finite difference approach is used. For this case Alternating Direction Implicit time stepping scheme is also included.

Chapter 6 consists of some studies related to the simulation of D-T fusion plasmas. Emphasis is on the calculation of $\langle \sigma v \rangle$ accurately under non-Maxwellian conditions arising out of fast ion heating scenarios. An improved reaction loss model which correctly calculates the particle losses due to fusion reactions at different energies is implemented. Loss and source mechanisms considered in the simulation include reacting particle losses and the reaction source for α 's. The transfer of energy from α particles to background plasma is studied taking into account the α - α interaction.

Finally, Chapter 7 summarizes the results presented in the previous chapters and ends with some observations and suggestions for the extension of the present work.

Acknowledgements

With immense pleasure and great respect, I express my deep sense of gratitude to Professors M. S. Kalra and K. Sri Ram for their invaluable guidance and encouragement. Their constant support and patience which sustained throughout my research made this thesis possible. The knowledge they imparted to me is indeed invaluable. They gave me complete freedom with a pleasant working environment and unrestricted access to all the laboratory facilities. My sincere thanks to their family members also.

I dutifully acknowledge the help and advice of Prof. Prabhat Munshi who acted as a friend and counsellor throughout my stay at IITK. My heartiest thanks to him. I also thank Prof. A. Sengupta for his association and concern.

Special thanks are due to Profs. R. Sethuraman and T. Sundararajan for their timely help and assistance. They offered very useful suggestions in some parts of the thesis.

I place on record with deep satisfaction the help rendered by Drs. Velusamy (IGCAR), M. R. Balakrishnan (BARC), Rajashankar (SERC), and Sampath Kumar in getting some useful literature.

My colleagues Krishna Mohan and Manmohan deserve special mention for their support and understanding which helped me in many ways. I strongly appreciate their willingness to help whenever asked for.

It is a pleasure to acknowledge the care and affection extended to me by the NET family members — Messrs Pathak, Tomar, Yadav, Gopal, Mohsin, and Prasad. My heartiest thanks to all of them.

Words are not sufficient to express my thankfulness to all my friends who made my stay at IITK indeed memorable. My special thanks to Ravi, Venki, Sampath,

Uma Mahesh, Guruprem, Karunakaran, Srikanth and Kishore for their help in the final preparation of the thesis.

The research work was partially supported by the Department of Science and Technology, Govt. of India under the SRPP scheme. The assistance provided by IIT – Kanpur is also gratefully acknowledged.

Last but not the least, with profound feelings and respect, I sincerely thank my parents, sisters, and brothers for giving me the freedom to pursue my career in research. Their adorable patience and encouragement will remain with me for ever.

— *Pandimani*

To My Parents

Contents

List of Figures	xvii
List of Tables	xxi
1 Introduction	1
1.1 Motivation and Objectives	1
1.2 Numerical solution of Fokker-Planck equations	3
1.3 Adaptive Node Distribution	7
1.4 Outline of the Thesis	9
2 Governing Equations and Boundary Singularities	11
2.1 Introduction	11
2.2 Basic Equations	12
2.2.1 Preliminaries	12
2.2.2 Basic Equations in 2-D Velocity Space	14
2.2.3 Rosenbluth Potentials and Legendre Polynomials	15
2.3 Fokker-Planck Equations in Nondimensional Form	17
2.3.1 Fokker-Planck Equations	19
2.3.2 Background Species	26
2.4 Fokker-Planck Equations in One Dimension	27
2.5 Collision Operators without Boundary Singularities	29
2.5.1 1-D Operator	30
2.5.2 2-D Operator	31
2.6 Summary	35

3	One Dimensional Fokker-Planck Equations	37
3.1	Introduction	37
3.2	Finite Element Method	38
3.2.1	Galerkin Formulation for 1-D Equations	38
3.2.2	Computation of Element Matrices	42
3.2.3	Time Integration	43
3.3	Computation of Fokker-Planck Coefficients	45
3.3.1	Numerical Quadrature and Interpolation	46
3.3.2	Comparison of Accuracy	47
3.4	Convergence	48
3.4.1	Error Norms and Test Input	48
3.4.2	Spatial and Temporal Convergence	50
3.5	Computational Aspects	55
3.5.1	Density and Energy Conservation	55
3.5.2	Controlling the Time Step	56
3.5.3	Velocity Scale Refinement	57
3.5.4	Structure of the Program	61
3.6	Finite Difference Solutions	62
3.6.1	One Step Θ -Method of Solution	63
3.6.2	Approximation on the Boundary	64
3.7	Treating Electrons as a General Species	67
3.8	Summary	75
4	Discretization Errors and Optimal Distribution of Nodes	77
4.1	Introduction	77
4.2	Error Estimates	78
4.3	Redistribution of Nodes	79
4.4	Exact and Computed Errors	80
4.5	Comparison of Errors for Ions and Electrons	88
4.6	Interpolation and Quadrature Errors	90
4.7	Adaptive Time Stepping Based on Energy Error	90
4.8	Summary	95

5	Numerical Solution of 2-D Fokker-Planck Equations	97
5.1	Introduction	97
5.2	Finite Element Solution in 2-D	98
5.2.1	Formulation	98
5.2.2	Evaluation of Element Matrices and Coefficients	102
5.3	Accuracy and Numerical Results	105
5.3.1	Error Indicators and Relaxation Norms	105
5.3.2	Performance of the Quadrilateral Finite Elements	106
5.4	Finite Difference Solutions	111
5.4.1	Θ -method of Solution in 2-D	113
5.4.2	Alternating Direction Implicit Method	117
5.5	Background Species and Energy Transfer	120
5.5.1	Fixed Background Species	120
5.5.2	Energy Transfer between the Species	120
5.6	Summary	124
6	Fusion Reactivities and Fast Ion Interactions	127
6.1	Introduction	127
6.2	Reaction Losses	128
6.2.1	Killeen's Model	128
6.2.2	Improved Model	129
6.3	Fast Ion Source(s)	132
6.3.1	Fast Ions	132
6.3.2	Reaction Products	135
6.4	Particle Loss	138
6.5	Energy Loss	140
6.6	Summary	141
7	Concluding Remarks	145
7.1	Summary and Conclusions	145
7.2	Observations and Suggestions	148
	Bibliography	151

A Legendre Polynomials and their Derivatives	159
B Finite Element Shape Functions	163

List of Figures

2.1	Maxwellian distributions for different species	20
3.1	One dimensional finite elements	39
3.2	L_∞ and L_2 relaxation norms for a Gaussian at 6τ for different grid spacings	52
3.3	L_∞ and L_2 relaxation norms for a Gaussian at 6τ for different time steps	53
3.4	Equipartition of energy between deuterons and tritons using different velocity scales	55
3.5	Comparison of numerical errors in the finite element and finite difference methods	66
3.6	e_∞ and e_{rms} errors of numerical and analytical approximations at the boundary for a Maxwellian.	67
3.7	e_∞ and e_2 errors of ions and electrons for a Maxwellian input	69
3.8	Energy transfer from deuterons to electrons at low temperatures . .	72
3.9	Energy transfer from electrons to ions at low temperatures	73
3.10	Energy transfer between ions and electrons–Finite element method .	74
3.11	Energy transfer between ions and electrons–Finite difference method	75
4.1	Comparison of discretization errors for a Maxwellian distribution on uniform and optimal grids using standard three-point central difference formula	81

4.2	Comparison of discretization errors for a Maxwellian distribution on uniform and optimal grids using a five-point difference formula based on Lagrangian polynomials	81
4.3	Discretization errors for a Gaussian distribution on a uniform and optimal grid with 101 nodes	82
4.4	Optimal distribution of nodes for two different distribution functions (101 nodes)	83
4.5	Comparison of exact and estimated errors for a Maxwellian distribution using central differences	84
4.6	Exact and estimated errors for a Maxwellian distribution using five-point difference formula	85
4.7	Comparison of exact and estimated errors for a Gaussian distribution using central differences	85
4.8	Exact and estimated errors for a Gaussian distribution using higher order difference formulae	86
4.9	Variation of L_{max} error with grid spacing: (U) Uniform grid, (O) Optimal grid	87
4.10	Comparison of discretization errors for a Maxwellian distribution with a large velocity cut-off	88
4.11	Comparison of discretization errors for ions and electrons: (a) & (b) - Standard central difference, (c) & (d) - five-point difference formulae	89
4.12	Optimal distribution of nodes for the evolution of a Gaussian at different times	91
5.1	Finite element computational domain and various types of quadrilateral finite elements	99
5.2	Spatial convergence of various types of quadrilateral finite elements .	108
5.3	Temporal convergence of the quadrilateral finite elements	109
5.4	The distribution of fractional negative values of f in a 2-D evolution	111
5.5	The distribution of fractional negative values of f in a 1-D multi-species problem	112

5.6	Comparison of numerical errors using different boundary approximations	116
5.7	Energy loss from a general species in the presence of a fixed background species	121
5.8	Energy transfer between general species and a varying background species	123
5.9	Energy transfer between ions and electrons	124
6.1	Reaction loss coefficients of fuel ions in D-T and D- He^3 plasmas . .	130
6.2	Distribution function with a tail	131
6.3	Loss coefficients for fuel ions for non-Maxwellian f	132
6.4	Distributions of fast ions and electrons in a D-e plasma	134
6.5	Distribution functions at 1.5 s in the presence of reaction products .	137
6.6	Variation in density and energy for a single species with particle sink	139
6.7	Distribution function of deuterons in the presence of particle sink . .	140
6.8	Variation in energy of the species (bulk+fast) in the presence of sinks	142

List of Tables

3.1	Fokker-Planck coefficient A_a obtained by using different integration schemes (S)– E-Error function, T-Trapezoidal and H-Hermite	47
3.2	Relaxation measures in percent of a Gaussian at 10τ with different finite elements and time stepping schemes ($\Delta\tau = 1/16$, L-Linear, Q-Quadratic and C-Cubic)	51
3.3	Percent errors due to numerical evolution for the species T in a multispecies calculation at 6τ	54
3.4	Negative values in the spectrum for common and multi-velocity scale models (L-Linear, Q-Quadratic, C-Cubic, and N-Number of nodes) .	59
3.5	Energy of deuterons at 0.5 s in a D-T plasma obtained by using various finite elements	60
3.6	Comparison of relaxation norms at 6τ for a Gaussian input using different approximations at the boundary (CN-Crank-Nicolson, FI-Fully Implicit)	68
3.7	Relaxation norms at 6τ for a Gaussian input using finite elements .	68
3.8	CPU times in minutes for the finite element (FE) and the finite difference (FD) methods	76
4.1	Projection errors during grid adaptation	92
4.2	Quadrature errors in Fokker-Planck coefficients, (C-Coefficient, S-Scheme, E-Exact, T-Trapezoidal, L-Lagrangian, H-Hermite)	92
4.3	Density and energy errors per time step and the renormalization constants a and b	94

4.4	Number of time steps required for the evolution of a Gaussian species starting with $\Delta\tau = 0.1$ for $t_{max} = 1.0$ s	94
5.1	CPU times for the quadrilateral finite elements with respect to the linear elements	110
5.2	Relaxation norms for a Gaussian input	117
5.3	Comparison of errors (percent) with different boundary approxima- tions in the alternating direction method for two species ($\Delta\tau = 1/16$)	119
5.4	Relaxation norms for a Gaussian distribution with different boundary approximations ($\Delta\tau = 1/16$)	119
6.1	Comparison of fusion reactivities in a D-T plasma as obtained by Killeen's and Improved reaction loss models	133
6.2	Comparison of energies of different species obtained by treating elec- trons as a general and a background species (Gen-General and Bgd- Background).	135
6.3	Increase in the fusion reactivity due to alpha heating in a D-T plasma	137
6.4	Effect of parameter β on $\langle \sigma v \rangle$ in time dependent calculations of D-T plasmas with particle and energy sinks	142
B.1	Gauss points and weights	168

Chapter 1

Introduction

1.1 Motivation and Objectives

Fusion Plasmas are generally not in a state of local thermodynamic equilibrium. In such cases the charged particle distribution functions are non-Maxwellian. For many applications, the actual knowledge of the distribution functions is required. Examples include, among others, the study of auxiliary heating by neutral beams or microwaves, thermalization of alpha particles in D-T plasmas, and the study of runaway electrons in tokamaks. In all these cases, kinetic models based on the Boltzmann equation with Fokker-Planck collision terms have been successful (Killeen, Kerbel, *et al.*, 1986). However, numerical simulations based on the kinetic equations involve considerable computational effort due to the nonlinear nature of the governing partial integrodifferential equations. Further, widely different characteristic velocities and relaxation times encountered in plasmas together with highly peaked distributions arising out of auxiliary heating and reaction products add to the complications in the numerical modeling process.

The finite difference method has been generally used for the numerical solution of Fokker-Planck equations, with relatively less emphasis on the finite element method. In the present work both finite element and finite difference methods of discretization have been employed, with emphasis on the following aspects of the simulation process:

- i. The governing Fokker-Planck equations and the Rosenbluth potentials are cast in a dimensionless form using a cut-off velocity characteristic to each species. This allows the nodes for each species to be chosen independently of other species.
- ii. In putting the equations for a particular species in the dimensionless form, the relaxation time of the species is used for normalizing the time variable. This facilitates each species to be integrated on its own characteristic time scale. This is possible in Fokker-Planck equations as the coupling between the different species is only through Rosenbluth potentials.
- iii. In spherical polar geometry, the Fokker-Planck operator has singularities at $v = 0$, and $\theta = 0$ and π . These are eliminated analytically in the present work, and the resulting operator is discretized at the actual boundaries rather than at near-by points.
- iv. Multispecies Fokker-Planck equations both in 1-D and 2-D are solved by Galerkin finite element method. The relative performance of various finite elements is studied. Sufficient emphasis is put on the study of density and energy conservation, velocity scale refinement and its effect on the numerical oscillations, and time step control based on the energy norm of the error in the computed solutions.
- v. Discretization errors over the velocity space are studied and a strategy to redistribute the nodes optimally to minimize the errors is presented. In view of the integrodifferential nature of the governing equations, the possibility of improving the accuracy using higher order interpolation and quadrature schemes is also studied.
- vi. A comparison of the Spitzer equipartition model with Fokker-Planck results, an improved fusion reaction loss term, and a few other aspects of energy transfer involving fast ions are also included.

A brief outline of the work is presented in Section 1.4. In the next two sections the relevant literature for the present work is reviewed.

1.2 Numerical solution of Fokker-Planck equations

The literature in the area of numerical solution of Fokker-Planck equations is reviewed here. A starting point could be the two books written 8 years ago (Killeen, Kerbel, *et al.*, 1986; Dnestrovskii and Kostomarov, 1986) which give a wealth of literature and the history of the developments in the numerical simulation of fusion plasmas. These books provide a detailed description of several state-of-art Fokker-Planck computational models based on the finite difference method, together with many useful applications of these models to magnetically confined plasmas.

The finite difference method of solution to Fokker-Planck equation is fairly established. Research has progressed step by step starting with single species calculations under simplifying assumptions to multidimensional models for multispecies. The Fokker-Planck equation was derived in spherical polar coordinates by Rosenbluth, MacDonald and Judd (1957) under the assumption that the distribution functions are azimuthally symmetric in (v, μ, φ) space ($\mu = \cos\theta$, where θ is the pitch angle). The potentials and the distribution functions are expanded in Legendre polynomials, which eventually lead to a system of coupled 1-D nonlinear integro-differential equations. Bing and Roberts (1961) solved the Fokker-Planck equation numerically for one ion species without taking into account the effect of electrons and other species. Their work also includes a feasibility study of using approximately separable solutions in (v, μ) space. A similar work was attempted by BenDaniel and Allis (1962), with emphasis on approximating the distribution functions in a separable form. Their study also involved modeling fusion applications for different parameters in mirror machines.

The Fokker-Planck calculations in 1-D were later extended to more than one species. A study of energy transfer from hot ions to cold electrons was made by solving Fokker-Planck equations for electrons keeping the ion distribution fixed in time (Killeen, Heckrotte and Boer, 1962). Steady state 1-D Fokker-Planck equations were solved both for ions and electrons by Fowler and Rankin (1966). The distribution functions are taken to be functions of energy. A time dependent Fokker-Planck code was later developed by Killeen and Futch (1968) to solve the 1-D kinetic equations

for ions and electrons in the velocity space v . The Fokker-Planck coefficients are extrapolated using the values at the previous time steps. The singularity at $v = 0$ is avoided by solving the equations for the interior points only in the numerical grid. This code was used to model certain applications in mirror machines.

Application oriented 1-D models were further developed by Killeen and Marx (1970). This work was also extended to 2-D in velocity space v and θ for one ion species. The ion equation was solved by alternating direction implicit method. The coefficients in the 2-D Fokker-Planck equation were obtained by calculating the potentials g and h in their elliptic integral form. They have also discussed alternative ways of computing the potentials. Whitney (1970) solved the 2-D Fokker-Planck equation by expanding the solution in Legendre polynomials, which results in a system of 1-D equations. The equations are exact to all orders of Legendre polynomials. Until now the Fokker-Planck collision operator was expanded (nonconservative form) and then solved numerically. A new finite difference scheme which addresses mainly to the problem of distribution functions becoming negative was presented by Chang and Cooper (1970). They showed that their recommended scheme, based on conservative form of the collision operator, improves the accuracy of the solution and also possibly reduces the computational time. All the models/codes developed later on are mostly based on the conservative form of the Fokker-Planck collision operator.

Full velocity space multispecies codes (Mirin, 1975; Killeen, Mirin and Rensink, 1976) were developed to model applications in fusion plasmas for mirrors and tokamaks. These codes include many source and loss terms. The concept of hybrid models was also introduced in which the electrons are treated as isotropic. The 2-D ion kinetic equations are solved either by the semi-implicit or by the alternating direction implicit method, whereas 1-D equation is solved for electrons. These codes were also used to study the effect of anisotropic part of the ion-ion Rosenbluth potentials on certain parameters of interest. Fowler, Smith and Rome (1978) developed a code (FIFPC) to study the slowing down process of fast ions in tokamaks. This model treats the background plasma species to be Maxwellian. The Fokker-Planck equation is solved by the Crank-Nicolson and the alternating direction implicit methods. A 2-D multispecies nonlinear Fokker-Planck package (FP-

PAC) was developed by McCoy, Mirin and Killeen (1981). In this code derivatives in the velocity space are approximated by central differences. The collision operator which has singularities at the boundaries is also approximated numerically. Time stepping is made by semi-implicit or the alternating direction implicit or fully implicit methods. FPPAC is considered to be a standard 2-D Fokker-Planck code for plasmas in uniform magnetic fields. Later, they incorporated an improved finite difference scheme, which is similar to that suggested by Chang and Cooper (1970). According to them, FPPAC88, the newer version of the old code FPPAC, virtually eliminates the problem of distribution functions becoming negative (Mirin, McCoy, *et al.*, 1988).

Andrade and Oliphant (1981) solved 2-D Fokker-Planck equation by using a five point algorithm. They have calculated the coefficients with isotropic background species for all times. Spatial part is also included in their model. The resulting algebraic system of equations was solved by matrix factorization. For the 1-D time dependent Fokker-Planck equations several discretization schemes have been suggested by Larsen, Levermore, *et al.* (1985). According to them, their schemes possess certain advantages over the scheme of Chang and Cooper (1970). However their approach requires the coefficients of the equations in analytic form which can not be easily satisfied even in the case of 1-D multispecies models.

Karney (1986) presented the numerical treatment of Fokker-Planck equation with particular reference to the study of rf driven current. He has discussed various time stepping schemes including the Chebyshev acceleration which is used to vary the time steps. Similar calculations for rf heating were made by O'Brien, Cox and Start (1986). It is suggested that unequally spaced mesh points in the finite difference or the finite element method may reduce the number of grid points required. They ignored the singularities present in the collision operator by choosing the lower cut-off slightly away from the singular points or the boundaries. Recently McKenzie, O'Brien and Cox (1991) developed a code BANDIT3D based on the finite difference method to solve the 3-D Fokker-Planck equation for electrons in a tokamak. This work includes a Fokker-Planck model in (v, θ) together with one spatial variable r . Ions are assumed to be Maxwellian. The equation is advanced in time using an operator splitting technique in two stages. The code can be used

to study both kinetic and transport physics.

The progress in the area of finite element modeling of fusion plasmas has been slow till now. Fyfe, Weiser, *et al.* (1981) applied Rayleigh-Ritz finite element method to solve a linearized steady state Fokker-Planck equation in variational form. They used B-splines as basis functions for the phase space variables (energy and μ), and solved the equation in a rectangular domain. A relativistic multiregion bounce averaged Fokker-Planck code for mirror plasmas was developed later (Matsuda and Stewart, 1986). This work includes solution of Fokker-Planck equation by Galerkin finite element method with specific applications to mirror plasmas. This code also uses one dimensional splines in energy and magnetic moment phase space. Poisson equations are solved directly by finite element method for the Rosenbluth potentials. Finite element method has also been used to model wave particle interactions for rf heating based on Fokker-Planck equations (Succi, Appert, *et al.*, 1986).

Attempts have also been made to use the standard finite element library solvers to model plasma applications, mostly to solve a single kinetic equation. Shoucri, Fuchs and Bers (1987), Shoucri, Shkarofsky, *et al.* (1989) used standard 2-D finite element based partial differential equation solvers to model rf heating. These models mostly involve a fixed number of Maxwellians and seek the steady state solutions of Fokker-Planck equations for electrons. Harrison (1988) has applied moving finite element method to solve 1-D kinetic equations. Recently Gardner, Gardner and Zaki (1993) have modeled a few applications in which 1-D Fokker-Planck equation is coupled with other equations. The equations are solved by the Galerkin finite element method using the linear finite elements.

Calculations of fusion reactivities $\langle \sigma v \rangle$ can be improved if the distribution functions of the interacting species are known more accurately. The enhancement in the fusion reactivities due to auxiliary heating was pointed out by Dawson, Furth and Tenney (1971). Since then fusion reactivity calculations have been performed under various conditions involving non-Maxwellian distributions (for example, Futch Jr., Holdren, *et al.*, 1972; Jassby and Towner, 1976; Slaughter, 1983). Over the years, convenient expressions and formulae have also been developed for Maxwellian (thermal) reactivities and fusion cross-sections (Hively, 1977; Bosch and Hale, 1992). Faster methods have been developed to compute $\langle \sigma v \rangle$, which is a

5-D integral in velocity space, using Legendre polynomials (Cordey, Marx, *et al.*, 1978). The 5-D integral can be simplified to 3-D integral if one of the distributions is isotropic (Marx, Mirin, *et al.*, 1976).

Various studies have been made to investigate the effect of distortion in the ion distribution functions on the fusion reactivities. The improvement in the fusion reactivity and multiplication factor in the presence of fast ions has been studied recently by Niikura and Nagami (1988), Niikura, Nagami and Horiike (1988), and Niikura and Nagami (1990). Fast ion distribution functions are used in analytical form, which are obtained by solving linearized Fokker-Planck equations. The dependence of $\langle \sigma v \rangle$ on the fast ion energy and ICRF heating is also addressed. Bittoni, Cordey and Cox (1980) have shown that the (kinetic) temperature of the tail is dependent critically upon the velocity dependence of the particle and energy loss mechanisms. Mirin and Tomaschke (1982) have compared the fusion reactivity in TFTR, obtained by solving the Fokker-Planck equations for bulk ions with that obtained under the assumption of Maxwellian distributions. The effect of the distortion of the bulk ion distribution from the Maxwellian during heating by energetic particles was found to be rather insignificant. The heating of plasma by energetic particles including loss models have also been studied by Sigmar and Joyce (1971), Tsuji, Katsurai, *et al.* (1976), and Jassby (1977). Steady state calculations were made under neutral beam heating scenarios in the presence of velocity dependent loss mechanisms (Matsuura, Nakao and Kudo, 1992; Matsuura, Nakao, *et al.*, 1993). It is pointed out that some of the calculations are strongly dependent on the plasma conditions and the loss mechanisms.

1.3 Adaptive Node Distribution

The topic of adaptive grid refinement is wide ranging. The status of the adaptive refinement techniques in finite difference, finite element, and other methods is reviewed in, for example, Hawken, Gottlieb and Hansen (1991) and Brebbia and Aliabadi (1993). The main steps in the process of grid refinement are:

- i. the choice of the variable(s) and the error norms based on which the refinement is made,
- ii. the computation of error estimates,
- iii. the strategies used to refine the grid.

These steps are common to both the finite difference and the finite element methods. The central idea is to improve the quality of numerical solution by distributing the nodes optimally. In this process, the errors are either reduced, or distributed more uniformly for the same number of grid points.

Grid refinement is still new in the area of numerical solution of Fokker-Planck equations. The moving finite element method has been applied to solve a single 1-D Fokker-Planck equation by Harrison (1988). He has shown that an adaptive grid, with less number of nodes, reduces the oscillations in the solution. In the grid refinement process, the error measures are sometimes chosen heuristically, depending upon the nature of the problem. For problems in which the variables experience steep gradients, the nodes may be placed in proportion to the gradients (for example, Russell and Christiansen, 1978; Dwyer, Kee and Sanders, 1980; Carey and Oden, 1984; Arney and Flaherty, 1986). In some other problems, variation in a key variable or a parameter relevant to the problem of interest is chosen as the error estimate (Yasar and Moses, 1992; Golias and Tsiboukis, 1993; Brebbia and Aliabadi, 1993). Altas and Stephenson (1991) have used an approach based on the errors in the integral values of the solution.

Local discretization or truncation errors at different grid points have been used for grid refinement in the finite difference method by Crowder and Dalton (1971) and de Rivas (1972). Denny and Landis (1972) solved a two point boundary value problem adaptively using the leading truncation error term as an error measure in a three point finite difference approach. Various strategies for adapting the meshes for boundary value problems have been presented in detail by Russell and Christiansen (1978). Chong (1978) solved a class of parabolic differential equations using a variable mesh finite difference method. The truncation error is distributed more or less uniformly. Nonlinear partial differential equations have also been solved by

adaptive finite difference method (Schonauer, Raith and Glotz, 1981). Truncation errors have been obtained in a curvilinear coordinate system by Lee and Tsuei (1992). Some more details in using the adaptive grid in the finite difference method can be found in Berger and Olinger (1984) and Arney and Flaherty (1986).

The error measures can also be estimated by using a lower and next higher order finite difference formulae (Schonauer, Raith and Glotz, 1981). They have used Newton's interpolation polynomial to obtain the coefficients (weights) of the difference formulae. Efforts have also been made to generate the finite difference weights in a nonuniform grid for derivatives up to any order of accuracy in one dimension (Fornberg, 1988, 1990). The error measures can also be obtained by using fine and coarse grids. Altas and Stephenson (1991) obtained the error measures by dividing the sub cells of the computational domain into smaller cells. In the finite element method, the difference between quadratic finite element solution and the linear element solution can be evaluated and used as an error measure (Hassan, Probert, *et al.*, 1993). Golias and Tsiboukis (1993) have suggested some more ways of estimating the errors.

Many algorithms have been developed to refine the numerical grids based on the error estimates. Chong (1978) presented an algorithm to generate initial nonuniform mesh and to refine the grid later by distributing the errors nearly uniformly. Coyle, Flaherty and Ludwig (1986) studied the stability of several mesh moving schemes that are based on equidistribution. They have studied the schemes that are designed to move a mesh so that a particular quantity is uniform over the domain. A simple technique has been presented by Sanz-Serna and Christie (1986) to adapt the grid. Daripa (1992) developed some grid generators to distribute a fixed number of grid points appropriately. Fraga and Morris (1992) also implemented a new method for spatial grid refinement.

1.4 Outline of the Thesis

The thesis consists of seven chapters. Chapter 2 presents the dimensionless multi-velocity scale kinetic equations. The Fokker-Planck collision operators without singularities at the boundaries are also given. Chapter 3 deals with the numerical

solution of one dimensional Fokker-Planck equations by the Galerkin finite element method and the finite difference method. The computational aspects covered are the use of higher order schemes for quadrature and interpolation, conservation of density and energy, and the refinement of velocity scales. Redistribution of a fixed number of nodes, based on local discretization errors is dealt in Chapter 4. A scheme based on the energy error in the computed solutions, to accelerate the time marching, is also discussed in this chapter. Solutions of 2-D Fokker-Planck equations by the finite element method using five types of quadrilateral elements are given in Chapter 5. This chapter also includes the Θ -method, and the alternating direction implicit method as applied in the finite difference method. Chapter 6 presents some applications involving an improved reaction loss model, and the other sources and sinks considered for the simulation of plasmas. Chapter 7 summarizes the results obtained in Chapters 2-6 and presents a few suggestions for extending the present work further.

Chapter 2

Governing Equations and Boundary Singularities

2.1 Introduction

In a plasma the interactions at the Coulomb collisional time level largely affect the energy transfer among the species in order to bring the plasma into kinetic or thermodynamic equilibrium. Therefore kinetic models based on the Fokker-Planck Coulomb collision operator are essential in representing the plasma behavior. The collision operators which model the Coulomb interactions among the charged species have interesting properties. They conserve density, total energy and momentum of the species. Further the operators vanish for Maxwellian distributions at a common temperature in a multi-component plasma. Fokker-Planck equations, when represented in phase space, are functions of seven independent variables. In general the equations are reduced to 2-D in velocity space under the assumption of spatial independence and azimuthal symmetry in velocity space (uniform magnetic field). This is usually done to make the problem tractable. In many applications the 2-D models represent the plasma behavior adequately. The equations can further be reduced to 1-D in velocity space to deal with isotropic situations.

When Fokker-Planck equations are applied to model a multi-component plasma, the equations are solved for all the general species whose distributions are arbitrary. That is a system of coupled nonlinear integro-differential equations is solved. The

contributions from different species are included in the Fokker-Planck coefficients through the Rosenbluth potentials and their derivatives. In case of 2-D problems the distribution functions, and consequently the Rosenbluth potentials, can be expanded in Legendre polynomials to obtain the potentials and their derivatives at a faster rate. However if some of the distributions are Maxwellian the Fokker-Planck coefficients get simplified.

In this chapter, the multi-velocity and time scale Fokker-Planck equations have been presented. In this approach dimensionless velocity and time scales most appropriate for each species are used. The structure of the Fokker-Planck equations in which the coupling between different species is only through the Rosenbluth potentials makes this approach possible. Analytical limits of the Coulomb collision operator at the boundaries are also presented.

2.2 Basic Equations

2.2.1 Preliminaries

In general the distribution functions for charged particles in a plasma are obtained by solving Boltzmann transport equation with Fokker-Planck collision terms, known as Fokker-Planck equations. These equations can be written as

$$\frac{\partial f_a}{\partial t} + \mathbf{v} \cdot \frac{\partial f_a}{\partial \mathbf{r}} + \frac{\mathbf{F}}{m_a} \cdot \frac{\partial f_a}{\partial \mathbf{v}} = \left(\frac{\partial f_a}{\partial t} \right)_c + S_a + L_a, \quad (2.1)$$

where $f_a(\mathbf{r}, \mathbf{v}, t)$ is the distribution function for species a at time t and at spatial location \mathbf{r} with velocity \mathbf{v} , \mathbf{F} is the force field, $(\partial f_a / \partial t)_c$ is the Fokker-Planck collision term representing the rate of change of f_a due to small angle Coulomb collisions, and S_a and L_a are the source and loss terms respectively.

Assuming that f_a is independent of spatial position and that force \mathbf{F} arises only from a magnetic field about which f_a possesses azimuthal symmetry, eq. (2.1) reduces to

$$\frac{\partial f_a}{\partial t} = \left(\frac{\partial f_a}{\partial t} \right)_c + S_a + L_a. \quad (2.2)$$

Under these assumptions the Fokker-Planck collision operator derived by Rosenbluth, MacDonald and Judd (1957) is of the form

$$\left(\frac{\partial f_a}{\partial t}\right)_c = \Gamma_a \left\{ -\frac{\partial}{\partial v_i} \left(f_a \frac{\partial h_a}{\partial v_i} \right) + \frac{1}{2} \frac{\partial^2}{\partial v_i \partial v_j} \left(f_a \frac{\partial^2 g_a}{\partial v_i \partial v_j} \right) \right\}, \quad (2.3)$$

where g_a and h_a are called Rosenbluth potentials. The potentials are given by (McCoy, Mirin and Killeen, 1981)

$$g_a = \sum_b \left(\frac{Z_b}{Z_a} \right)^2 \ln \Lambda_{ab} \int f_b(\mathbf{v}') |\mathbf{v} - \mathbf{v}'| d\mathbf{v}', \quad (2.4)$$

$$h_a = \sum_b \frac{m_a + m_b}{m_b} \left(\frac{Z_b}{Z_a} \right)^2 \ln \Lambda_{ab} \int f_b(\mathbf{v}') |\mathbf{v} - \mathbf{v}'|^{-1} d\mathbf{v}', \quad (2.5)$$

where the index b is over all the species including a and Λ_{ab} is the Coulomb logarithm which depends on both the interacting species a and b . Coulomb logarithm is taken from Futch Jr., Holdren, *et al.* (1972), which is given by

$$\ln \Lambda_{ab} = \ln \left\{ \left(\frac{m_a m_b}{m_a + m_b} \right) \frac{8\pi\epsilon_0 \alpha c \lambda_D}{e^2} \max \left[\left(\frac{2\bar{E}}{m} \right)_{a,b}^{1/2} \right] \right\} - \frac{1}{2}, \quad (2.6)$$

where $\alpha = 1/137$ is the fine structure constant, c is the velocity of light, \bar{E} is the mean energy of the species a or b and λ_D is the Debye length. Γ_a and λ_D are defined as

$$\Gamma_a = \left(\frac{Z^4 e^4}{4\pi\epsilon_0^2 m_a^2} \right); \quad \lambda_D = \left(\frac{2\epsilon_0 E_e}{3n_e e^2} \right)^{1/2}, \quad (2.7)$$

where Z_a , m_a are the charge number and mass of the species a , n_e and E_e are average electron density and energy respectively, and ϵ_0 is the permittivity of free space.

2.2.2 Basic Equations in 2-D Velocity Space

Rosenbluth, MacDonald and Judd (1957) further simplified eq. (2.3) by choosing spherical polar coordinates in velocity space (v, θ, φ) , where v is the speed, θ the pitch angle between velocity vector and magnetic field, and φ is the azimuthal angle. With the assumption that the distribution functions f are azimuthally symmetric i.e., independent of φ , eq. (2.3) becomes (McCoy, Mirin and Killeen, 1981)

$$\left(\frac{\partial f_a}{\partial t} \right)_c = \Gamma_a \left(\frac{1}{v^2} \frac{\partial G_a}{\partial v} + \frac{1}{v^2 \sin \theta} \frac{\partial H_a}{\partial \theta} \right), \quad (2.8)$$

where

$$G_a = A_a f_a + B_a \frac{\partial f_a}{\partial v} + C_a \frac{\partial f_a}{\partial \theta}, \quad (2.9)$$

$$H_a = D_a f_a + E_a \frac{\partial f_a}{\partial v} + F_a \frac{\partial f_a}{\partial \theta}. \quad (2.10)$$

The coefficients A_a through F_a are

$$\begin{aligned} A_a = & \frac{v^2}{2} \frac{\partial^3 g_a}{\partial v^3} + v \frac{\partial^2 g_a}{\partial v^2} - \frac{\partial g_a}{\partial v} - v^2 \frac{\partial h_a}{\partial v} - \frac{1}{v} \frac{\partial^2 g_a}{\partial \theta^2} \\ & + \frac{1}{2} \frac{\partial^3 g_a}{\partial v \partial \theta^2} - \frac{\cot \theta}{v} \frac{\partial g_a}{\partial \theta} + \frac{\cot \theta}{2} \frac{\partial^2 g_a}{\partial v \partial \theta}, \end{aligned} \quad (2.11)$$

$$B_a = \frac{v^2}{2} \frac{\partial^2 g_a}{\partial v^2}, \quad (2.12)$$

$$C_a = -\frac{1}{2v} \frac{\partial g_a}{\partial \theta} + \frac{1}{2} \frac{\partial^2 g_a}{\partial v \partial \theta}, \quad (2.13)$$

$$\begin{aligned} D_a = & \frac{\sin \theta}{2v^2} \frac{\partial^3 g_a}{\partial \theta^3} + \frac{\sin \theta}{2} \frac{\partial^3 g_a}{\partial v^2 \partial \theta} + \frac{\sin \theta}{v} \frac{\partial^2 g_a}{\partial v \partial \theta} \\ & - \frac{1}{2v^2 \sin \theta} \frac{\partial g_a}{\partial \theta} + \frac{\cos \theta}{2v^2} \frac{\partial^2 g_a}{\partial \theta^2} - \sin \theta \frac{\partial h_a}{\partial \theta}, \end{aligned} \quad (2.14)$$

$$E_a = \sin \theta \left[-\frac{1}{2v} \frac{\partial g_a}{\partial \theta} + \frac{1}{2} \frac{\partial^2 g_a}{\partial v \partial \theta} \right], \quad (2.15)$$

$$F_a = \frac{\sin \theta}{2v^2} \frac{\partial^2 g_a}{\partial \theta^2} + \frac{\sin \theta}{2v} \frac{\partial g_a}{\partial v}. \quad (2.16)$$

The density n_a and energy E_a of species a are defined as

$$n_a = 2\pi \int_0^\pi \int_0^\infty f_a(v, \theta) v^2 \sin \theta \, dv d\theta, \quad (2.17)$$

$$n_a E_a = m_a \pi \int_0^\pi \int_0^\infty f_a(v, \theta) v^4 \sin \theta \, dv d\theta. \quad (2.18)$$

In the above equation E_a denotes the average energy per particle. This should not be confused with the symbol E_a in eqs. (2.10) and (2.15) which denote one of the Fokker-Planck coefficients. The Fokker-Planck equations (2.2) are now of the form

$$\frac{\partial f_a}{\partial t} = \Gamma_a \left(\frac{1}{v^2} \frac{\partial G_a}{\partial v} + \frac{1}{v^2 \sin \theta} \frac{\partial H_a}{\partial \theta} \right) + S_a + L_a, \quad (2.19)$$

which is a system of equations to be solved for different species in a plasma.

2.2.3 Rosenbluth Potentials and Legendre Polynomials

The integrands of the potentials g_a and h_a in eqs. (2.4)-(2.5) get simplified under the assumption of azimuthal symmetry. The integrands are reduced and expressed in terms of complete Elliptic integrals (Rosenbluth, MacDonald and Judd, 1957). The potentials are then written in the form of double integrals. As such, in principle, these double integrals and their derivatives can be evaluated numerically in order to calculate the coefficients. When the potentials are expressed as

$$g_a = \sum_b \left(\frac{Z_b}{Z_a} \right)^2 \ln \Lambda_{ab} \bar{g}_b, \quad (2.20)$$

$$h_a = \sum_b \frac{m_a + m_b}{m_b} \left(\frac{Z_b}{Z_a} \right)^2 \ln \Lambda_{ab} \bar{h}_b, \quad (2.21)$$

\bar{g}_b and \bar{h}_b satisfy the Poisson equations (Rosenbluth, MacDonald and Judd, 1957; Mirin, 1975), namely

$$\nabla^4 \bar{g}_b = -8\pi f_b, \quad (2.22)$$

$$\nabla^2 \bar{h}_b = -4\pi f_b. \quad (2.23)$$

The Poisson equations may be solved directly to get \bar{g}_a and \bar{h}_a . The potentials and their derivatives can then be obtained from these numerically.

However faster methods are preferable as these potentials are used repeatedly in the calculation of Fokker-Planck coefficients. A method based on which some of the Fokker-Planck codes have been developed is to decompose the distribution functions and thereby the potentials in Legendre polynomials. This procedure has been adopted in the present work also. Writing f_b (Mirin, 1975) as

$$f_b(v, \theta, t) = \sum_{l=0}^{\infty} V_l^b(v, t) P_l(\cos \theta), \quad (2.24)$$

where

$$V_l^b(v, t) = \frac{2l+1}{2} \int_0^\pi f_b(v, \theta, t) P_l(\cos \theta) \sin \theta d\theta. \quad (2.25)$$

The potentials g_a and h_a are written as

$$g_a(v, \theta, t) = \sum_{l=0}^{\infty} \sum_b \left(\frac{Z_b}{Z_a} \right)^2 \ln \Lambda_{ab} B_l^b(v, t) P_l(\cos \theta), \quad (2.26)$$

$$h_a(v, \theta, t) = \sum_{l=0}^{\infty} \sum_b \frac{m_a + m_b}{m_b} \left(\frac{Z_b}{Z_a} \right)^2 \ln \Lambda_{ab} A_l^b(v, t) P_l(\cos \theta), \quad (2.27)$$

with

$$A_l^b(v, t) = \frac{4\pi}{2l+1} \left[\int_0^v \frac{(v')^{l+2}}{v'^{l+1}} V_l^b(v', t) dv' + \int_v^\infty \frac{v^l}{(v')^{l-1}} V_l^b(v', t) dv' \right], \quad (2.28)$$

$$B_l^b(v, t) = -\frac{4\pi}{4l^2 - 1} \left[\int_0^v \frac{(v')^{l+2}}{v'^{l-1}} \left(1 - \frac{l - \frac{1}{2}}{l + \frac{3}{2}} \frac{(v')^2}{v^2} \right) V_l^b(v', t) dv' \right]$$

$$+ \int_v^\infty \frac{v^l}{(v')^{l-3}} \left(1 + \frac{l - \frac{1}{2}}{l + \frac{3}{2}} \frac{v^2}{(v')^2} \right) V_l^b(v', t) dv' \Big]. \quad (2.29)$$

The derivatives of g_a and h_a with respect to v can be obtained analytically from these coefficients. The θ derivatives are nothing but the derivatives of $P_l(\cos \theta)$ which can be done easily analytically. Legendre polynomials of order up to 8 and their derivatives are given in Appendix A.

2.3 Fokker-Planck Equations in Nondimensional Form

In this section, the normalization constants for velocity, time, and the distribution functions are introduced. Making use of these characteristic velocities and time constants, the Fokker-Planck equations are recast into a nondimensional form. The potentials, and density and energy integrals are also written in terms of these dimensionless variables.

Velocity

In a plasma, whether the species are Maxwellian or not, ions and electrons have to be represented adequately in velocity space for accurate modeling. The cut-off for velocity v is chosen in terms of the thermal speed v_a^{th} for each species a . Thermal speed is defined as

$$v_a^{th} = \sqrt{\frac{T_a}{m_a}}, \quad (2.30)$$

where T_a is the temperature of the species. In general a minimum of 5 or 6 times the thermal speed v_a^{th} can provide a satisfactory limit for the representation of species in velocity space for many applications. In the present work the velocity normalization constant \bar{v}_a is generally chosen to be $6 v_a^{th}$, unless otherwise mentioned.

Time

Here only two time constants, viz. one for all the ion species and the other for electrons, are considered based on the following facts. In a typical plasma ions and electrons, both fast and slow, have different self relaxation times depending upon their energy. The fastest relaxation time is of electrons, t_e , compared to t_i of ions. Among ions, the difference in t_i due to their masses is not significant. Therefore, one time constant \bar{t}_i , which is common for all the ions can be effectively used without any loss of generality. The self relaxation time t_i for ions (Roth, 1986) is

$$t_i = 2.256 \times 10^{-4} \frac{\sqrt{A_i}}{Z^3} \frac{T_i^{3/2}}{n_i(10^{20})} \quad \text{s}, \quad (2.31)$$

where A_i is the ion mass in terms of proton masses, the ion density n_i is in units of 10^{20} m^{-3} , and the kinetic temperature T_i is in units of keV. The time normalization constant \bar{t}_i can be chosen as a suitably weighted average of relaxation times t_i for various species. Similarly for electrons the self relaxation time is given by

$$t_e = 5.264 \times 10^{-6} \frac{T_e^{3/2}}{n_e(10^{20})} \quad \text{s}. \quad (2.32)$$

Here T_e is the kinetic temperature of electrons in keV, and n_e is the electron density in units of 10^{20} m^{-3} . In this case \bar{t}_e is taken to be equal to t_e .

Normalizations

The dimensionless velocity variable x_a and time τ_a for each species are defined by the following relations:

$$v = \bar{v}_a x_a, \quad (2.33)$$

$$t = \bar{t}_j \tau_a, \quad j = i, e \quad (2.34)$$

where x_a and τ_a are the normalized velocity and time respectively. The maximum dimensionless velocity x_{max} can be any value, and need not be common for all the species in the plasma. It is however convenient to take $x_{max} = 1.0$ for all species,

and choose and change the cut-off velocities during the evolution accordingly. In the present work, x_{max} is taken as 1.0 for all calculations.

The normalized distribution functions $f_a(x_a, \theta, \tau_a)$ are defined as

$$f_a(x_a, \theta, \tau_a) = \frac{\bar{v}_a^3}{n_a} f_a(v, \theta, t), \quad (2.35)$$

where n_a is the density of species a . For simplicity, the same symbol f_a is used for the nondimensional distribution function. Now the normalized Maxwellian distribution, which is independent of θ , is of the form

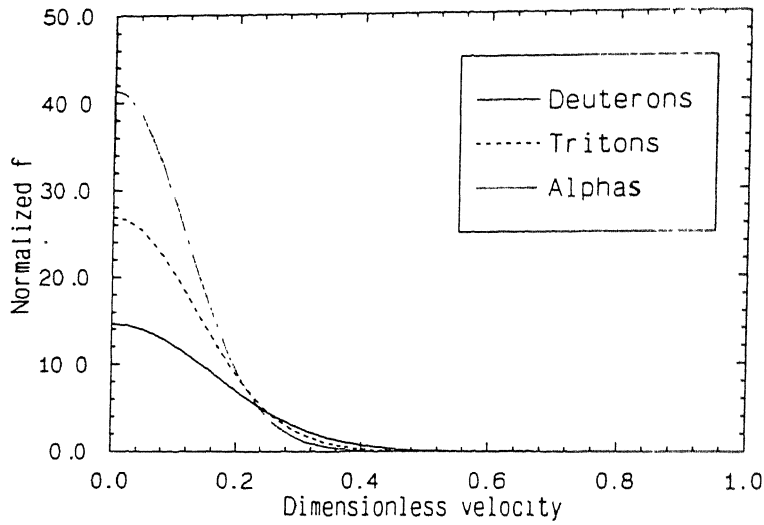
$$f_a(x_a) = \left(\frac{b}{\pi}\right)^{3/2} e^{-bx_a^2}, \quad (2.36)$$

where $b = m_a \bar{v}_a^2 / 2T_a$. The distribution functions for deuterons, tritons and alpha particles at a temperature of 20 keV are shown in Fig. 2.1a for a common velocity normalization constant $\bar{v} = 6.0 \times 10^6 \text{ m s}^{-1}$. If \bar{v} is increased further, the spectra of all the species become more and more peaked at the origin. This implies that the number of particles at the tail (at higher energies) will be negligibly small, which can be ignored. The presence of such low values of f at the tail end can become a source of oscillation in the numerical solutions. That is, the spectrum may become negative at the tail in a numerical solution.

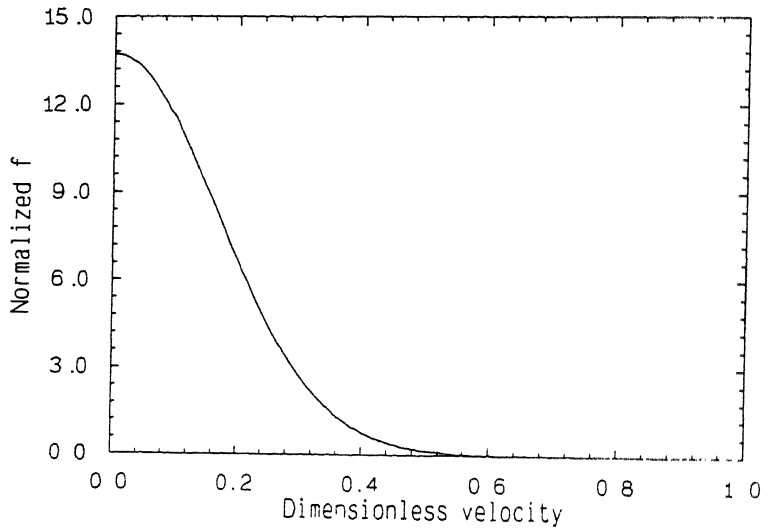
The undesirable portions in the tails can not be skipped if the same \bar{v} is used for all the species. However, if multi-velocity scales are used, each species including electrons can be represented individually, in which case the distribution functions of all the species, if Maxwellian, will be as depicted in Fig. 2.1b. It can be seen that the number of particles in the high energy region of different species are represented adequately and uniformly on their respective velocity scales.

2.3.1 Fokker-Planck Equations

The new variables incorporated into eqs. (2.8)-(2.16) lead to the following multi-velocity and time scale kinetic equations in dimensionless form. Same symbols have been used for the normalized quantities. This has been done for simplicity and to



a) Common velocity scale



b) Multi-velocity scale

Figure 2.1: Maxwellian distributions for different species

maintain continuity. Henceforth, unless otherwise specified, all the references will be made to these dimensionless variables only. The Fokker-Planck equations in nondimensional form are

$$\frac{\partial f_a}{\partial \tau_j} = K_a \left(\frac{1}{x_a^2} \frac{\partial G_a}{\partial x_a} + \frac{1}{x_a^2 \sin \theta} \frac{\partial H_a}{\partial \theta} \right) + S_a + L_a, \quad (2.37)$$

where

$$K_a = \left(\frac{n_a \Gamma_a \tilde{t}_j}{\bar{v}_a^3} \right), \quad j = i, e \quad (2.38)$$

and

$$G_a = A_a f_a + B_a \frac{\partial f_a}{\partial x_a} + C_a \frac{\partial f_a}{\partial \theta}, \quad (2.39)$$

$$H_a = D_a f_a + E_a \frac{\partial f_a}{\partial x_a} + F_a \frac{\partial f_a}{\partial \theta}. \quad (2.40)$$

S_a and L_a are the source and loss terms, respectively. The Fokker-Planck coefficients are

$$\begin{aligned} A_a = & \frac{x_a^2}{2} \frac{\partial^3 g_a}{\partial x_a^3} + x_a \frac{\partial^2 g_a}{\partial x_a^2} - \frac{\partial g_a}{\partial x_a} - x_a^2 \frac{\partial h_a}{\partial x_a} - \frac{1}{x_a} \frac{\partial^2 g_a}{\partial \theta^2} \\ & + \frac{1}{2} \frac{\partial^3 g_a}{\partial x_a \partial \theta^2} - \frac{\cot \theta}{x_a} \frac{\partial g_a}{\partial \theta} + \frac{\cot \theta}{2} \frac{\partial^2 g_a}{\partial x_a \partial \theta}, \end{aligned} \quad (2.41)$$

$$B_a = \frac{x_a^2}{2} \frac{\partial^2 g_a}{\partial x_a^2}, \quad (2.42)$$

$$C_a = -\frac{1}{2x_a} \frac{\partial g_a}{\partial \theta} + \frac{1}{2} \frac{\partial^2 g_a}{\partial x_a \partial \theta}, \quad (2.43)$$

$$\begin{aligned} D_a = & \frac{\sin \theta}{2x_a^2} \frac{\partial^3 g_a}{\partial \theta^3} + \frac{\sin \theta}{2} \frac{\partial^3 g_a}{\partial x_a^2 \partial \theta} + \frac{\sin \theta}{x_a} \frac{\partial^2 g_a}{\partial x_a \partial \theta} \\ & - \frac{1}{2x_a^2 \sin \theta} \frac{\partial g_a}{\partial \theta} + \frac{\cos \theta}{2x_a^2} \frac{\partial^2 g_a}{\partial \theta^2} - \sin \theta \frac{\partial h_a}{\partial \theta}, \end{aligned} \quad (2.44)$$

$$E_a = \sin \theta \left[-\frac{1}{2x_a} \frac{\partial g_a}{\partial \theta} + \frac{1}{2} \frac{\partial^2 g_a}{\partial x_a \partial \theta} \right], \quad (2.45)$$

$$F_a = \frac{\sin \theta}{2x_a^2} \frac{\partial^2 g_a}{\partial \theta^2} + \frac{\sin \theta}{2x_a} \frac{\partial g_a}{\partial x_a}. \quad (2.46)$$

The Rosenbluth potentials g_a and h_a , and their derivatives are now of the form

$$g_a(x_a, \theta, \tau) = \sum_{l=0}^{\infty} \sum_b \left(\frac{Z_b}{Z_a} \right)^2 \ln \Lambda_{ab} \left(\frac{n_b}{n_a} \right) \left(\frac{\bar{v}_a}{\bar{v}_b} \right)^{-1} B_l^b(x_a, \tau) P_l(\cos \theta), \quad (2.47)$$

$$\frac{\partial g_a}{\partial x_a} = \sum_{l=0}^{\infty} \sum_b \left(\frac{Z_b}{Z_a} \right)^2 \ln \Lambda_{ab} \left(\frac{n_b}{n_a} \right) \frac{\partial B_l^b}{\partial x_a} P_l(\cos \theta), \quad (2.48)$$

$$\frac{\partial^2 g_a}{\partial x_a^2} = \sum_{l=0}^{\infty} \sum_b \left(\frac{Z_b}{Z_a} \right)^2 \ln \Lambda_{ab} \left(\frac{n_b}{n_a} \right) \left(\frac{\bar{v}_a}{\bar{v}_b} \right) \frac{\partial^2 B_l^b}{\partial x_a^2} P_l(\cos \theta), \quad (2.49)$$

$$\frac{\partial^3 g_a}{\partial x_a^3} = \sum_{l=0}^{\infty} \sum_b \left(\frac{Z_b}{Z_a} \right)^2 \ln \Lambda_{ab} \left(\frac{n_b}{n_a} \right) \left(\frac{\bar{v}_a}{\bar{v}_b} \right)^2 \frac{\partial^3 B_l^b}{\partial x_a^3} P_l(\cos \theta), \quad (2.50)$$

$$h_a(x_a, \theta, \tau) = \sum_{l=0}^{\infty} \sum_b \frac{m_a + m_b}{m_b} \left(\frac{Z_b}{Z_a} \right)^2 \ln \Lambda_{ab} \left(\frac{n_b}{n_a} \right) \left(\frac{\bar{v}_a}{\bar{v}_b} \right) A_l^b(x_a, \tau) P_l(\cos \theta), \quad (2.51)$$

$$\begin{aligned} \frac{\partial h_a}{\partial x_a} &= \sum_{l=0}^{\infty} \sum_b \frac{m_a + m_b}{m_b} \left(\frac{Z_b}{Z_a} \right)^2 \ln \Lambda_{ab} \left(\frac{n_b}{n_a} \right) \left(\frac{\bar{v}_a}{\bar{v}_b} \right)^2 \\ &\quad \frac{\partial A_l^b}{\partial x_a} P_l(\cos \theta). \end{aligned} \quad (2.52)$$

The expressions of $A_l^b(x_a, \tau)$ and $B_l^b(x_a, \tau)$, can be written in terms of four functionals M_l , N_l , R_l , and E_l , as follows:

$$A_l^b(x_a, \tau) = \frac{4\pi}{2l+1} [u^{-l-1} N_l(V_l^b) + u^l M_l(V_l^b)], \quad (2.53)$$

$$B_l^b(x_a, \tau) = \frac{4\pi}{2l+1} \left\{ \frac{1}{(2l+3)} [u^{-l-1} E_l(V_l^b) + u^{l+2} M_l(V_l^b)] \right.$$

$$-\frac{1}{(2l-1)}[u^{1-l}N_l(V_l^b) + u^l R_l(V_l^b)]\}, \quad (2.54)$$

where

$$u = \frac{\bar{v}_a}{\bar{v}_b} x_a. \quad (2.55)$$

V_l^b 's are as given in eq. (2.25), and the functionals are defined as

$$M_l(w(x_a)) = \int_u^{u_{max}} w(y) y^{(1-l)} dy, \quad (2.56)$$

$$N_l(w(x_a)) = \int_0^u w(y) y^{(2+l)} dy, \quad (2.57)$$

$$R_l(w(x_a)) = \int_u^{u_{max}} w(y) y^{(3-l)} dy, \quad (2.58)$$

$$E_l(w(x_a)) = \int_0^u w(y) y^{(4+l)} dy, \quad (2.59)$$

with

$$u_{max} = \frac{\bar{v}_a}{\bar{v}_b} x_{max}. \quad (2.60)$$

It may be noted that maximum limit of u (u_{max}) can be taken as x_{max} itself. Since x_{max} has been chosen as 1.0 in the present work, u_{max} also can be taken as 1.0.

As mentioned earlier, the derivatives of A_l^b and B_l^b in terms of the new variables can be obtained analytically. They are

$$\frac{\partial A_l^b}{\partial x_a} = \frac{4\pi}{2l+1} [l u^{l-1} M_l(V_l^b) - (l+1) u^{-l-2} N_l(V_l^b)], \quad (2.61)$$

$$\begin{aligned} \frac{\partial^2 A_l^b}{\partial x_a^2} &= \frac{4\pi}{2l+1} [(l+1)(l+2) u^{-l-3} N_l(V_l^b) + l(l-1) u^{l-2} M_l(V_l^b)] \\ &\quad - 4\pi V_l^b(u), \end{aligned} \quad (2.62)$$

$$\frac{\partial B_l^b}{\partial x_a} = \frac{4\pi}{2l+1} \left\{ \frac{1}{(2l+3)} [(l+2) u^{l+1} M_l(V_l^b) - (l+1) u^{-l-2} E_l(V_l^b)] \right.$$

$$-\frac{1}{(2l-1)}[lu^{l-1}R_l(V_l^b) - (l-1)u^{-l}N_l(V_l^b)]\Big\}, \quad (2.63)$$

$$\begin{aligned} \frac{\partial^2 B_l^b}{\partial x_a^2} = & \frac{4\pi}{2l+1} \left\{ \frac{(l+1)(l+2)}{(2l+3)}[u^{-l-3}E_l(V_l^b) + v^l M_l(V_l^b)] \right. \\ & \left. - \frac{l(l-1)}{(2l-1)}[u^{-l-1}N_l(V_l^b) + u^{l-2}R_l(V_l^b)] \right\}, \end{aligned} \quad (2.64)$$

$$\begin{aligned} \frac{\partial^3 B_l^b}{\partial x_a^3} = & \frac{4\pi}{2l+1} \left\{ \frac{(l+1)(l+2)}{(2l+3)}[lu^{l-1}M_l(V_l^b) - (l+3)u^{-l-4}E_l(V_l^b)] \right. \\ & \left. - \frac{l(l-1)}{(2l-1)}[(l-2)u^{l-3}R_l(V_l^b) - (l+1)u^{-l-2}N_l(V_l^b)] \right\}, \end{aligned} \quad (2.65)$$

$$\begin{aligned} \frac{\partial^4 B_l^b}{\partial x_a^4} = & \frac{4\pi}{2l+1} \left\{ \frac{1}{(2l+3)}[(l-1)l(l+1)(l+2)u^{l-2}M_l(V_l^b) \right. \\ & + (l+1)(l+2)(l+3)(l+4)u^{-l-5}E_l(V_l^b)] \\ & - \frac{1}{(2l-1)}[l(l-1)(l-2)(l-3)u^{l-4}R_l(V_l^b) \\ & + (l-1)l(l+1)(l+2)u^{-l-3}N_l(V_l^b)] \Big\} \\ & - 8\pi V_l^b(u). \end{aligned} \quad (2.66)$$

With the normalized distribution functions, the density and energy integrals in eqs. (2.17) and (2.18) become

$$2\pi \int_0^\pi \int_0^1 f_a(x_a, \theta) x_a^2 \sin \theta dx_a d\theta = 1, \quad (2.67)$$

$$m_a \bar{v}_a^2 \pi \int_0^\pi \int_0^1 f_a(x_a, \theta) x_a^4 \sin \theta dx_a d\theta = E_a, \quad (2.68)$$

where E_a is the energy per particle.

Boundary Conditions

The Fokker-Planck equations (2.37)-(2.46) are solved with the following velocity space boundary conditions (Killeen, Kerbel, *et al.*, 1986).

$$f_a(x_a = 0, \theta) \text{ is independent of } \theta, \quad (2.69)$$

$$\frac{\partial f_a}{\partial x_a}(x_a = 0, \theta = \pi/2) = 0, \quad (2.70)$$

$$\frac{\partial f_a}{\partial \theta}(x_a, \theta = 0) = \frac{\partial f_a}{\partial \theta}(x_a, \theta = \pi) = 0, \quad (2.71)$$

$$f_a(x_a = x_{max}, \theta) = 0. \quad (2.72)$$

Initial Conditions

Initial distribution of each species $f_a(x_a, \theta)$ at time $\tau_a = 0$ is specified. f_a can be any distribution including non-Maxwellian. This would facilitate a study of relaxation of arbitrary distributions to approximate steady state Maxwellian in the absence of source and loss terms. In fact this can serve as a test case for the code(s). In general, the initial distributions are used in a form given by (Futch Jr., Holdren, *et al.*, 1972; McCoy, Mirin and Killeen, 1981)

$$f_a(x_a, \theta) = \alpha_a \exp(-b_a(x_a - \beta_a)^2 - c_a(\theta - d_a)^2), \quad (2.73)$$

where β_a is defined as $a_a = \frac{1}{2}m_a\beta_a^2/\bar{v}_a^2$ and a_a, b_a, c_a , and d_a are constants which are given as input. α_a is obtained by satisfying eq. (2.67). The initial distribution functions of the form given here are referred to as Gaussian distribution functions. When $c_a = 0$, i.e. f_a is isotropic, the above distributions are sometimes called as shifted or displaced Maxwellians. Further when the distributions are Maxwellian, some of the Fokker-Planck coefficients also get simplified.

2.3.2 Background Species

Simulations of plasmas include both energetic and warm/cold background populations. Energy from fast ions is transferred to heat the background species. The background species are in general assumed to be isotropic, that is there is no θ dependence, and also Maxwellian. The distributions are of the form

$$f(x) = \left(\frac{b}{\pi}\right)^{3/2} e^{-bx^2} \quad (2.74)$$

where $b = m\bar{v}^2/2T$ and \bar{v} is the velocity normalization constant. In this case the potentials g_a and h_a get reduced to simpler forms and the contribution from such distributions to the respective coefficients are

$$A_a^b = 2 \frac{m_a}{m_b} \left(\frac{Z_b}{Z_a}\right)^2 \ln \Lambda_{ab} \frac{n_b}{n_a} \left[-\sqrt{\frac{b}{\pi}} u e^{-bu^2} + \frac{1}{2} \phi(\sqrt{b}u) \right], \quad (2.75)$$

$$B_a^b = \frac{m_b}{m_a} \frac{\bar{v}_b}{\bar{v}_a} \frac{1}{2bu} A_a^b, \quad (2.76)$$

$$F_a^b = \left(\frac{Z_b}{Z_a}\right)^2 \ln \Lambda_{ab} \frac{n_b}{n_a} \frac{\sin \theta}{2x_a} \left[\left(1 - \frac{1}{2bx_a^2}\right) \phi(\sqrt{b}u) + \frac{1}{\sqrt{\pi b} x_a} e^{-bx_a^2} \right], \quad (2.77)$$

where u is as defined in eq. (2.55), with $\bar{v}_b = \bar{v}$. In eqs. (2.75)-(2.77), the subscript or superscript b refers to the background species under consideration. In the above expressions terms containing $e^{-bu_{max}^2}$ have been ignored because they are negligible if suitable cut-off velocities are chosen. The function $\phi(z)$ is the error function defined as

$$\phi(z) = \frac{2}{\sqrt{\pi}} \int_0^z e^{-y^2} dy, \quad (2.78)$$

which can be evaluated easily by power series approximation. For $z < 0.6$,

$$\phi(z) = \frac{2}{\sqrt{\pi}} \sum_{k=0}^6 (-1)^k \frac{z^{2k+1}}{k!(2k+1)}, \quad (2.79)$$

and for $z \geq 0.6$,

$$\phi(z) = 1 - \frac{2}{\sqrt{\pi}} e^{-z^2} \sum_{k=1}^5 A_k \eta^k, \quad (2.80)$$

with

$$\eta = \frac{1}{1 + pz}, \quad (2.81)$$

and $p = 0.3275911$, $A_1 = 0.225836846$, $A_2 = -0.252128668$, $A_3 = 1.25969513$, $A_4 = -1.287822453$, and $A_5 = 0.94664607$.

2.4 Fokker-Planck Equations in One Dimension

One dimensional Fokker-Planck equations are easily obtained by setting $l = 0$ in eqs. (2.37)-(2.46) and neglecting terms containing θ derivatives. This results in the following equations:

$$\frac{\partial f_a}{\partial \tau_a} = K_a \frac{1}{x_a^2} \frac{\partial G_a}{\partial x_a}, \quad (2.82)$$

$$\frac{\partial f_a}{\partial \tau_a} = K_a \frac{1}{x_a^2} \frac{\partial}{\partial x_a} \left[A_a + B_a \frac{\partial f_a}{\partial x_a} \right]. \quad (2.83)$$

The boundary conditions are

$$\frac{\partial f_a}{\partial x_a} = 0 \text{ at } x_a = 0, \quad (2.84)$$

$$f_a = 0 \text{ at } x_a = x_{max} = 1.0. \quad (2.85)$$

The coefficients and the potentials are

$$A_a = \frac{x_a^2}{2} \frac{\partial^3 g_a}{\partial x_a^3} + x_a \frac{\partial^2 g_a}{\partial x_a^2} - \frac{\partial g_a}{\partial x_a} - x_a^2 \frac{\partial h_a}{\partial x_a}, \quad (2.86)$$

$$B_a = \frac{x_a^2}{2} \frac{\partial^2 g_a}{\partial x_a^2}, \quad (2.87)$$

and

$$g_a(x_a, \tau) = \sum_b \left(\frac{Z_b}{Z_a} \right)^2 \ln \Lambda_{ab} \left(\frac{n_b}{n_a} \right) \left(\frac{\bar{v}_a}{\bar{v}_b} \right)^{-1} B_0^b(x_a, \tau), \quad (2.88)$$

$$h_a(x_a, \tau) = \sum_b \frac{m_a + m_b}{m_b} \left(\frac{Z_b}{Z_a} \right)^2 \ln \Lambda_{ab} \left(\frac{n_b}{n_a} \right) \left(\frac{\bar{v}_a}{\bar{v}_b} \right) A_0^b(x_a, \tau). \quad (2.89)$$

The expressions for A_0^b and B_0^b are given by

$$A_0^b(x_a, \tau) = 4\pi \left[\frac{1}{u} N_0(f^b) + M_0(f^b) \right], \quad (2.90)$$

$$B_0^b(x_a, \tau) = 4\pi \left[\frac{1}{3} \left(\frac{1}{u} E_0(f^b) + u^2 M_0(f^b) \right) + (u N_0(f^b) + R_0(f^b)) \right]. \quad (2.91)$$

The derivatives of A_0^b and B_0^b are

$$\frac{\partial A_0^b}{\partial x_a} = 4\pi \left[-\frac{1}{u^2} N_0(f^b) \right], \quad (2.92)$$

$$\frac{\partial^2 A_0^b}{\partial x_a^2} = 4\pi \left[\frac{2}{u^3} N_0(f^b) \right] - 4\pi f_b(u), \quad (2.93)$$

$$\frac{\partial B_0^b}{\partial x_a} = 4\pi \left[\frac{1}{3} \left(2u M_0(f^b) - \frac{1}{u^2} E_0(f^b) \right) + N_0(f^b) \right], \quad (2.94)$$

$$\frac{\partial^2 B_0^b}{\partial x_a^2} = 4\pi \left[\frac{2}{3} \left(\frac{1}{u^3} E_0(f^b) + M_0(f^b) \right) \right], \quad (2.95)$$

$$\frac{\partial^3 B_0^b}{\partial x_a^3} = 4\pi \left[-\frac{2}{u^4} E_0(f^b) \right], \quad (2.96)$$

$$\frac{\partial^4 B_0^b}{\partial x_a^4} = 4\pi \left[\frac{8}{u^5} E_0(f^b) \right] - 8\pi f_b(u). \quad (2.97)$$

The functionals M_0 , N_0 , and E_0 are defined in eqs. (2.56)-(2.59). The coefficients can further be reduced to

$$A_a = 4\pi \sum_b \left(\frac{Z_b}{Z_a}\right)^2 \ln \Lambda_{ab} \left(\frac{n_b}{n_a}\right) \frac{m_a}{m_b} N_0(f^b), \quad (2.98)$$

$$B_a = 4\pi \sum_b \left(\frac{Z_b}{Z_a}\right)^2 \ln \Lambda_{ab} \left(\frac{n_b}{n_a}\right) \left(\frac{\bar{v}_a}{\bar{v}_b}\right)^{-1} \left[\frac{1}{3u} E_0(f^b) + \frac{u^2}{3} M_0(f^b) \right], \quad (2.99)$$

The density and energy integrals in 1-D are given as

$$4\pi \int_0^1 f_a(x_a) x_a^2 dx_a = 1, \quad (2.100)$$

$$m_a \bar{v}_a^2 2\pi \int_0^1 f_a(x_a) x_a^4 dx_a = E_a, \quad (2.101)$$

where E_a is the energy per particle, as earlier. As in 2-D, if the distribution is assumed to be Maxwellian for a background species, the corresponding contributions to the coefficients can be simplified. The final form of the coefficients are the same as given in eqs. (2.75)-(2.76).

2.5 Collision Operators without Boundary Singularities

The Fokker-Planck equations both in 1-D and 2-D can be solved numerically by the finite difference and the finite element methods. In the case of the finite difference method, the singularities in the collision operators at the boundaries have to be dealt with properly. The usual method employed is to approximate the operator at a point close to the boundary. In some cases, especially when the number of grid points in the computational domain is large, the boundary point can as well be ignored and the solution at the boundary is set to the value at the nearest node. In this section the analytical limits of the collision operator at the boundaries are presented, which are used in later chapters for discretization at the boundaries.

2.5.1 1-D Operator

The 1-D Fokker-Planck equations (2.82)-(2.83), dropping the subscript a and omitting the constant K_a for simplicity, can be written as

$$\frac{\partial f}{\partial \tau} = \frac{1}{x^2} \frac{\partial G}{\partial x}, \quad (2.102)$$

$$\frac{\partial f}{\partial \tau} = \frac{1}{x^2} \frac{\partial}{\partial x} \left[A f + B \frac{\partial f}{\partial x} \right]. \quad (2.103)$$

Here G is zero at $x = 0$ because $A = B = 0$ at $x = 0$. It can be seen easily that $\partial G / \partial x$ and $\partial^2 G / \partial x^2$ are also zero at $x = 0$, as must be the case if the limit of the right hand side is to exist. Therefore the limiting value can be found by applying L'Hôpital's rule (Apostol, 1962). Before doing this it is convenient to rewrite the right hand side of the above equation in expanded form as

$$\frac{\partial f}{\partial \tau} = A^* f + B^* \frac{\partial f}{\partial x} + C^* \frac{\partial^2 f}{\partial x^2}, \quad (2.104)$$

where the coefficients A^* , B^* , and C^* , obtained from eqs. (2.86)-(2.87) are given below:

$$A^* = \frac{1}{2} \frac{\partial^4 g}{\partial x^4} + \frac{2}{x} \frac{\partial^3 g}{\partial x^3} - \frac{2}{x} \frac{\partial h}{\partial x} - \frac{\partial^2 h}{\partial x^2}, \quad (2.105)$$

$$B^* = \frac{\partial^3 g}{\partial x^3} + \frac{2}{x} \frac{\partial^3 g}{\partial x^3} - \frac{1}{x^2} \frac{\partial g}{\partial x} - \frac{\partial h}{\partial x}, \quad (2.106)$$

$$C^* = \frac{1}{2} \frac{\partial^2 g}{\partial x^2}. \quad (2.107)$$

It should be noted that at $x = 0$,

$$g = \frac{\partial g}{\partial x} = \frac{\partial^3 g}{\partial x^3} = h = \frac{\partial h}{\partial x} = 0. \quad (2.108)$$

Therefore, second and third terms in A^* are of the form $0/0$. Their values are:

$$\lim_{x \rightarrow 0} \frac{1}{x} \frac{\partial^3 g}{\partial x^3} = \frac{\partial^4 g}{\partial x^4}, \quad (2.109)$$

$$\lim_{x \rightarrow 0} \frac{1}{x} \frac{\partial h}{\partial x} = \frac{\partial^2 h}{\partial x^2}. \quad (2.110)$$

Thus, the coefficient A^* at $x = 0$ is given by

$$A^* = \frac{5}{2} \frac{\partial^4 g}{\partial x^4} - 3 \frac{\partial^2 h}{\partial x^2}. \quad (2.111)$$

It is easily seen that $B^* \rightarrow \infty$, as $x \rightarrow 0$. This is due to the third term in eq. (2.106). Thus the limit of the second term in eq. (2.104) must be obtained together with the boundary conditions (2.84). Its limit is given by

$$\lim_{x \rightarrow 0} B^* \frac{\partial f}{\partial x} = \frac{\partial^2 g}{\partial x^2} \frac{\partial^2 f}{\partial x^2}. \quad (2.112)$$

This term is then combined with the third term in eq. (2.104) which is finite and nonzero at $x = 0$. The resulting operator at $x = 0$ can be written as

$$\frac{\partial f}{\partial \tau} = A^* f + C^* \frac{\partial^2 f}{\partial x^2} \quad (2.113)$$

where

$$C^* = \frac{3}{2} \frac{\partial^2 g}{\partial x^2}. \quad (2.114)$$

and A^* is as obtained in eq. (2.111).

2.5.2 2-D Operator

In this case the operators have singularities at three boundaries, $x = 0$, $\theta = 0$, and $\theta = \pi$. The singularities at $\theta = 0$ and π are of first order, due to the division by $\sin \theta$ term, while the singularity at $x = 0$ is of second order (see eqs. (2.37)-(2.46)). As the coefficients A_a through F_a are evaluated using potentials g_a and h_a which involve Legendre polynomials $P_l(\cos \theta)$, the analytical limits must be valid for all the orders, l , of Legendre polynomials.

The general steps are similar to the case for 1-D Fokker-Planck operator, but considerably more involved due to large number of terms and the need to evaluate

the limits for all values of l . Analysis of singularities is somewhat facilitated by rewriting eq. (2.37) in the following manner:

$$\frac{\partial f}{\partial \tau} = \frac{1}{x^2} \frac{\partial G}{\partial x} + \frac{1}{x^2 \sin \theta} \frac{\partial(\sin \theta H^*)}{\partial \theta}, \quad (2.115)$$

where

$$G = Af + B \frac{\partial f}{\partial x} + C \frac{\partial f}{\partial \theta}, \quad (2.116)$$

$$H^* = D^* f + E^* \frac{\partial f}{\partial x} + F^* \frac{\partial f}{\partial \theta}. \quad (2.117)$$

The coefficients D^* , E^* , and F^* are given by

$$\begin{aligned} D^* = & \frac{1}{2x^2} \frac{\partial^3 g}{\partial \theta^3} + \frac{1}{2} \frac{\partial^3 g}{\partial x^2 \partial \theta} + \frac{1}{x} \frac{\partial^2 g}{\partial x \partial \theta} - \frac{1}{2x^2 \sin^2 \theta} \frac{\partial g}{\partial \theta} \\ & + \frac{\cot \theta}{2x^2} \frac{\partial^2 g}{\partial \theta^2} - \frac{\partial h}{\partial \theta}, \end{aligned} \quad (2.118)$$

$$E^* = -\frac{1}{2x} \frac{\partial g}{\partial \theta} + \frac{1}{2} \frac{\partial^2 g}{\partial x \partial \theta}, \quad (2.119)$$

$$F^* = \frac{1}{2x^2} \frac{\partial^2 g}{\partial \theta^2} + \frac{1}{2x} \frac{\partial g}{\partial x}. \quad (2.120)$$

In the above equations, the constant K_a and the subscript a have been omitted for simplicity as earlier in this section. The following points have been made use of in the process of obtaining analytical expressions for the 2-D operator at the boundaries:

- a. At $x = 0$, coefficients $A-C$, $D^* - F^*$ are zero.
- b. At $x = 0$, g and h and their derivatives with respect to x are zero for $l > 4$.
- c. At $x = 0$, the terms containing θ derivatives are zero.
- d. At $\theta = 0$ and π , $A \neq 0$, $B \neq 0$, and $C = D^* = E^* = 0$.

e. All the odd derivatives of $P_l(\cos \theta)$ are zero at $\theta = 0$ and π .

f. The boundary conditions $\partial f / \partial \theta = 0$ at $\theta = 0$ and π are used where necessary.

At $\theta = 0$ and π

Considering the above points, the term containing $\partial f / \partial \theta$ in G drops out at $\theta = 0$ and π , while the other two terms remain, with the limiting expressions for A and B as follows:

$$A = \frac{x^2}{2} \frac{\partial^3 g}{\partial x^3} + x \frac{\partial^2 g}{\partial x^2} - \frac{\partial g}{\partial x} - x^2 \frac{\partial^2 h}{\partial x^2} - \frac{2}{x} \frac{\partial^2 g}{\partial \theta^2} + \frac{\partial^3 g}{\partial x \partial \theta^2}, \quad (2.121)$$

$$B = \frac{x^2}{2} \frac{\partial^2 g}{\partial x^2}. \quad (2.122)$$

The limit of the second term in eq. (2.115) is same at $\theta = 0$ and π , and is given by

$$\frac{2}{x^2} \frac{\partial H^*}{\partial \theta} = \frac{2}{x^2} \left(\frac{\partial D^*}{\partial \theta} f + \frac{\partial E^*}{\partial \theta} \frac{\partial f}{\partial x} + F^* \frac{\partial^2 f}{\partial \theta^2} \right), \quad (2.123)$$

where the terms which are zero have been dropped. The expression F^* remains the same as in eq. (2.120). The limiting expressions for the remaining two coefficients are as given below:

$$\frac{\partial D^*}{\partial \theta} = \frac{2}{3x^2} \frac{\partial^4 g}{\partial \theta^4} - \frac{1}{3x^2} \frac{\partial^2 g}{\partial x^2} + \frac{1}{x} \frac{\partial^3 g}{\partial x \partial \theta^2} + \frac{1}{2} \frac{\partial^4 g}{\partial x^2 \partial \theta^2} - \frac{\partial^2 h}{\partial \theta^2}, \quad (2.124)$$

$$\frac{\partial E^*}{\partial \theta} = -\frac{1}{2x} \frac{\partial^2 g}{\partial \theta^2} + \frac{1}{2} \frac{\partial^3 g}{\partial x \partial \theta^2}. \quad (2.125)$$

At $x = 0$

Equation (2.37) is expanded and written in the following form to facilitate the analysis of the singularity at $x = 0$:

$$\frac{\partial f}{\partial \tau} = \left[\bar{A} f + \bar{B} \frac{\partial f}{\partial x} + \bar{C} \frac{\partial^2 f}{\partial x^2} + \bar{D} \frac{\partial f}{\partial x \partial \theta} + \bar{E} \frac{\partial f}{\partial \theta} + \bar{F} \frac{\partial^2 f}{\partial \theta^2} \right], \quad (2.126)$$

where

$$\bar{A} = \frac{1}{x^2} \left[\frac{\partial A}{\partial x} + \frac{1}{\sin \theta} \frac{\partial D}{\partial \theta} \right], \quad (2.127)$$

$$\bar{B} = \frac{1}{x^2} \left[A + \frac{\partial B}{\partial x} + \frac{1}{\sin \theta} \frac{\partial E}{\partial \theta} \right], \quad (2.128)$$

$$\bar{C} = \frac{1}{x^2} B, \quad (2.129)$$

$$\bar{D} = \frac{1}{x^2} \left[C + \frac{1}{\sin \theta} E \right], \quad (2.130)$$

$$\bar{E} = \frac{1}{x^2} \left[\frac{\partial C}{\partial x} + \frac{1}{\sin \theta} D + \frac{1}{\sin \theta} \frac{\partial F}{\partial \theta} \right], \quad (2.131)$$

$$\bar{F} = \frac{1}{x^2} \left[\frac{1}{\sin \theta} F \right]. \quad (2.132)$$

Making use of the observations made earlier, it can be easily seen that the terms containing \bar{D} , \bar{E} , and \bar{F} drop out at $x = 0$, because their limits are zero. As in 1-D, $\bar{B} \rightarrow \infty$, as $x \rightarrow 0$. However, if $\partial f / \partial x$ is taken as zero at $x = 0$ for all values of θ , the limit of the term containing \bar{B} exists, and can be merged with the term containing \bar{C} , which is finite at $x = 0$. The resulting Fokker-Planck operator at $x = 0$ is:

$$\frac{\partial f}{\partial \tau} = A^* f + C^* \frac{\partial^2 f}{\partial x^2}, \quad (2.133)$$

where A^* and C^* are the same as in 1-D, eqs. (2.111) and (2.114). It is seen that the limiting expressions of the operator in 2-D is same as in 1-D. It must be mentioned here that for the limit to exist at $x = 0$ in 2-D, the boundary condition $(\partial f / \partial x)_{x=0} = 0$ has to be imposed for all values of θ , instead of at $\theta = \pi/2$ only as in eq. (2.70). This fact gets masked if the operator is approximated at near-by nodes, as is usually done. The expressions given in this section, besides being free from singularities, are also simpler, and lead to elegant and accurate discretization of the collision operator at the boundaries.

2.6 Summary

The work that has been carried out in this chapter can be summarized as under:

- i. 2-D velocity space kinetic equations applicable to plasmas in their general form have been presented.
- ii. The concept of using multi-velocity and time scales in the kinetic simulation of plasmas has been presented. The dimensionless Fokker-Planck equations and Rosenbluth potentials in 2-D velocity space are given. These equations can be used for an arbitrary number of general and background species. In the case of background species, separate expressions for the coefficients have been arrived at using the characteristic velocity scales.
- iii. One dimensional multi-velocity scale Fokker-Planck equations, as derived from 2-D equations, are also presented.
- iv. Both 1-D and 2-D collision operators have singularities at the boundaries. The singularities are removed analytically and the non-singular operators to be applied at the boundaries are given.

Chapter 3

One Dimensional Fokker-Planck Equations

3.1 Introduction

In a numerical solution of the Fokker-Planck equations, accuracy of the computed solution with regard to the distribution functions as well as satisfying the conservation requirements are equally important. Difficulties arise as the numerical solutions are expected to conserve both the density and energy. Suitable choice of boundary conditions can sometimes be applied to satisfy either the density or the energy condition accurately. In this context the finite element method can possibly play a better role because it is known, despite the fact that more computational effort is involved, that the spatial resolution in the finite element solutions is better than the finite difference solutions. In addition, the finite element method offers certain advantages for problems with curved boundaries. The operator singularities encountered in curvilinear coordinate systems at the boundaries are also easier to deal with in the finite element method.

In this chapter one dimensional Fokker-Planck equations have been solved by both the Galerkin finite element method and the finite difference method. Various aspects of the computation process are illustrated for a multispecies plasma including electrons as a general species. The Fokker-Planck solutions have also been compared with the Spitzer energy relaxation model which is valid under the

Maxwellian conditions.

3.2 Finite Element Method

In this method, the computational domain of interest is divided into a number of non-overlapping subdomains or finite elements. The solution to the governing equation is then constructed by using piece wise polynomials over each element, called the shape functions. This approximate solution in satisfying the governing equations results in a residue R which can be minimized with respect to weighting functions W_i as

$$\int_{\Omega} W_i R d\Omega = 0, \quad i = 1, \dots, N, \quad (3.1)$$

where N is the number of nodes in the domain. In the finite element discretization procedure, the elemental contributions are assembled to obtain the global system of equations at all the nodes. The global equations are solved to get the approximate solution to the governing equation. Nevertheless there are many ways to choose the weighting functions W_i . In Galerkin finite element approach, the W_i are chosen to be identical to the shape functions themselves.

The various steps associated with Galerkin finite element method of solution are given in detail with the help of 1-D Fokker-Planck finite element formulation.

3.2.1 Galerkin Formulation for 1-D Equations

The 1-D Fokker-Planck equation to be solved is chosen in its usual form as in eq.(2.83) with some additional terms. The additional terms include a term of the form Qf and a constant term S . Omitting the subscript a and the constant K , the equation is written as

$$\frac{\partial f}{\partial \tau} = \frac{1}{x^2} \frac{\partial}{\partial x} \left[Af + B \frac{\partial f}{\partial x} \right] + Qf + S, \quad (3.2)$$

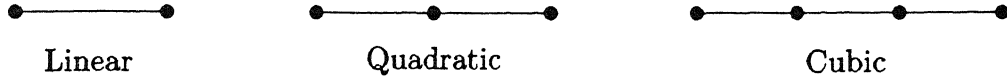


Figure 3.1: One dimensional finite elements

with the boundary conditions

$$\frac{\partial f}{\partial x} = 0 \text{ at } x = 0, \quad (3.3)$$

$$f = 0 \text{ at } x = 1.0. \quad (3.4)$$

Here the computational domain is restricted between 0 and 1.0. Let \bar{f} be the approximate solution to this equation. The residue R can then be written as

$$R = \frac{\partial \bar{f}}{\partial \tau} - \frac{1}{x^2} \frac{\partial}{\partial x} \left[A \bar{f} + B \frac{\partial \bar{f}}{\partial x} \right] - Q \bar{f} - S, \quad (3.5)$$

and its integral with weighting functions W_i is minimized over the entire domain as

$$\int_0^{1.0} W R 4\pi x^2 dx = 0, \quad i = 1, \dots, N, \quad (3.6)$$

The factor $4\pi x^2$ arises out of the governing equation being written in spherical geometry. W_i are chosen as follows: The domain is divided into N_x elements, not necessarily having equal lengths. The number of unknowns at each node is only one. Therefore, linear elements having two nodes are represented by two linear shape functions. Similarly higher order elements namely quadratic, cubic etc. have 3, 4 and more nodes respectively. These elements are represented by the corresponding number of shape functions. In the present work, the nodes are placed in each element at equal intervals for quadratic and cubic elements as shown in Fig. 3.1.

The approximate solution \bar{f}^e at time τ can be written over each element as

$$\bar{f}^e = \sum_{j=1}^m f_j(\tau) \phi_j(x), \quad (3.7)$$

where m is, the number of shape functions or, the number of nodes in each element. Here f_j are functions of time and the shape functions depend only on x . Choosing ϕ_j as weighting functions, the residual equations for an element e with global coordinates x_e and x_{e+1} can be written as

$$\int^e \left[x^2 \frac{\partial \bar{f}}{\partial \tau} - \frac{\partial}{\partial x} \left(A \bar{f} + B \frac{\partial \bar{f}}{\partial x} \right) - Q \bar{f} x^2 - S x^2 \right] \phi_i(x) dx = 0, \quad i = 1, \dots, m, \quad (3.8)$$

for all the shape functions m in the element. Integrating the second term by parts

$$\begin{aligned} & \int^e \phi_i \frac{\partial \bar{f}}{\partial \tau} x^2 dx + \int^e \frac{d\phi_i}{dx} \left(A \bar{f} + B \frac{\partial \bar{f}}{\partial x} \right) dx - \int^e \phi_i Q \bar{f} x^2 dx \\ & - \int^e \phi_i S x^2 dx - \left[\left(A \bar{f} + B \frac{\partial \bar{f}}{\partial x} \right) \phi_i \right]_{x_e}^{x_{e+1}} = 0, \quad i = 1, \dots, m, \end{aligned} \quad (3.9)$$

The contribution of the last term in the left hand side of the above equation vanishes at the boundary nodes. That is, it can be seen that

$$\left(A \bar{f} + B \frac{\partial \bar{f}}{\partial x} \right) \phi_i = 0 \quad \text{at } x = 0 \text{ and } 1.0, \quad (3.10)$$

because A and B are zero at $x = 0$, and $f = 0$ and $B \approx 0$ at $x = 1$. Substitution of eq.(3.7) for \bar{f} in eq.(3.9) leads to

$$\begin{aligned} & \sum_{j=1}^m \left[\left(\int^e \phi_i \phi_j x^2 dx \right) \frac{df_j}{d\tau} + \left(\int^e \frac{d\phi_i}{dx} \left(A \phi_j + B \frac{d\phi_j}{dx} \right) dx \right) f_j(\tau) \right. \\ & \left. - \left(\int^e \phi_i Q \phi_j x^2 dx \right) f_j(\tau) \right] = \int^e \phi_i S x^2 dx \\ & + y_{e+1} - y_e, \quad i = 1, \dots, m, \end{aligned} \quad (3.11)$$

with

$$y_e = \left(A\bar{f} + B\frac{\partial\bar{f}}{\partial x} \right) \phi_i \Big|_{x=x_e}, \quad (3.12)$$

$$y_{e+1} = \left(A\bar{f} + B\frac{\partial\bar{f}}{\partial x} \right) \phi_i \Big|_{x=x_{e+1}}. \quad (3.13)$$

These element equations in matrix form are

$$\mathbf{t} \frac{d\mathbf{f}^e}{d\tau} + \mathbf{u}\mathbf{f}^e(\tau) = \mathbf{v}(\tau), \quad (3.14)$$

where

$$t_{ij} = \int_e \phi_i \phi_j x^2 dx, \quad (3.15)$$

$$u_{ij} = \int_e \frac{d\phi_i}{dx} B \frac{d\phi_j}{dx} dx + \int_e \frac{d\phi_i}{dx} A \phi_j dx - \int_e \phi_i Q \phi_j x^2 dx, \quad (3.16)$$

$$v_i = \int_e \phi_i S x^2 dx + y_e - y_{e+1}. \quad (3.17)$$

The choices of shape functions and elements, and thereafter the computations of the element matrices are discussed in Section 3.2.2. The element equations are generated for all the N_x elements. Finally these equations are assembled to arrive at the global equations. The global equations in matrix form are

$$\mathbf{T} \frac{d\mathbf{f}}{d\tau} + \mathbf{U}\mathbf{f} = \mathbf{V}, \quad (3.18)$$

representing a system of coupled ordinary differential equations. The discretization of spatial part of eq. (3.2) by finite element method has resulted in a system of ordinary differential equations in time. These equations are integrated in time by the one step Θ -method. The boundary conditions are implemented as follows:

1. The derivative condition at $x = 0$ is homogeneous and as such does not contribute to eq. (3.11).

2. The other condition that $f = 0$ at $x = 1.0$, is imposed before solving the global equations.

3.2.2 Computation of Element Matrices

Each entry of the matrices \mathbf{t} , \mathbf{u} and \mathbf{v} in eq. (3.14) requires numerical evaluation of 1-D integrals. A local coordinate ξ between -1 and +1 is used to transform the integrals in order to facilitate the use of Gauss quadrature. Introducing the local variable ξ with the transformation

$$x = \frac{x_h}{2}\xi + \frac{x_e + x_{e+1}}{2}, \quad -1 \leq \xi \leq +1, \quad (3.19)$$

with

$$x_h = x_{e+1} - x_e, \quad (3.20)$$

the equations (3.15)-(3.17) become

$$t_{ij} = \frac{x_h}{2} \int_{-1}^{+1} \phi_i(\xi) \phi_j(\xi) x^2(\xi) d\xi, \quad (3.21)$$

$$\begin{aligned} u_{ij} = & \left(\frac{x_h}{2}\right)^{-1} \int_{-1}^{+1} \frac{d\phi_i}{d\xi}(\xi) B(\xi) \frac{d\phi_j}{d\xi}(\xi) d\xi + \int_{-1}^{+1} \frac{d\phi_i}{d\xi}(\xi) A(\xi) \phi_j(\xi) d\xi \\ & - \frac{x_h}{2} \int_{-1}^{+1} \phi_i(\xi) Q(\xi) \phi_j(\xi) x^2(\xi) d\xi, \end{aligned} \quad (3.22)$$

$$v_i = \frac{x_h}{2} \sum_{j=1}^m S_j \int_{-1}^{+1} \phi_i(\xi) \phi_j(\xi) x^2(\xi) d\xi + y_e - y_{e+1}. \quad (3.23)$$

The 1-D shape functions in terms of the local variable ξ for different elements are given in Appendix B. The integrals are evaluated numerically using Gauss quadrature, which for a general integral is given by

$$\int_{-1}^{+1} z(\xi) d\xi = \sum_{k=1}^{N_g} w_k z(\xi_k), \quad (3.24)$$

where ξ_k and w_k are the Gauss points and weights respectively. The entries in the element matrices given in eqs. (3.21)-(3.23) are calculated by the above procedure.

To evaluate the element matrices, the Fokker-Planck coefficients A and B are needed at each Gauss point ξ_k . These coefficients are not in explicit form for direct computations. Calculating the coefficients accurately at each Gauss point for individual elements at every time step is quite costly and it should possibly be avoided. However, the coefficients can be calculated after every time step at all the nodes in the domain. Then these nodal values can be used to interpolate for any value of ξ_k within each element. In other words, the coefficients A and B are written simply as

$$A^e(\xi) = \sum_{j=1}^m A_j \phi_j(\xi), \quad (3.25)$$

$$B^e(\xi) = \sum_{j=1}^m B_j \phi_j(\xi), \quad (3.26)$$

in terms of the nodal values A_j and B_j and the shape functions ϕ_j . The interpolated values are used in the integrals of element matrices.

Similarly, in the case of source and loss terms, where explicit expressions are not available, e.g. reaction loss, the same procedure has been employed. For example, Q can be written as

$$Q^e(\xi) = \sum_{j=1}^m Q_j \phi_j(\xi), \quad (3.27)$$

where Q_j are the nodal values. In the present case, the above procedure is supported by the fact that the Fokker-Planck coefficients behave smoothly.

With the help of these representations, it is now possible to calculate the element matrices and finally the global matrices \mathbf{T} , \mathbf{U} , \mathbf{V} . This completes the spatial discretization procedure. Next step is to integrate the equations to advance in time.

3.2.3 Time Integration

In the Fokker-Planck equations nonlinearity comes through the potentials which are dependent on the distribution functions f . There are different ways to solve a

system of nonlinear equations. For example

- i. The coefficients at the $n+1$ th step can be obtained by extrapolating the values at steps n and $n - 1$. The resulting linear system is solved.
- ii. The system is treated as quasi-linear. The coefficients are calculated using the distribution functions at the previous time step.

In both the cases, the coefficients can also be iterated over the solutions. In the present work, the method (ii) has been adopted because past researchers have found that the coefficients of Fokker-Planck equations are slowly varying (Killeen and Futch, 1968; McCoy, Mirin and Killeen, 1981) and in general it is not necessary to iterate the coefficients over the solutions. Further, the coefficients are relatively insensitive to the distribution functions because they involve only their integrals. Provisions have, however, been made in the computer codes to iterate the coefficients also. In general, iterations have not shown any appreciable difference in the results obtained.

The temporal part is discretized by standard finite difference techniques. The scheme that has been employed here is generally known as the one step Θ method. This method is chosen because it gives a chance to conduct many numerical experiments by varying Θ values. This can also help to study numerically the stability and convergence aspects of the computed solutions.

The Θ method approximates the time derivative as follows. A weighted average of the time derivatives of the dependent variable f at two consecutive time steps, say n and $n + 1$ is used to interpolate the values of f linearly between the two steps. That is

$$\frac{f^{n+1} - f^n}{\Delta\tau} = \Theta \frac{df^{n+1}}{d\tau} + (1 - \Theta) \frac{df^n}{d\tau}, \quad 0 \leq \Theta \leq 1.0. \quad (3.28)$$

Using this approximation, eq. (3.18) becomes

$$\mathbf{T} \frac{f^{n+1} - f^n}{\Delta\tau} = \Theta(\mathbf{V}^{n+1} - \mathbf{U}f^{n+1}) + (1 - \Theta)(\mathbf{V}^n - \mathbf{U}f^n), \quad (3.29)$$

or,

$$\left(\frac{1}{\Delta\tau}\mathbf{T} + \Theta\mathbf{U}\right)\mathbf{f}^{n+1} = \left(\frac{1}{\Delta\tau}\mathbf{T} - (1 - \Theta)\mathbf{U}\right)\mathbf{f}^n + \left(\Theta\mathbf{V}^{n+1} + (1 - \Theta)\mathbf{V}^n\right). \quad (3.30)$$

The right hand side can be calculated using f at time step n . Now the resulting algebraic system of equations can be written as

$$\mathbf{A}\mathbf{f}^{n+1} = \mathbf{B}, \quad (3.31)$$

where

$$\mathbf{A} = \left(\frac{1}{\Delta\tau}\mathbf{T} + \Theta\mathbf{U}\right), \quad (3.32)$$

$$\mathbf{B} = \left(\frac{1}{\Delta\tau}\mathbf{T} - (1 - \Theta)\mathbf{U}\right)\mathbf{f}^n + \left(\Theta\mathbf{V}^{n+1} + (1 - \Theta)\mathbf{V}^n\right). \quad (3.33)$$

Different values of the parameter Θ lead to the following schemes:

$$\begin{aligned} \Theta &= 0.0 \text{ forward or explicit method } (O(\Delta\tau)) , \\ &= 1/2 \text{ Crank-Nicolson method } (O(\Delta\tau^2)) , \\ &= 2/3 \text{ Galerkin method } (O(\Delta\tau)) , \\ &= 1.0 \text{ backward or fully implicit method } (O(\Delta\tau)) , \end{aligned}$$

where $O(\Delta\tau)$ is the order of convergence of the respective methods.

3.3 Computation of Fokker-Planck Coefficients

The coefficients which appear in the Fokker-Planck collision operators are calculated numerically at the grid points. The collision operators can be written as a sum

$$\left(\frac{\partial f_a}{\partial t}\right)_c = \sum_b \left(\frac{\partial f_a}{\partial t}\right)_c^b, \quad (3.34)$$

where $(\partial f_a / \partial t)_c^b$ represents collision of species a with species b . The contributions from all the general species b including a are accounted as outlined in eqs. (2.88) (2.97) and that of background species are calculated as given in Section 2.3.2. In multi-velocity scale approach numerical approximations that arise primarily are through the Rosenbluth potentials and their derivatives. The computations involve:

- i. numerical evaluation of the integrals M, N, R , and E in eqs. (2.56) (2.59), and
- ii. numerical interpolations which arise out of representing species on different dimensionless velocity scales and grids.

The values of the functionals obtained at grid points are used to calculate the Rosenbluth potentials and their derivatives.

3.3.1 Numerical Quadrature and Interpolation

Various schemes can be used for numerical integration and interpolation. Higher order quadrature and interpolation will naturally lead to improvement in the accuracy of the coefficients. The limits of the integrals in eqs. (2.56) (2.59) can vary by a factor of 40-60 due to difference in the velocity cut-offs. Since x_{max} (maximum cut-off in the normalized velocity) is always 1.0, all these integrals are evaluated first for each species b using its own \bar{v}_b . Then the integral values at the grid points are interpolated for intermediate x values as required by the species a . In this work, two schemes have been implemented for quadrature and interpolation. First one is the trapezoidal rule which is commonly used and easy to implement. In order to improve the accuracy in the calculation of coefficients, a scheme based on cubic polynomials has also been used. In the trapezoidal rule the integral is approximated as

$$\int_{x_k}^{x_l} y(x) dx = \sum_{i=k}^{l-1} \left(\frac{x_{i+1} - x_i}{2} \right) (y(x_{i+1}) + y(x_i)). \quad (3.35)$$

Table 3.1: Fokker-Planck coefficient A_a obtained by using different integration schemes (S)– E-Error function, T-Trapezoidal and H-Hermite

Δx	S	x_2	x_3	x_4	x_5	x_6	x_7	x_8	x_9
1/30	E	0.0446	0.3443	1.095	2.393	4.218	6.449	8.901	11.370
	T	0.0663	0.3836	1.142	2.437	4.251	6.466	8.900	11.350
	H	0.0445	0.3444	1.095	2.392	4.216	6.447	8.898	11.370
1/60	E	0.0056	0.0446	0.148	0.344	0.654	1.095	1.674	2.393
	T	0.0084	0.0501	0.156	0.354	0.665	1.107	1.686	2.404
	H	0.0056	0.0446	0.148	0.344	0.654	1.095	1.674	2.392
1/90	E	0.0017	0.0133	0.045	0.105	0.202	0.344	0.537	0.786
	T	0.0025	0.0149	0.047	0.108	0.206	0.348	0.542	0.791
	H	0.0017	0.0133	0.045	0.105	0.202	0.344	0.537	0.786

In the case of cubic approximation both the Hermite and Lagrangian polynomials have been used, with almost identical results. For the interpolation also, both linear and cubic polynomials have been implemented. It should be mentioned here that 1-D Fokker-Planck coefficients are more easily obtained through eqs. (2.98)–(2.99) than the procedure outlined in eqs. (2.86)–(2.97). In the case of 2-D coefficients the steps discussed above are in principle the same and these steps are repeated for all the orders l of the Legendre polynomials.

3.3.2 Comparison of Accuracy

In order to evaluate the merits of the trapezoidal and Hermite quadratures, Fokker-Planck coefficients are calculated for a single species with Maxwellian distribution. The values of 1-D coefficients A_a and B_a are also obtained accurately by using error function given in Section 2.3.2. The coefficients A_a computed by employing different schemes are shown in Table 3.1. The values are given for the first 9 grid points (excluding $x = 0$, where $A_a = B_a = 0$) corresponding to different mesh sizes Δx . It can be seen that Hermite scheme is more accurate even with less number of grid

points than the trapezoidal rule. Such high accuracy is maintained in the case of multispecies also. Coefficient A_a reaches asymptotic value beyond certain x . So both the schemes produce the same results.

Coefficients B_a which involve the functionals M and E have not shown any significant difference in the low velocity region (near $x = 0$) for both the schemes. This is because the functional M dominates near $x = 0$. Consequently the integral varies slowly in the low velocity region.

3.4 Convergence

Among the various time stepping schemes presented earlier (for different Θ values), Crank-Nicolson and backward (fully implicit) schemes are unconditionally stable for any value of the time step. However the former, although second order accurate, is prone to oscillation in the solutions. Backward and Galerkin schemes are first order accurate and the later is only conditionally stable. Therefore the temporal behavior of these time stepping schemes has to be assessed. Similarly the spatial convergence behavior of the various finite elements must be studied in order to have stable and accurate numerical solutions.

3.4.1 Error Norms and Test Input

An essential part of any computational method is the assessment of the accuracy of the results obtained. For problems related to transport phenomena, in which the conservation of certain quantities is important, density and energy norms of the error in the computed solutions are quite often used. The relative error norms can be defined as follows:

$$e_n = \frac{L_n \text{ norm of } \Delta f}{L_n \text{ norm of } f} = \left[\frac{\int_{\Omega} |\Delta f|^n d\Omega}{\int_{\Omega} f^n d\Omega} \right]^{1/n}, \quad (3.36)$$

with

$$|\Delta f| = |f_{app} - f_{ex}|, \quad (3.37)$$

where f_{ex} and f_{app} are the exact and approximate solutions respectively. Here four types of relative errors namely, e_∞, e_1, e_2 , and e_{rms} corresponding to the L_∞, L_1, L_2 , and L_{rms} norms are defined. For 1-D problems, the errors in percentage are measured as

$$e_\infty = \frac{|\Delta f_i|_{max}}{f_{max}} \times 100, \quad (3.38)$$

$$e_1 = \frac{\int |\Delta f| x^2 dx}{\int f x^2 dx} \times 100, \quad (3.39)$$

$$e_2 = \left[\frac{\int |\Delta f|^2 x^2 dx}{\int f^2 x^2 dx} \right]^{1/2} \times 100, \quad (3.40)$$

$$e_{rms} = \left[\frac{1}{N_x} \sum_i |\Delta f_i|^2 \right]^{1/2} \times 100, \quad (3.41)$$

where the subscript i is over all the nodes in the velocity grid. The L_n norms can also be used to measure the degree of relaxation of of an arbitrary distribution at different times. In this case the f_{ex} represents the Maxwellian distribution to which the initial distribution function is expected to evolve. When used for this purpose the norms are denoted by L_n , and not by e_n .

Test Input

Numerical experiments have been conducted first for a single species in the absence of source and loss terms with Maxwellian and Gaussian distributions. An arbitrary initial distribution (at $\tau = 0$) can be expected to relax to an approximate Maxwellian in about 6τ (τ -relaxation time). The following aspects of evolution are covered in the numerical tests conducted:

- i. If a Maxwellian itself is given as input, the distribution function should not evolve (change) under the action of Fokker-Planck collision operator. However the numerical approximation of the collision operator induces numerical evolution (Succi, Appert, *et al.*, 1986), and the input steady state distribution begins to deviate from the Maxwellian. This occurs due to the contribu-

tions from both spatial and temporal discretization procedures. Keeping the time step constant, by varying the number of grid points, the effect of spatial discretization errors on the artificial (spurious) numerical evolution can be studied.

- ii. When arbitrary initial distributions (used mostly in the form of $(a \exp \frac{1}{2}(x-x_0)^2)$) are allowed to relax for sufficient time, the degree of relaxation to the Maxwellian at the corresponding temperature is studied using the L_n norms defined in eqs. (3.38)–(3.41). These are then referred to as relaxation measures or norms. Such experiments can be used to study numerically the spatial and temporal convergence of various finite elements in the context of the Fokker-Planck equations.

3.4.2 Spatial and Temporal Convergence

In order to ascertain the performance of various finite elements with the time stepping schemes, the results of relaxation of a Gaussian to Maxwellian is presented for a single species in Table 3.2. All the four measures are shown at 10τ (τ -relaxation time) for various finite elements and time integration schemes. The results are shown, in percent, for two different total number of grid points ($N=61$ and 121). It is seen that by the time of 10τ , the species has almost reached the equilibrium state. Since the Crank-Nicolson scheme is second order accurate, its results can be considered to be more accurate (Numerical oscillations were absent in the case of a single species). The table shows that backward scheme slows down the equilibration or relaxation process compared to the Crank-Nicolson scheme except with the linear elements with 61 points, the results of which can be considered to be the least accurate. Galerkin scheme is somewhere in between the other two schemes. Since it is only conditionally stable, this scheme has not been used in later calculations. Among the finite elements, linear elements with 61 grid points show a slightly different trend. Such trends disappear when the $\Delta\tau$ is changed, as shown later in Fig. 3.3. In general, the linear elements do not show consistent behavior with less number of grid points. This is explained in the following paragraphs.

Table 3.2: Relaxation measures in percent of a Gaussian at 10τ with different finite elements and time stepping schemes ($\Delta\tau = 1/16$, L-Linear, Q-Quadratic and C-Cubic)

El.	S	$N = 61$				$N = 121$			
		L_∞	L_1	L_2	L_{rms}	L_∞	L_1	L_2	L_{rms}
L	CN	3.150	1.053	1.102	1.963	0.448	0.352	0.369	0.413
	GA	2.713	0.796	0.832	0.160	0.803	0.584	0.618	0.743
	FI	1.890	0.315	0.334	0.936	1.495	1.030	1.089	1.374
Q	CN	1.967	0.798	0.847	1.249	1.488	0.796	0.847	1.249
	GA	2.337	1.029	1.081	1.572	1.859	1.027	1.087	1.481
	FI	3.033	1.467	1.546	2.183	2.561	1.464	1.544	2.094
C	CN	1.384	0.799	0.850	1.165	1.324	0.796	0.844	1.144
	GA	1.757	1.030	1.092	1.492	1.697	1.027	1.087	1.470
	FI	2.459	1.468	1.549	2.108	2.400	1.464	1.544	2.083

Convergence with Mesh Refinement

The spatial behavior of various elements is assessed by studying the relaxation of a Gaussian distribution for various total number of grid points keeping the time step ($\Delta\tau = 1/16$) constant. The results are shown in the form of L_∞ and L_2 measures at 6τ in Fig. 3.2 for different elements. Crank-Nicolson scheme has been used to obtain the results shown. It is observed that both quadratic and cubic elements closely follow each other. However the linear elements with coarse grid spacing (less number of grid points) are slow in relaxation compared to the other elements which are more accurate. Only on a sufficiently refined grid the relaxation observed using the linear elements is same as that obtained by the higher order elements, indicating convergence. Similar behavior is seen with the backward scheme also.

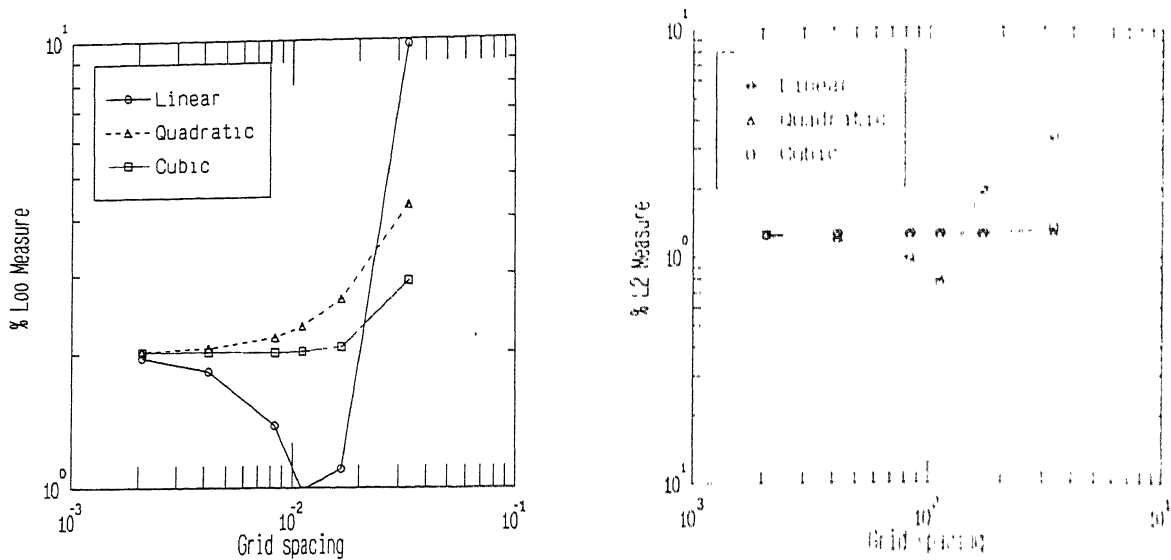


Figure 3.2: L_∞ and L_2 relaxation norms for a Gaussian at 6τ for different grid spacings

Convergence with Time Increment

The temporal behavior of various finite elements is studied in the same manner. For a fixed total number of grid points N , time step was varied from $1/2$ to $1/64$ τ for the Crank-Nicolson scheme. The results are shown in Fig. 3.3 for a single species. Here again the linear elements exhibit a slightly nonuniform behavior. Both the quadratic and cubic elements show good convergence. In general larger time steps slow down the relaxation. As the step size is decreased further the slopes of the measures change slowly indicating a steady state like situation. This kind of behavior is seen when the number of grid points is also varied. It is also true with the backward implicit scheme. These observations suggest that quadratic and cubic elements are better than the linear elements in terms of convergence and accuracy.

The errors that occur in the case of multispecies calculations have also been studied. Two Maxwellian species (D-deuterons and T-tritons) with equal energy were allowed to evolve with a fixed time step $\Delta\tau = 1/16$ and the errors introduced purely due to numerical evolution were studied. The velocity cut-offs were set first to a common value for both species and later to $6v_{th}$ (multi-velocity) for each

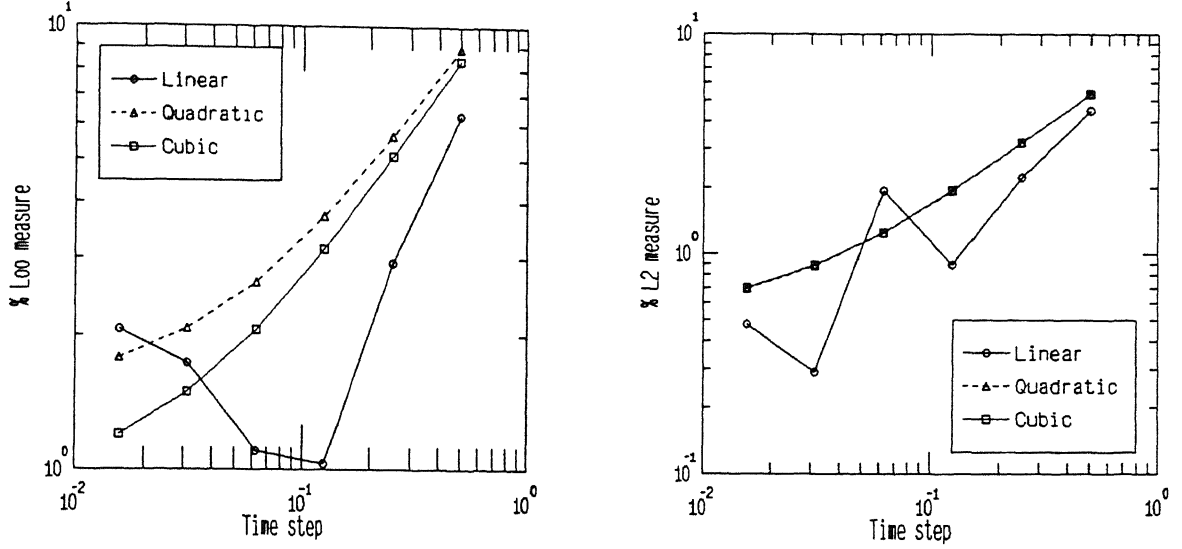


Figure 3.3: L_∞ and L_2 relaxation norms for a Gaussian at 6τ for different time steps

species. The errors are shown in Table 3.3 for the second species T. Error norms indicate that the multi-velocity scale approach has reduced the errors of the species T considerably. This is true with other error norms also. The error norms of D also have shown similar improvements, even though in this case the difference between the cut-off velocities is not large. The reduction in errors with the higher order elements as well as with increasing number of grid points is clearly brought out in this table.

Further to check and validate the implementation of the multi-velocity scale model, equipartition of energy between deuterons and tritons in a D-T plasma has been studied by using both the common and multi-velocity dimensionless scales. Species with different energies at $t = 0$ ($E_D = 75$ keV and $E_T = 15$ keV) were followed for about 0.4 s as shown in Fig. 3.4 using 30 cubic elements ($N = 91$). The equilibration using a common velocity scale is shown in continuous solid and dotted lines. The circles are that of multi-velocity scale model. The results match with each other very well. This confirms the validity and the proper implementation of the multi-velocity scale model. The cumulative error in energy is 0.98% of the total energy for the Crank-Nicolson scheme and is 1.9% for the backward scheme.

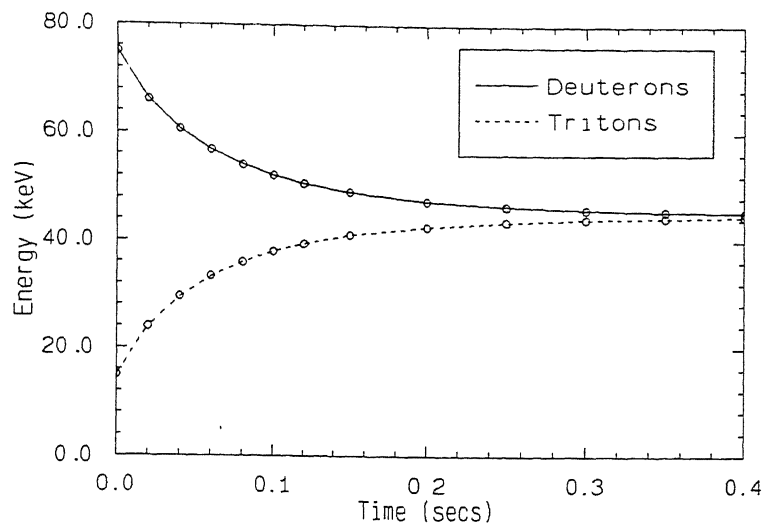


Figure 3.4: Equipartition of energy between deuterons and tritons using different velocity scales

3.5 Computational Aspects

Certain aspects related to density and energy conservation, controlling the time step, and changing the velocity scale of a species during the computation are discussed in this section. These features have been incorporated in the program to avoid cumulative errors in densities and energies and to improve the accuracy of the numerical solution as well as to reduce the number of time steps required.

3.5.1 Density and Energy Conservation

When the Fokker-Planck equations are solved numerically, it is not necessary that both density and energy can be conserved exactly even when large number of grid points and small time steps are used. By choosing proper boundary conditions only one of them can be conserved (Whitney, 1970). When electrons are modeled as a general species, very small time steps are needed. Therefore even small deviations in solutions can propagate further as the species evolve to reach steady state. In order to maintain conservation either special schemes must be devised, or it may be imposed externally. In the present work an attempt has been made to impose

the conservation conditions from outside after every time step, or a fixed number of time steps.

In order to conserve both density and the total energy exactly, it is necessary to slightly alter the computed distributions using a suitable weighting function for each species, i , say $a_i + b w_i(x)$ when $a_i \approx 1.0$, $b \approx 0.0$, as the computed solution is expected to approximately conserve the density and energy. The parameters, a_i and b , equals the number of constraints to be satisfied. In this work $w_i(x)$ are chosen to be Gaussian centered around the instantaneous peak of the the species i . The density and energy constraints in one dimensions are specified as follows

$$\int_0^{1.0} (a_i + b w_i(x)) f_i(x) 4\pi x^2 dx = n_i, \quad (3.42)$$

$$\sum_{i=1}^N m_i \bar{v}_i^2 (a_i + b w_i(x)) f_i(x) 2\pi x^4 dx = \sum_{i=1}^N n_i E_i \quad i = 1, \dots, N \quad (3.43)$$

where N is the number of species. The right hand sides of eqs. (3.42) and (3.43) are the densities and the total energy to which the computed distribution functions are constrained. When source and loss terms are present the conservation of density and energy are maintained in the same way by taking into account the respective loss and gain of individual species.

3.5.2 Controlling the Time Step

In the simulation of multispecies fusion plasmas it is always desirable to have control over the time steps. Adaptive time stepping schemes can be used. In that case species are integrated in time with different time steps. Subsequently the coefficients and the distribution functions have to be interpolated among the species. If implemented successfully adaptive schemes are desirable to study even a simple relaxation of arbitrary distribution to Maxwellian, where the first few relaxation times are more important because by then the spectrum takes the shape of approximate Maxwellian. Later on the distributions relax slowly to reach the actual Maxwellian. In the present work time steps are controlled in the following ways:

- i. Constant dimensionless time steps $\Delta\tau$ are chosen based on the relaxation time of each species which is adjusted if a significant change in the energy of the species occurs during the evolution.
- ii. The time steps $\Delta\tau$ are controlled by the energy norm of the error in the computed solution.

The number of time steps required in the second option depends on the energy accuracy desired. This is elaborated in Chapter 4, where adaptive node distribution in (velocity) space is also studied.

3.5.3 Velocity Scale Refinement

Multi-velocity scale models together with density and energy conservation, and with a strategy for varying the time step, improve the numerical solutions in terms of accuracy and speed. The cut-offs of individual species are chosen based on the energies at $t = 0$ and the expected values in the steady state. If reactions and other auxiliary heating are present, cut-off velocities are chosen to give adequate representation of particles at high energies (tail) as well.

Even with multi-velocity scale approach, as pointed out in Section 2.3, choosing higher cut-offs in the beginning itself to represent species with low energies can introduce erroneous oscillations making the distribution functions negative, especially at the tail end. As the species gain more and more energy due to collisions and other mechanisms such negative values can possibly improve slowly. Therefore if the velocity scales/cut-offs can be refined during evolution such spurious oscillations can be controlled or eliminated. This is particularly important when the electrons are treated as a general species.

A strategy has been used in the present work to refine the velocity scales during evolution. If the change in energy of the species exceeds a specified value, given as input, then the corresponding velocity normalization constant \bar{v}^{old} is modified to a new value \bar{v}^{new} . Correspondingly the distribution function is projected on to the

new grid with the transformations

$$x^{old} \bar{v}^{old} = x^{new} \bar{v}^{new} \quad (3.44)$$

$$f^{new} = \frac{(\bar{v}^{old})^3}{(\bar{v}^{new})^3} f^{old}, \quad (3.45)$$

where f^{old} and f^{new} are the distribution functions on the old and new grids. The projection on the new grid makes use of interpolation. The only problem associated with such refinement scheme is the projection error. This can be easily controlled by using higher order interpolation schemes, if at all needed. It is shown in Chapter 4 that such projection errors are quite negligible.

Refinement of velocity scale can be better illustrated with an example. Again in a D-T plasma, ions with initial energies $E_D = 110$ keV and $E_T = 10$ keV were allowed to equipart the energy over a period of time using: (i) a common velocity cut-off, (ii) different velocity cut-offs resulting in different dimensionless velocity scales, and (iii) different cut-offs with velocity scale refinement (energy increment 5 keV). The non-negative nature of the solutions at every time step is studied by summing up the number of grid points at which the distribution function is negative. The sum of the negative points is obtained for 0.5 s using 250 steps. Numerical experiments were carried out for these three cases for various finite elements and for different total number of grid points N .

The total number of negatives in 250 steps, and the fraction of grid points on which the distribution function becomes negative, are shown in Table 3.4 for all the three cases mentioned above. The advantages of the multi-velocity scale model as well as the velocity scale refinement are self-evident from this table. In order to improve the solutions, in general more number of grid points are needed (Chang and Cooper, 1970; Harrison, 1988). Such a trend is observed here also.

The energy of the deuterons at 0.5 s is shown in Table 3.5 for various cases. It can be seen that the quadratic and cubic elements show acceptable results from the view point of energy exchange even with less number of grid points. Further, it also shows that the velocity scale refinement does not introduce any error in the calculated energy of the species. Thus it may be inferred that the velocity normal-

Table 3.4: Negative values in the spectrum for common and multi-velocity scale models (L-Linear, Q-Quadratic, C-Cubic, and N-Number of nodes)

El.	N	Common		Multi-velocity		With refinement	
		Total	Fraction	Total	Fraction	Total	Fraction
L	31	2286	0.2950	718	0.0926	109	0.0141
	61	3575	0.2344	349	0.0229	21	0.0014
	91	4449	0.1956	16	0.0007	9	0.0004
	121	4960	0.1640	0	0.0	0	0.0
Q	31	1500	0.1935	85	0.0110	12	0.0015
	61	1247	0.0818	84	0.0055	10	0.0007
	91	1387	0.0610	0	0.0	4	0.0002
	121	2127	0.0703	0	0.0	0	0.0
C	31	2296	0.2962	721	0.0930	18	0.0023
	61	3654	0.2396	529	0.0347	10	0.0007
	91	4671	0.2053	332	0.0146	5	0.0002
	121	5383	0.1779	95	0.0031	6	0.0002

Table 3.5: Energy of deuterons at 0.5 s in a D-T plasma obtained by using various finite elements

El.	N	Common	Multi-velocity	With refinement
L	31	66.78	62.18	62.11
	61	62.30	61.49	61.52
	91	61.76	61.42	61.42
	121	61.59	61.40	61.39
Q	31	61.21	61.39	61.33
	61	61.38	61.37	61.35
	91	61.39	61.37	61.34
	121	61.39	61.37	61.34
C	31	61.31	61.34	61.31
	61	61.38	61.37	61.34
	91	61.39	61.37	61.34
	121	61.39	61.37	61.34

ization constants (cut-offs) do contribute to the negative values in the distribution functions, and the choice of velocity cut-offs as well as their refinement during the evolution, can play an important role in the accuracy of the computed solutions.

3.5.4 Structure of the Program

The programs that have been written here are primarily used to solve the Fokker-Planck collision operators based on the finite element method. In addition to the features mentioned above, other aspects like iterating coefficients over the solutions, including source and loss terms, etc. have also been incorporated. The details about source and loss terms are given in Chapter 6. The codes can be used to model an arbitrary number of general and Maxwellian background species, including electrons as a general species. The electron population is modified accordingly to satisfy the macroscopic neutrality. A flow of the algorithm may be visualized broadly in the following sequence:

1. Read in the input data and other control parameters.
2. Calculate density, energy, initial distribution functions, etc.
3. Compute Fokker-Planck coefficients using trapezoidal rule or Hermite scheme as specified.
4. Discretize the equations including source and loss terms and solve the system.
5. Iterate the coefficients, if desired.
6. The following options are included:
 - impose density and energy conservation conditions.
 - use velocity scale refinement.
 - change the size of the time step.
7. Calculate density, energy, and other quantities of interest.
8. Update the data of source and loss terms, if such terms are included.

9. Repeat steps 3 through 8 till the specified exit conditions are satisfied.

3.6 Finite Difference Solutions

The purpose of implementing finite difference method of solution for Fokker-Planck equations is twofold. First, the approach of using different dimensionless velocity scales for different species is tried in this context and compared with the finite element method presented earlier. Secondly, analytical limit of collision operator at the boundary derived in Chapter 2 is also implemented and tested.

In the finite difference method, the derivatives in the governing equations are approximated using finite differences over a numerical grid in the computational domain. Usually the derivatives are approximated with the central differences. This approximation translates the differential equation into a system of algebraic equations. The 1-D Fokker-Planck equations solved, without any source and loss terms, are given in eq. (2.83). The spatial derivatives are discretized accurate to second order. The derivatives are discretized at a node i as

$$\left. \frac{\partial(Af)}{\partial x} \right|_i \approx (A_{i+1} f_{i+1} - A_{i-1} f_{i-1}) / 2\Delta x_i, \quad (3.46)$$

$$\begin{aligned} \left. \frac{\partial}{\partial x} \left(B \frac{\partial f}{\partial x} \right) \right|_i \approx & \frac{1}{\Delta x_i} \left[B_{i+1/2} \left(\frac{f_{i+1} - f_i}{\Delta x_{i+1/2}} \right) \right. \\ & \left. - B_{i-1/2} \left(\frac{f_i - f_{i-1}}{\Delta x_{i-1/2}} \right) \right], \end{aligned} \quad (3.47)$$

where

$$\Delta x_i = \frac{1}{2}(x_{i+1} - x_{i-1}), \quad (3.48)$$

$$\Delta x_{i\pm 1/2} = \pm (x_{i\pm 1} - x_i), \quad (3.49)$$

$$B_{i\pm 1/2} = \frac{1}{2}(B_i + B_{i\pm 1}). \quad (3.50)$$

The above approximations are valid for all the interior nodes, except the boundary

nodes $i = 1$ and $i = I$ at $x = 0$ and $x = 1.0$ respectively.

3.6.1 One Step Θ -Method of Solution

The equation (2.83) is advanced in time from time step n to $n + 1$ using the Θ -method as

$$\frac{f_i^{n+1} - f_i^n}{\Delta\tau} = \Theta \mathcal{L}(f^{n+1}) + (1 - \Theta) \mathcal{L}(f^n), \quad (3.51)$$

where $\mathcal{L}(\cdot)$ is an operator containing the right hand side of eq. (2.83), i.e.

$$\mathcal{L}(f) = \frac{1}{x^2} \frac{\partial}{\partial x} \left[A f + B \frac{\partial f}{\partial x} \right]. \quad (3.52)$$

Finite difference discretization results in the following tridiagonal system

$$\alpha_i f_{i+1} + \beta_i f_i + \gamma_i f_{i-1} = \delta_i. \quad (3.53)$$

The coefficients $\alpha_i, \beta_i, \gamma_i$, and δ_i are given by

$$\alpha_i = -\Theta a_i, \quad (3.54)$$

$$\beta_i = -\Theta b_i, \quad (3.55)$$

$$\gamma_i = -\Theta c_i, \quad (3.56)$$

$$\delta_i = (1 - \Theta)(a_i f_{i+1}^n + b_i f_i^n + c_i f_{i-1}^n) + \frac{1}{\Delta\tau} f_i^n, \quad (3.57)$$

where

$$a_i = \frac{1}{x_i^2 \Delta x_i} \left(\frac{A_{i+1}^n}{2} + \frac{B_{i+1/2}^n}{\Delta x_{i+1/2}} \right), \quad (3.58)$$

$$b_i = \frac{1}{x_i^2 \Delta x_i} \left(\frac{B_{i+1/2}^n}{\Delta x_{i+1/2}} + \frac{B_{i-1/2}^n}{\Delta x_{i-1/2}} \right) + \frac{1}{\Delta\tau}, \quad (3.59)$$

$$c_i = \frac{1}{x_i^2 \Delta x_i} \left(-\frac{A_{i-1}^n}{2} + \frac{B_{i-1/2}^n}{\Delta x_{i-1/2}} \right), \quad (3.60)$$

for $2 \leq i \leq I-1$. The coefficients A and B are evaluated using the values of f at step n . The above system is solved by using a standard tridiagonal algorithm (Richtmyer and Morton, 1967).

3.6.2 Approximation on the Boundary

The boundary nodes need special attention, particularly at $x = 0$ due to the singularity. The Fokker-Planck collision operator at $x = 0$ can be treated either numerically or analytically. Both the treatments are implemented here.

Numerical Approximation

McCoy, Mirin and Killeen (1981) approximated the collision operator at node $i = 1$ numerically and the approximation is given by

$$\frac{1}{x^2} \frac{\partial G}{\partial x} \Big|_{x=0} \approx \frac{3}{x_{3/2}^3} G_{3/2}^{n+1}, \quad (3.61)$$

where $G_{3/2}$ is evaluated at the mid point $x_2/2$. The coefficients of the difference equation at the boundary can be written in terms of

$$\alpha_1 = -\Theta \frac{3}{x_{3/2}^3} \left(\frac{B_2^n + B_1^n}{2\Delta x_{2-1/2}} + \frac{A_2^n + A_1^n}{4} \right), \quad (3.62)$$

$$\beta_1 = -\Theta \frac{3}{x_{3/2}^3} \left(\frac{B_2^n + B_1^n}{2\Delta x_{2-1/2}} - \frac{A_2^n + A_1^n}{4} \right) + \frac{2}{\Delta \tau}, \quad (3.63)$$

and

$$\gamma_1 = 0. \quad (3.64)$$

The coefficient δ_1 is

$$\delta_1 = (1 - \Theta)(\alpha_1 f_2^n + \beta_1 f_1^n) + \frac{1}{\Delta\tau} f_1^n. \quad (3.65)$$

The errors introduced due to numerical evolution for a single species are shown in Fig. 3.5 along with the finite element results. It can be seen that finite difference method is slightly more accurate than the linear elements, whereas the quadratic and cubic elements are much better than the finite difference solutions. This clearly shows that finite element solutions exhibit better spatial resolution. The behavior is the same with all the four error norms. Both Crank-Nicolson and backward schemes have shown negligible difference. Further, the figure shows that as the total number of nodes are increased from 31 to 121 the improvement in the accuracy of solution in the case of finite difference method is slower compared to the finite element method whose accuracy improves by almost two orders of magnitude.

Analytical Approximation

The equation to be solved at the boundary $i = 1$ is eq. (2.113), where $\partial^2 f / \partial x^2$ is approximated as

$$\frac{\partial^2 f}{\partial x^2} = \frac{2(f_2 - f_1)}{(\Delta x_{2-1/2})^2}, \quad (3.66)$$

with the condition $\partial f / \partial x = 0$. The coefficients α_1, β_1 , and γ_1 are given by

$$\alpha_1 = -\Theta \frac{2C^*}{\Delta x_{3/2}}, \quad (3.67)$$

$$\beta_1 = -\Theta \left(A^* - \frac{2C^*}{\Delta x_{3/2}} \right) + \frac{1}{\Delta\tau}, \quad (3.68)$$

$$\gamma_1 = 0, \quad (3.69)$$

and δ_1 is the same as in eq. (3.65).

The results with the above approximation are shown in Fig. 3.6. The approximation based on the analytical limit improves the accuracy (e_∞) of the numerical solution by almost a factor of 2. This trend is seen with e_{rms} also. For a Gaussian

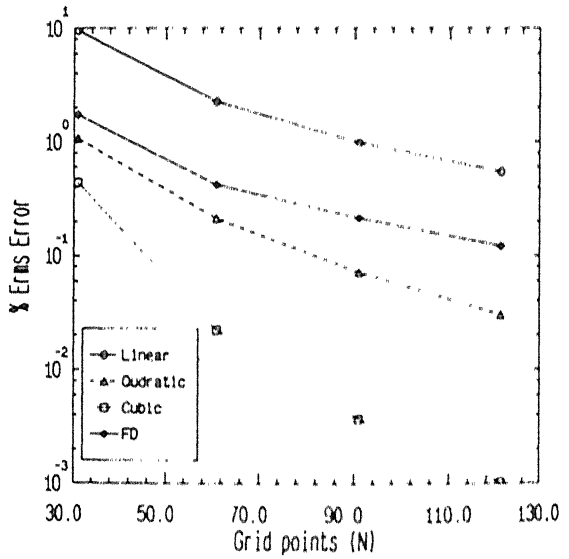
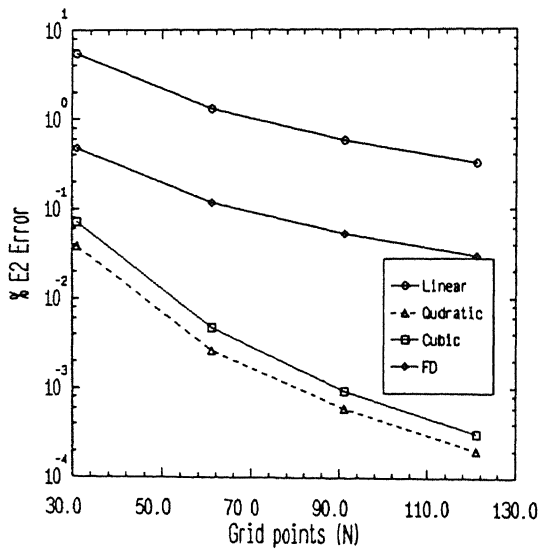
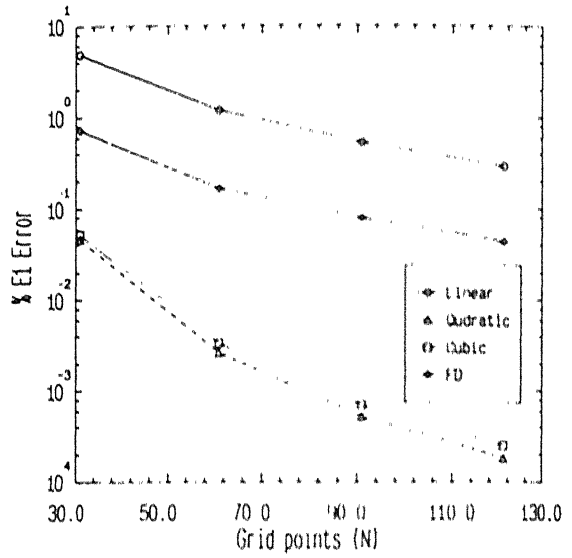
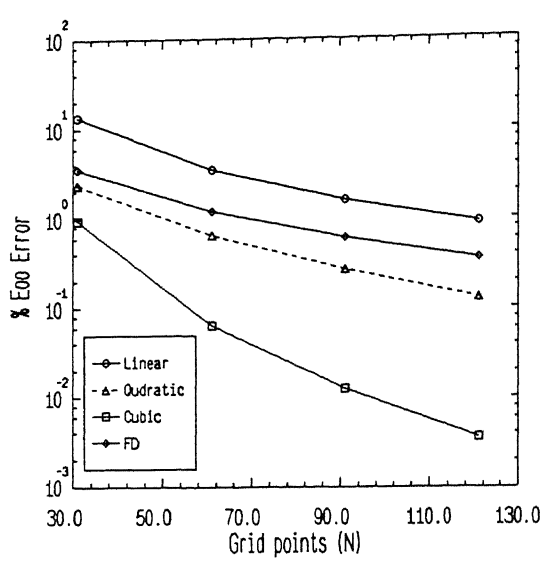


Figure 3.5: Comparison of numerical errors in the finite element and finite difference methods

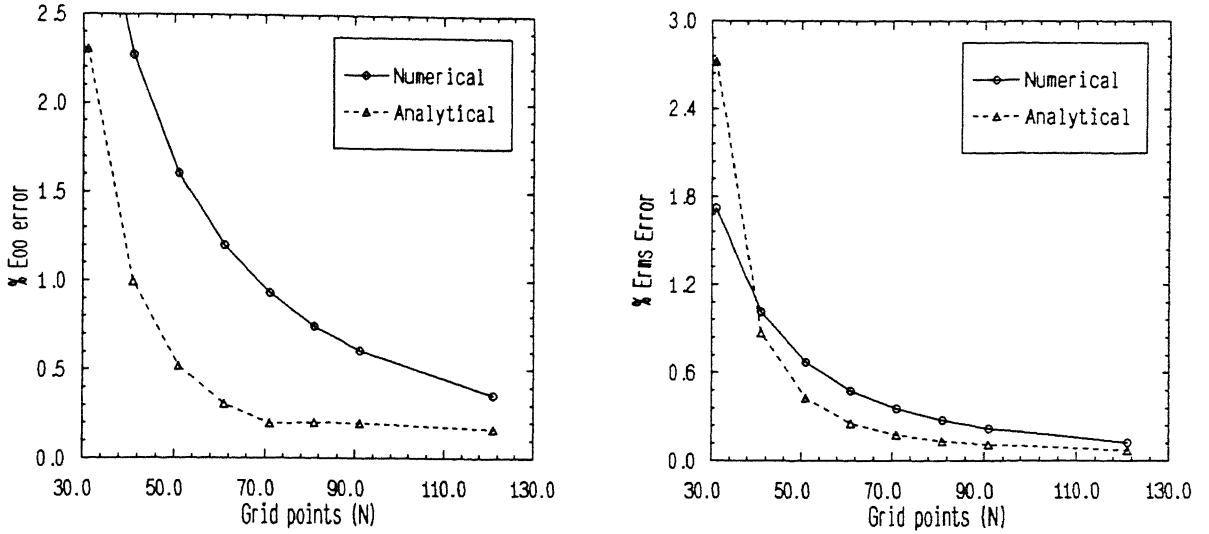


Figure 3.6: e_∞ and e_{rms} errors of numerical and analytical approximations at the boundary for a Maxwellian.

input, the steady state values are given at 6τ in Table 3.6. In this case the analytical approximation has increased L_∞ and L_2 measures of relaxation. This is correct because the numerical approximation at $x = 0$ introduces faster relaxation compared to the one based on analytical limit of the operator at the boundary, whose values are closer to the finite element relaxation norms, which are shown in Table 3.7 for identical input. It can be seen that the norms based on the analytical limit at the boundary are some where between those obtained by the use of quadratic and cubic finite elements.

3.7 Treating Electrons as a General Species

Errors in the numerical solutions for a single species have shown encouraging performance with the multi-velocity scale approach. Nevertheless, when the ion-electron interactions are modeled, the errors caused by the interpolation and integration may be significant, due to large difference in the velocities involved.

To estimate the numerical errors, experiments with two species – ions and electrons – were conducted for about 6 ion τ 's (τ -ion relaxation time) with the im-

Table 3.6: Comparison of relaxation norms at 6τ for a Gaussian input using different approximations at the boundary (CN-Crank-Nicolson, FI-Fully Implicit)

N	<u>Numerical (CN)</u>		<u>Analytical (CN)</u>		<u>Numerical (FI)</u>		<u>Analytical (FI)</u>	
	L_∞	L_{rms}	L_∞	L_{rms}	L_∞	L_{rms}	L_∞	L_{rms}
31	1.720	1.298	3.385	3.244	2.168	1.852	4.271	4.135
41	1.427	1.200	2.345	2.225	2.384	2.080	3.350	3.170
51	1.502	1.308	2.025	1.891	2.522	2.264	3.043	2.857
61	1.576	1.406	1.899	1.763	2.626	2.382	2.942	2.732
71	1.639	1.476	1.851	1.710	2.708	2.459	2.916	2.690
81	1.688	1.526	1.836	1.687	2.772	2.512	2.931	2.669
91	1.729	1.568	1.836	1.678	2.822	2.549	2.975	2.661
121	1.812	1.626	1.862	1.676	2.924	2.611	2.975	2.660

Table 3.7: Relaxation norms at 6τ for a Gaussian input using finite elements

Scheme	N	<u>Linear</u>		<u>Quadratic</u>		<u>Cubic</u>	
		L_∞	L_{rms}	L_∞	L_{rms}	L_∞	L_{rms}
Crank-Nicolson	31	9.767	6.438	4.278	2.455	2.901	2.057
	61	1.105	0.4411	2.640	1.817	2.063	1.739
	91	0.986	0.8970	2.295	1.746	2.015	1.721
	121	1.379	1.250	2.171	1.727	2.009	1.716
Fully implicit	31	8.316	5.115	5.368	3.390	4.010	3.037
	61	1.086	0.972	3.761	2.801	3.195	2.728
	91	2.087	1.910	3.420	2.731	3.147	2.708
	121	2.505	2.253	3.297	2.712	3.139	2.702

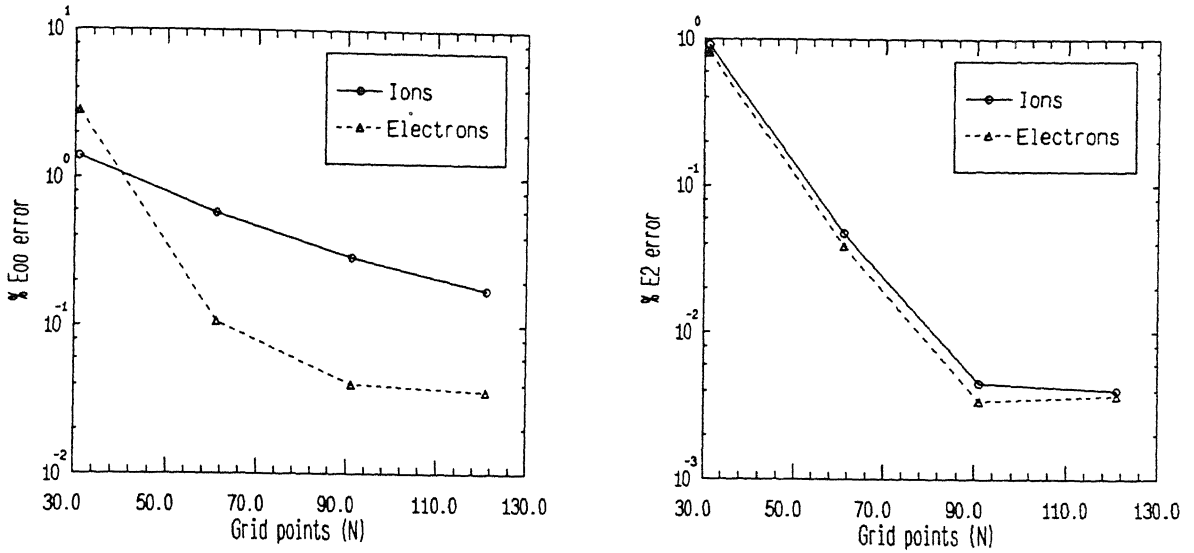


Figure 3.7: e_{∞} and e_2 errors of ions and electrons for a Maxwellian input

position of density and energy conservation conditions. The results are shown in Fig. 3.7 for quadratic elements. Error norms e_{∞} and e_2 indicate that the errors are under control and that the multi-velocity scale model is equally well applicable to model the electrons as a general species.

It may be noted in Fig. 3.7 that the magnitude of errors of the electrons which have larger cut-off is less than that of ions. This is due to the representation of species on different velocity grids. When the Fokker-Planck coefficients are calculated for electrons, the contributions from the ions to each of the points on the electron grid can be obtained easily. On the other hand the converse is not true because the contributions from electrons to almost all the points on the ion grid essentially come from the first few points of the electron grid. This is due to the factor of 40-60 in the velocity cut-offs of electrons and ions. This might give rise to some error in the ion equations. However as the total number of grid points is increased, the difference between the errors of ions and electrons become less, especially in the L_2 error.

Further to study the energy transfer between ions and electrons, a deuterium-electron plasma has been modeled. The Fokker-Planck equations were solved both by the finite element and the finite difference methods. When ions and electrons are

at low temperatures, in the absence of external influences, the energy transfer (relaxation) can be predicted by the Spitzer model approximately (Spitzer Jr., 1962). At low temperatures it may be assumed that the distributions remain Maxwellian during relaxation. However even if one of the species is at high temperature, the distributions will not remain Maxwellian during relaxation. This is because the particles in the low energy region gain more energy from the hot species causing a distortion in the distribution function (Killeen, Heckrotte and Boer, 1962).

Energy transfer between ions and electrons at low temperature has been studied mainly with a view to compare the Spitzer model with the Fokker-Planck results, using the methods developed in this work. According to Spitzer, in a Maxwellian plasma the equipartition of temperature from ions to electrons is governed by

$$\frac{dT_e}{dt} \approx \frac{1}{t_0} \frac{T_D - T_e}{(T_e + (m_e/m_D) T_D)^{3/2}}, \quad (3.70)$$

where the parameter t_0 is given by

$$t_0^{-1} = 1.8 \times 10^{-31} \frac{Z_e^2 Z_D^2 m_e^{1/2} \ln \Lambda}{m_D} s^{-1}, \quad (3.71)$$

and the symbols have their usual meanings. The temperatures are in units of keV and the density in m^{-3} . Equation (3.70) can be integrated easily by using $T_e + T_D = T_0 = (\text{constant})$. The solution is (Prudnikov, Brychkov and Marichev, 1986)

$$t = t_0 \left[\frac{1}{3} (g^{3/2}(0) - g^{3/2}) + e (g^{1/2}(0) - g^{1/2}) + \frac{e^{3/2}}{2} \ln \left| \frac{\Phi(0)}{\Phi(t)} \right| \right], \quad (3.72)$$

with $a = m_e/m_D$, $b = -T_0/2$, $c = (1 - a)$, $d = aT_0$, $e = (d - bc)$, $x = T_e + b$, and $g = (cx + e)$. $\Phi(t)$ is given by

$$\Phi(t) = \frac{(cx(t) + e)^{1/2} - e^{1/2}}{(cx(t) + e)^{1/2} + e^{1/2}}, \quad (3.73)$$

where $\Phi(0)$ is the value of Φ at $t = 0$. The energy transfer from ions to electrons has been studied for a range of $T_D/T_e = 10$ to $T_D/T_e = 100$. For the case of

$T_D/T_e = 100$, both the finite element and the finite difference results are shown in Fig. 3.8. The initial temperatures are $T_D = 4.0$ and $T_e = 0.04$ keV.

The results have been obtained using only 61 grid points. Quadratic and cubic elements have produced the same results. The multi-velocity scale model has made this possible which otherwise would have needed at least 150 points (Whitney, 1970). The figure shows that the Spitzer model is in good agreement with the Fokker-Planck calculations. The maximum difference between the two models is about 6%. In this case both the finite element and the finite difference solutions agree with each other very well.

Energy transfer from electrons to deuterons also has been studied in the same manner. Here the Spitzer model is given by

$$\frac{dT_D}{dt} \approx \frac{1}{t_0} \frac{T_e - T_D}{(T_e + (m_e/m_D) T_D)^{3/2}}. \quad (3.74)$$

The parameter t_0 is given in eq. (3.71). The solution is

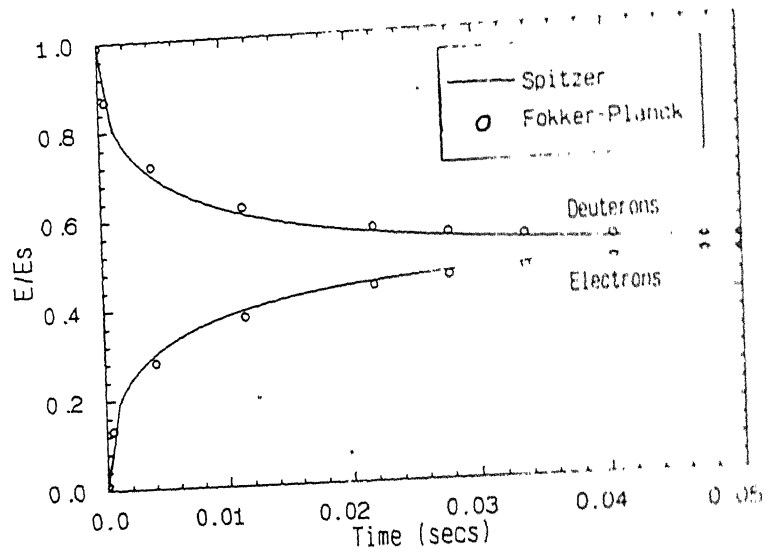
$$t = t_0 \left[\frac{1}{3} (g^{3/2}(0) - g^{3/2}) + b (g^{1/2}(0) - g^{1/2}) + \frac{b^{3/2}}{2} \ln \left| \frac{\Phi(0)}{\Phi(t)} \right| \right], \quad (3.75)$$

with $a = m_e/m_D$, $b = (1 + a)T_0/2$, $c = (1 - a)/2$, $x = T_0 - 2T_D$, and $g = (cx + b)$. $\Phi(t)$ is given by

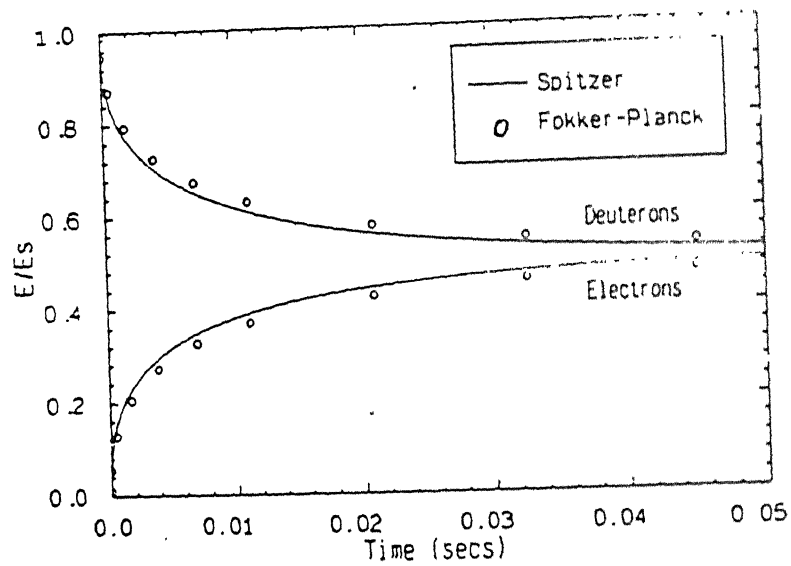
$$\Phi(t) = \frac{(cx(t) + b)^{1/2} - b^{1/2}}{(cx(t) + b)^{1/2} + b^{1/2}}. \quad (3.76)$$

Here also the temperature ratio T_D/T_e was varied from 0.1 to 0.01. Keeping other inputs the same, the result of a test case is shown in Fig. 3.9 for the initial temperatures $T_D = 0.04$ keV and $T_e = 4.0$ keV. In this case too the Spitzer model is in very good agreement with the results of the finite element method. The maximum difference in the finite difference case is about 8%. Therefore it can be concluded that the Spitzer model predicts the energy relaxation under Maxwellian conditions adequately.

Further a study of energy transfer from hot ions to cold electrons and vice versa has also been made using the multi-velocity scale Fokker-Planck equations. Ions

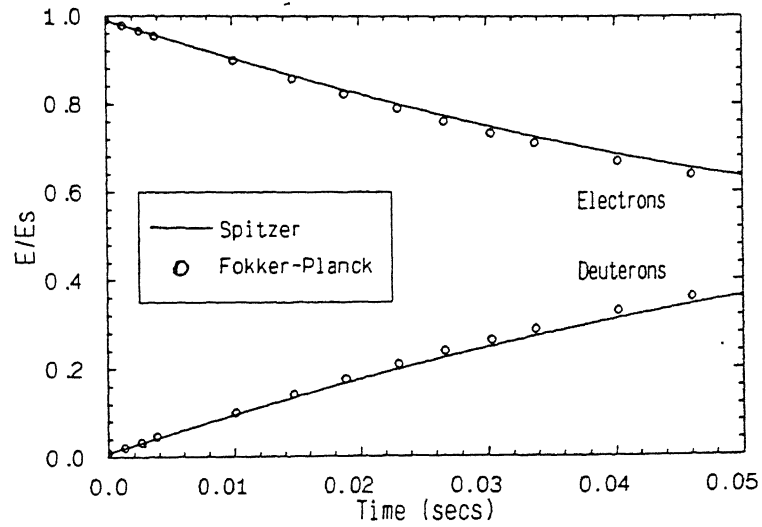


a) Finite element method

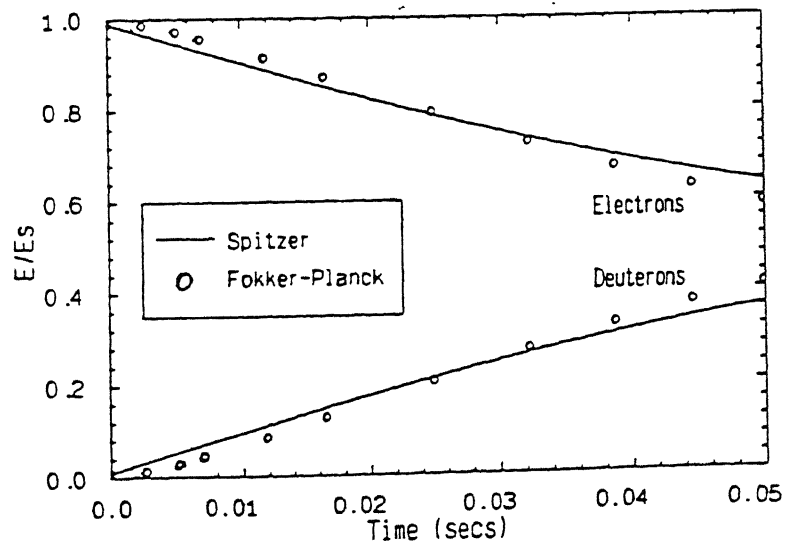


b) Finite difference method

Figure 3.8: Energy transfer from deuterons to electrons at low temperatures



a) Finite element method



b) Finite difference method

Figure 3.9: Energy transfer from electrons to ions at low temperatures

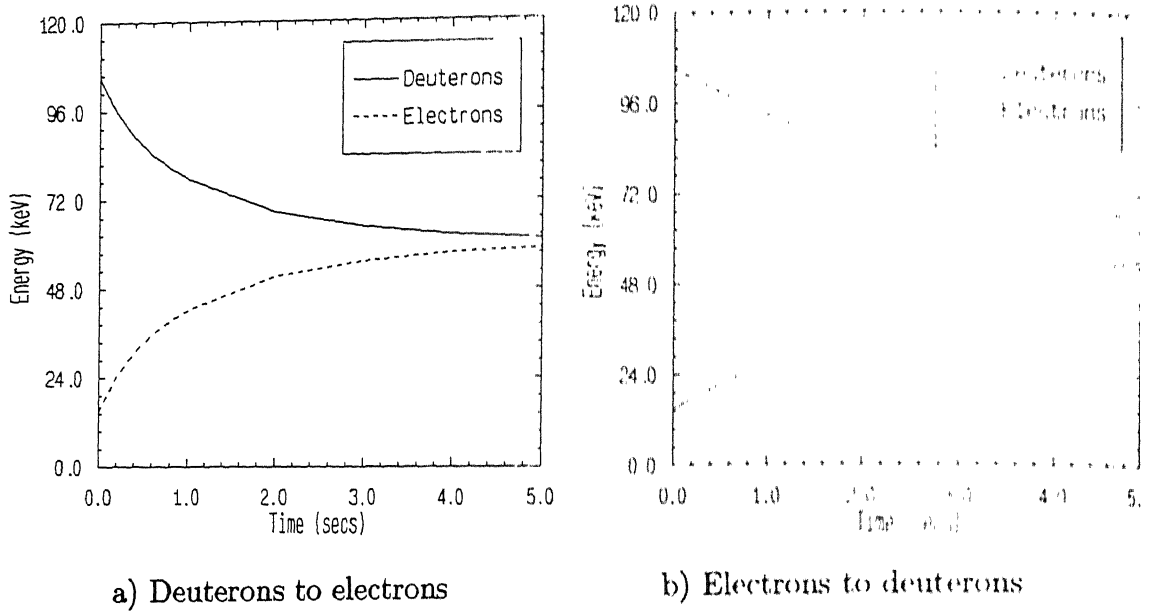


Figure 3.10: Energy transfer between ions and electrons Finite element method

with 105 keV and electrons with an initial energy of 15 keV were allowed to equipart the energy for about 5 s. Total energy and density are conserved in all the cases presented here. The results are presented in Figs. 3.10 and 3.11 for the finite element and the finite difference methods, respectively. In general both the methods closely follow each other. However, in the case of the finite difference method, to obtain the results similar to the finite element method, the total number of grid points had to be increased from 61 to 121.

The studies have shown that to improve the accuracy of the finite difference solutions in general more number of points are needed. On the other hand the finite element method is able to produce accurate results with less number of elements. The CPU time of the various finite elements and the finite difference method are given in Table 3.8. The run times given are on the CONVEX-220 system with O1 level optimization. CPU times are shown for options (I) and (II). In (II), the energy and density constraints as explained in Section 3.5.1 are imposed. It shows that the imposition of these conditions, which requires the evaluation of a few integrals at each time step, consumes a reasonable fraction of the total time.

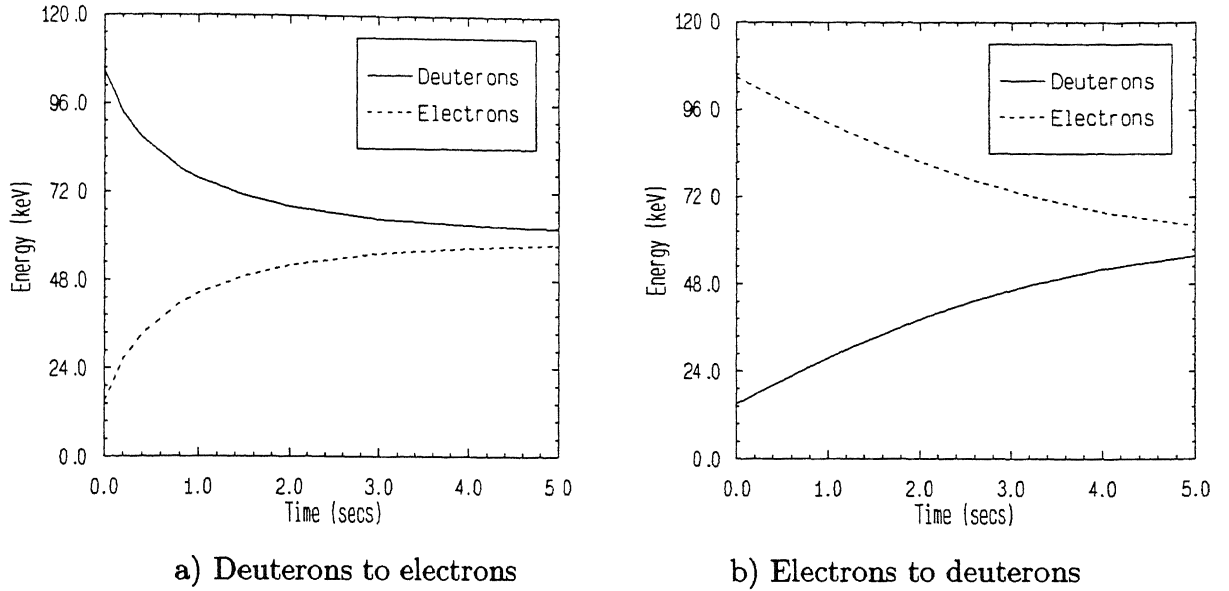


Figure 3.11: Energy transfer between ions and electrons—Finite difference method

It can be seen that although the finite element method takes about twice the time as compared to the finite difference method for the same number of nodes, the improvement in accuracy is much more. This can also be seen from Fig. 3.5. When the number of nodes are increased from 31 to 121 the errors in the finite difference method are reduced by less than a factor of 10, while the finite element method shows an improvement by almost two orders of magnitude. This indicates that the spatial resolution of the numerical solution of the Fokker-Planck equations based on the finite element method is better than the finite difference method.

3.8 Summary

The experience in this chapter has shown that the solution of multi-velocity scale Fokker-Planck equations based on the finite element method can be very useful in the area of numerical modeling of fusion plasmas. It is found that for the same computational effort the finite element method performs better than the finite difference method. The work reported in this chapter can be summarized as follows:

Table 3.8: CPU times in minutes for the finite element (FE) and the finite difference (FD) methods

Option	N	Linear	Quadratic	Cubic	FD
I	31	2.3	2.1	2.3	1.0
	61	4.9	4.4	4.9	2.3
	91	7.8	7.0	7.8	3.9
	121	11.0	10.0	11.0	5.9
II	31	3.0	2.8	3.1	1.7
	61	6.3	5.8	6.3	3.7
	91	9.9	9.1	9.9	6.0
	121	13.8	12.8	13.8	8.6

- i. Multi-velocity scale Fokker-Planck equations in 1-D have been solved by both the finite element and finite difference methods.
- ii. Strategies have been presented to vary the time steps and also to satisfy the conservation of both density and energy at every step.
- iii. It is found that the choices of velocity normalization constants (cut-offs) do improve the non-negative nature of the numerical solutions significantly. Further, varying the cut-offs during the course of evolution of plasma also reduces the problem of solutions becoming negative at the tail.
- iv. Quadratic and cubic finite elements are better than the linear elements in terms of convergence and computational accuracy.
- v. Electrons have been treated as a general species together with ions. Using the multi-velocity scale model, the energy transfer between ions and electrons has been studied using same number of grid points. The results of Spitzer model which is valid under Maxwellian approximation have been found to be in good agreement with the Fokker-Planck solutions.

Chapter 4

Discretization Errors and Optimal Distribution of Nodes

4.1 Introduction

When a dimensionless velocity scale characteristic to each species is used in the simulation of multispecies plasmas, the relevant velocity ranges are better modeled even with a uniform distribution of nodes. With this approach, the set of nodes for the species with the largest velocity cut-off, say electrons, need not be the union of nodes for other species plus additional nodes to cover the remaining part of the electron velocity. The number of nodes for each species can be chosen independently, and if desired, the same number of nodes can be used for all the species. The nodes, however, do not correspond to the same physical velocities, and appropriate interpolations are required for calculating the Fokker-Planck coefficients. The fact that this approach can be successfully exploited both in the finite element method and the finite difference method has been demonstrated in the previous two chapters.

Distribution functions, however, vary by a few orders of magnitude even when a dimensionless velocity scale most appropriate for each species is considered. Consequently, the discretization errors associated with a uniform distribution of nodes show a large variation. In this chapter, the local discretization/truncation errors are studied for typical distribution functions encountered in the simulation of fusion plasmas. These include the equilibrium Maxwellian distributions and the Gaussian

distributions which can be used for the characterization of fast ions or reaction products. Redistribution of nodes with a view to minimize the errors and achieve a more uniform error distribution is discussed. Where possible, exact errors are compared with the computed errors. Errors for ions and electrons are compared, both on a uniform grid as well as on an optimal grid. An adaptive time stepping scheme based on the norm of the energy error, as mentioned in Section 3.5.2 is also implemented.

4.2 Error Estimates

The Fokker-Planck equation used in this chapter is in the form of eq. (2.104):

$$\frac{\partial f}{\partial \tau} = A^* f + B^* \frac{\partial f}{\partial x} + C^* \frac{\partial^2 f}{\partial x^2}, \quad (4.1)$$

$$= \mathcal{L}(f), \quad (4.2)$$

where A^* , B^* , and C^* are as in Chapter 2 (eqs. 2.105 - 2.107), and \mathcal{L} denotes the operator on the right hand side. Three different methods to estimate the nodal errors were considered:

- i. Developing the truncation error term for the operator \mathcal{L} analytically in terms of the higher order derivatives,
- ii. Use of higher-order finite difference formulae in conjunction with the central difference formulae for approximating the operator \mathcal{L} and treating the difference as the error estimate, and
- iii. Approximating the operator \mathcal{L} on a fine and a coarse grid, and treating the difference as the error estimate.

The first method requires the computation of the higher order derivatives. Furthermore, analytical expressions for the leading terms in the truncation error(s) become intractable on a non-uniform grid except for the standard three-point central difference schemes. Comparison of error estimates with exact errors, which can be

done at $t = 0$ (see Section 4.4) has shown that generally the estimates obtained by method (iii) are more accurate as compared to those obtained by the methods (i) and (ii). Method (iii) is also the simplest to use. It is this method which has been used in this work, and can be explained as follows. Let $\mathcal{L}_{\Delta x}$ and $\mathcal{L}_{2\Delta x}$ be the two approximations of the operator \mathcal{L} on the fine and the coarse grids respectively. If $\epsilon_{\Delta x}$ and $\epsilon_{2\Delta x}$ are the corresponding discretization/truncation errors, and n the order of convergence for the discretization scheme, then

$$\frac{\partial f}{\partial \tau} = \mathcal{L}_{\Delta x}(f) + \epsilon_{\Delta x}, \quad (4.3)$$

$$= \mathcal{L}_{2\Delta x}(f) + \epsilon_{2\Delta x}, \quad (4.4)$$

where

$$\epsilon_{\Delta x} = C\Delta x^n, \quad (4.5)$$

$$\epsilon_{2\Delta x} = C(2\Delta x)^n = 2^n \epsilon_{\Delta x}. \quad (4.6)$$

Subtracting eq. (4.3) from eq. (4.4), and using eq. (4.6),

$$|\epsilon_{\Delta x}| = \left| \frac{\mathcal{L}_{\Delta x} - \mathcal{L}_{2\Delta x}}{2^n - 1} \right|. \quad (4.7)$$

For obtaining $\mathcal{L}_{2\Delta x}$, alternate points are skipped from the fine grid.

4.3 Redistribution of Nodes

The purpose of redistribution of nodes is the minimization of ϵ_{max} and a more uniform distribution of the discretization errors. The optimal distribution is obtained by iteratively adjusting the grid spacing in inverse proportion to $\epsilon^{1/n}$, where n is the order of convergence. Since the nodes in the present work are distributed on the dimensionless velocity scale extending from $x = 0$ to 1.0, the relation giving the new nodal distribution (spacing) $\Delta x'_i$ in terms of the old distribution Δx_i can be written as

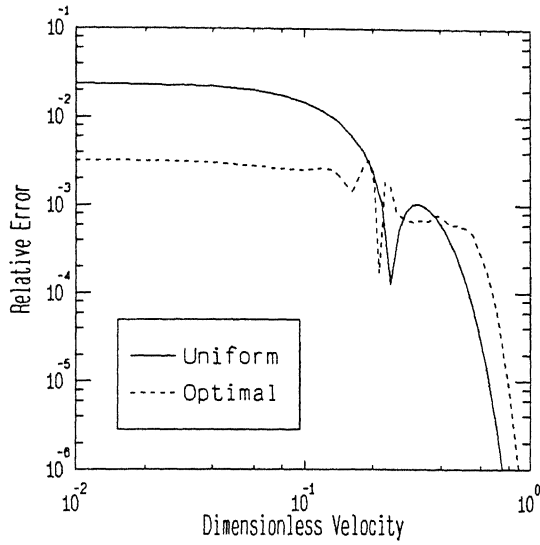
$$\Delta x'_i = \frac{\Delta x_i / |\epsilon_i|^{1/n}}{\sum_{i=1}^I \Delta x_i / |\epsilon_i|^{1/n}}. \quad (4.8)$$

Starting from a uniform grid at $t = 0$, generally 4 to 5 iterations based on eq. (4.8) are required to minimize ϵ_{max} . At later time steps one iteration, after a fixed number of time steps or time of integration is found to be adequate. If the error ϵ_i for a particular node i is below a certain cut-off limit, it is this limit which is used to avoid excessively large grid spacing around such nodes.

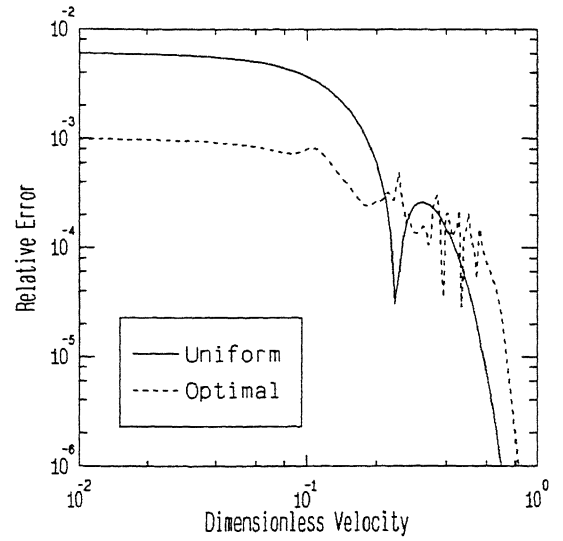
Figures 4.1, 4.2, and 4.3 present the results obtained with 51 and 101 nodes, using both the standard as well as higher order five-point difference formulae based on Lagrangian polynomials. Figures 4.1 and 4.2 show the distribution of relative nodal errors (ϵ_i/f_{max}) on the uniform and the optimal grid for a Maxwellian distribution function. It is seen that the maximum discretization error on the optimal grid is reduced by a factor of about 7 in the case of three-point approximation, and by more than an order of magnitude in the case of five-point approximation. The results are similar for a Gaussian distribution which are shown in Fig. 4.3. It should be mentioned here that the error distribution shows a number of maxima and minima both on the uniform and the optimal grid. This is due to the highly complex and nonlinear nature of eq. (4.1) where the coefficients A^* , B^* , and C^* involve various derivatives of the Rosenbluth potentials. Further the truncation error for the second and third terms in eq. (4.1) combine differently at different points on the grid, leading to addition or cancellation. More iterations of eq. (4.8) generally do not reduce such fluctuations even on the optimal grid. Fig. 4.4 shows the actual distribution of nodes after five iterations of eq. (4.8) for a Maxwellian and a Gaussian distribution.

4.4 Exact and Computed Errors

The redistribution of nodes shown in Figs. 4.1-4.3 has been based on the error estimates obtained using a fine and a coarse grid as explained in Section 4.2. In order to check the reliability of these estimates for uniform as well as non-uniform node distributions, exact discretization errors at $t = 0$ for known distribution functions

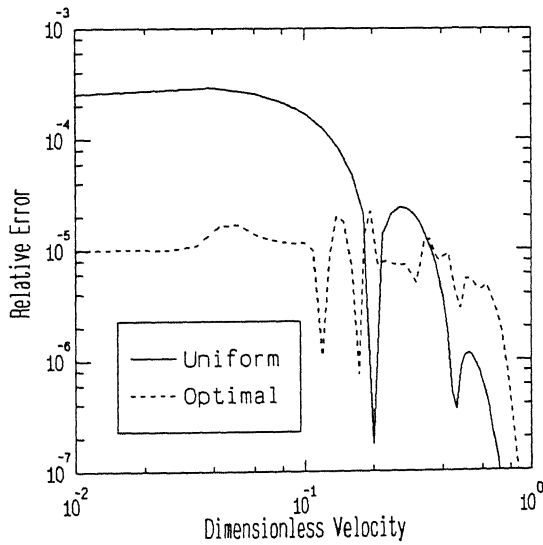


a) 51 nodes

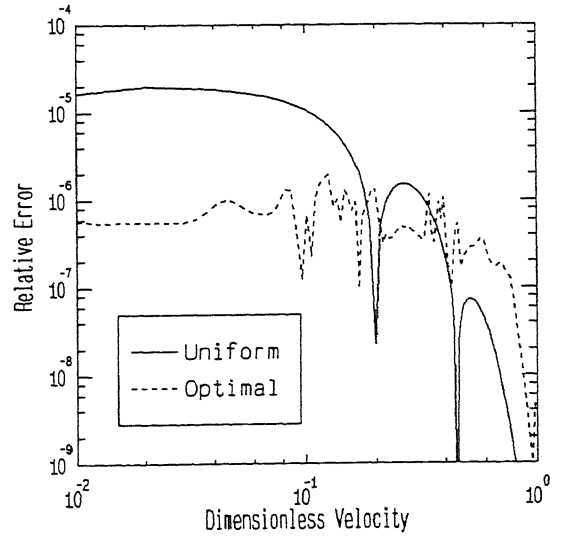


b) 101 nodes

Figure 4.1: Comparison of discretization errors for a Maxwellian distribution on uniform and optimal grids using standard three-point central difference formula

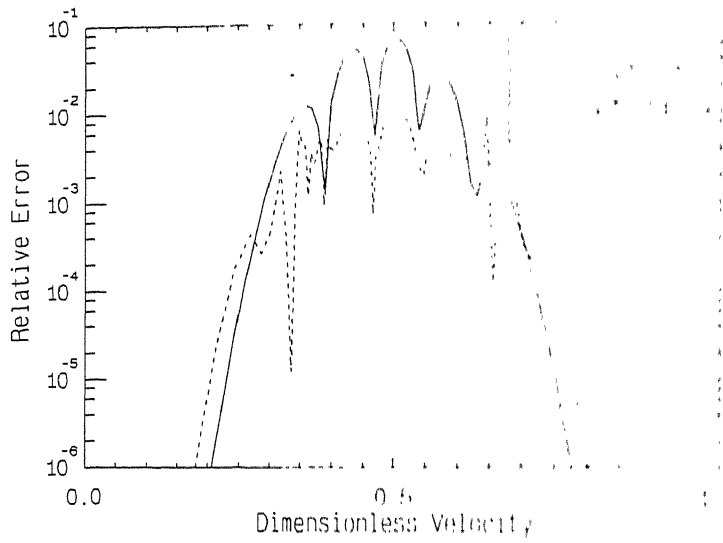


a) 51 nodes

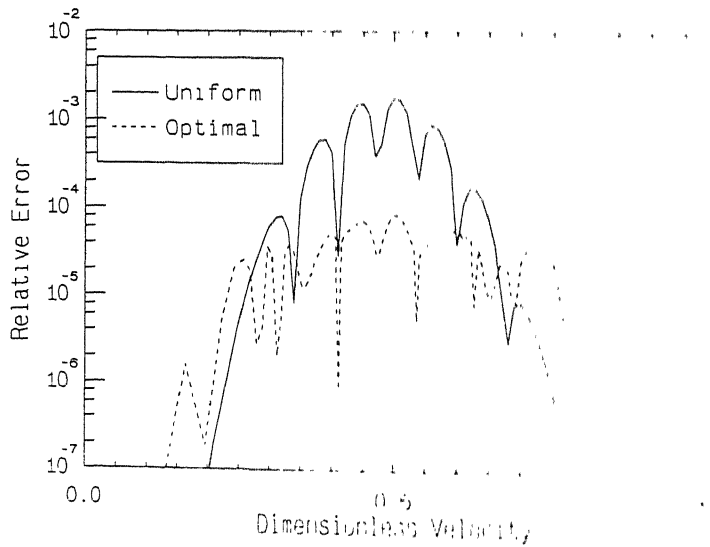


b) 101 nodes

Figure 4.2: Comparison of discretization errors for a Maxwellian distribution on uniform and optimal grids using a five-point difference formula based on Lagrangian polynomials

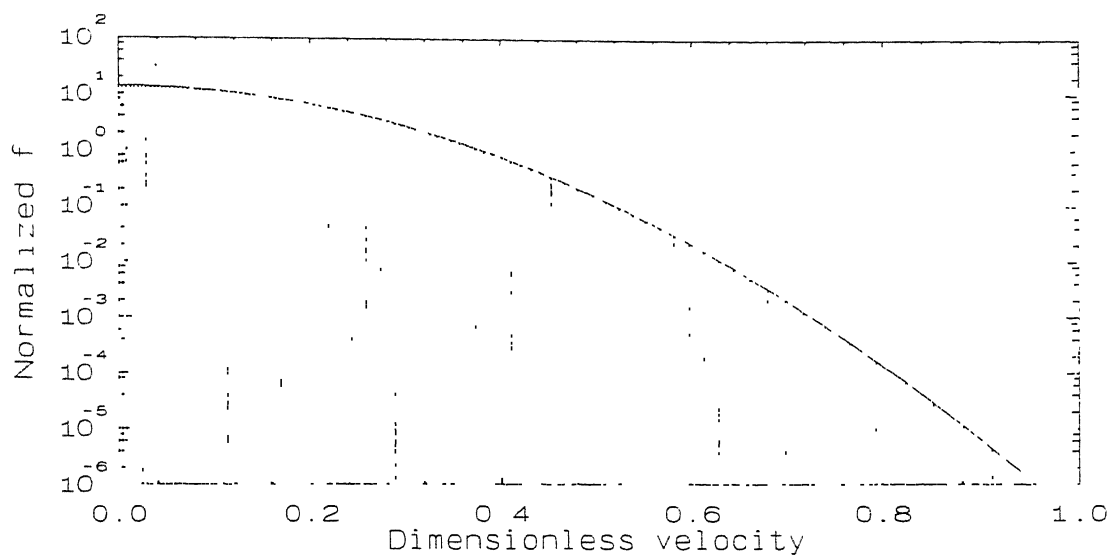


a) Three-point central difference formula

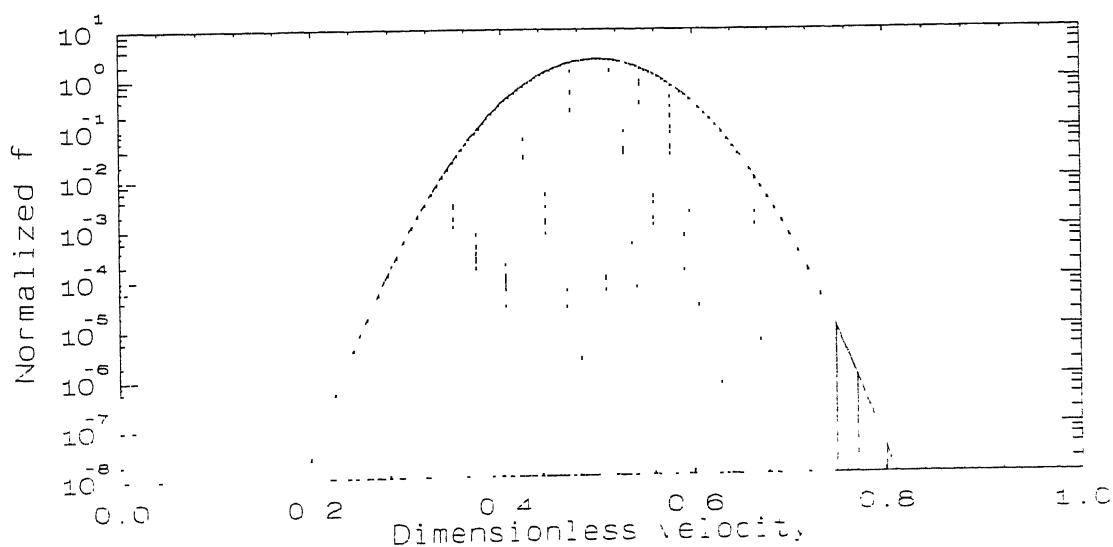


b) Five-point difference formula

Figure 4.3: Discretization errors for a Gaussian distribution on a uniform and optimal grid with 101 nodes



a) Maxwellian



b) Gaussian

Figure 4.4: Optimal distribution of nodes for two different distribution functions (101 nodes)

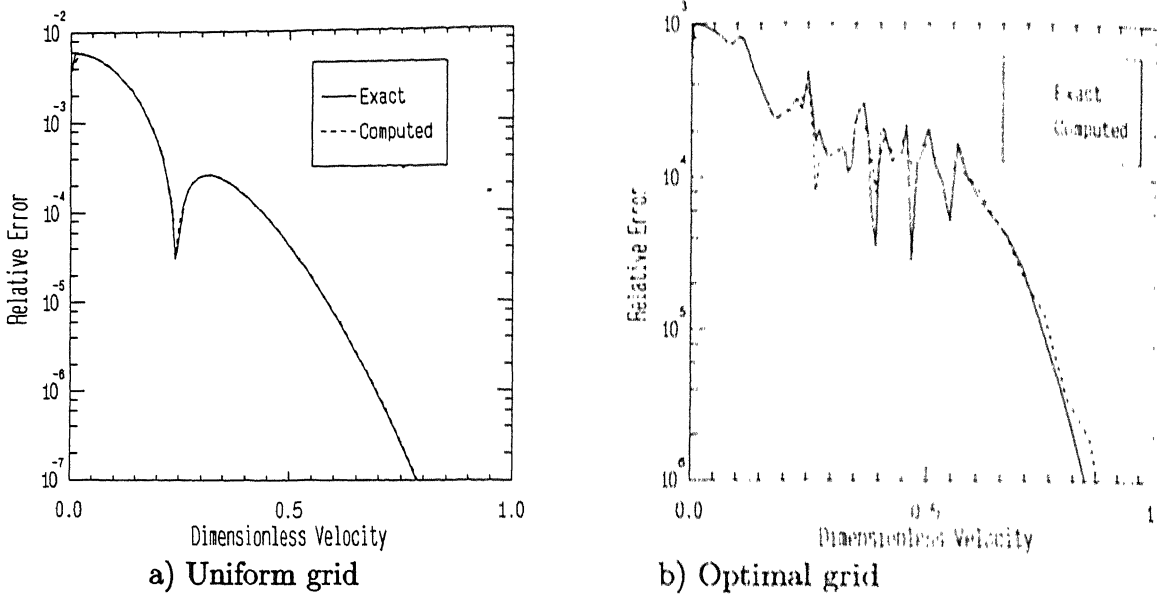
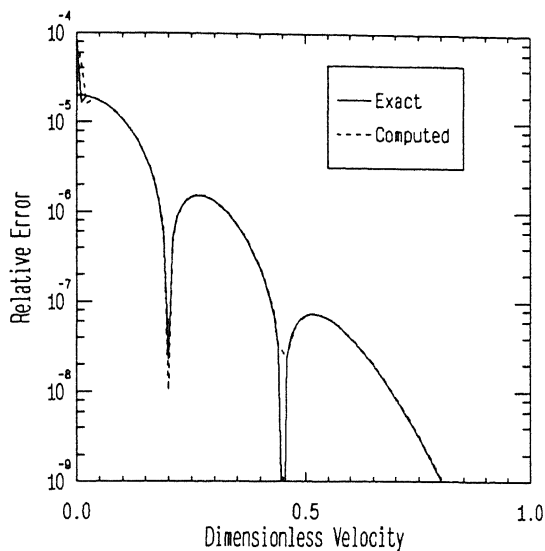


Figure 4.5: Comparison of exact and estimated errors for a Maxwellian distribution using central differences

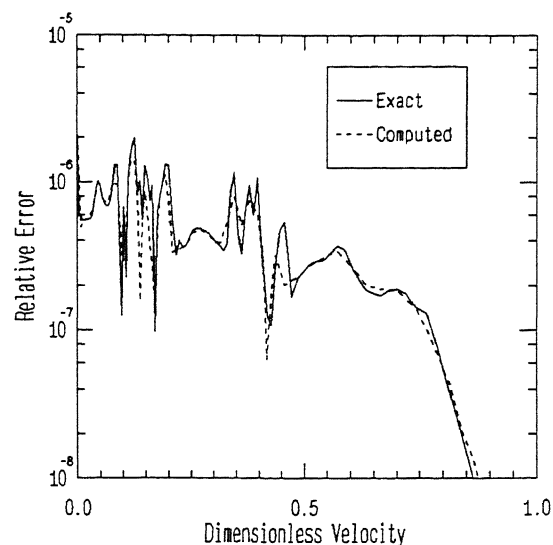
were computed. For the Maxwellian distribution $\mathcal{L}(f) = 0$, and therefore $|\mathcal{L}_{\Delta x}(f)|$ itself can be treated as the exact error. For a Gaussian distribution, the exact values of $\mathcal{L}(f)$ can be obtained using analytical integrations. This however is quite involved. Instead, a 12-point Gauss quadrature together with analytical values of the derivatives were used to calculate exact $\mathcal{L}(f)$. Comparisons with $\mathcal{L}_{\Delta x}(f)$ yields the exact $\epsilon_{\Delta x}$. This is then compared with the estimates obtained by using the fine and coarse grids.

The results are shown in Figs. 4.5, 4.6, 4.7, and 4.8. It can be seen that the exact errors compare quite well with the estimated errors. In these figures, the two errors have been normalized to agree at the point (node) of maximum error. In the redistribution of nodes, it is the relative variation of the error along the nodes which is of consequence. The good agreement between the exact and the estimated errors indicates that the estimated errors can be used effectively for the purpose of node redistribution to obtain an optimal grid initially, and for changing it at subsequent steps during the evolution.

Figure 4.9 shows the variation of L_{max} error, i.e., ϵ_{max} , for different average grid

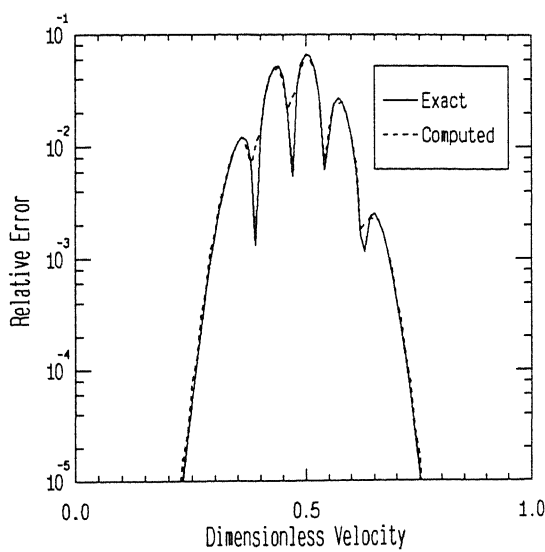


a) Uniform grid

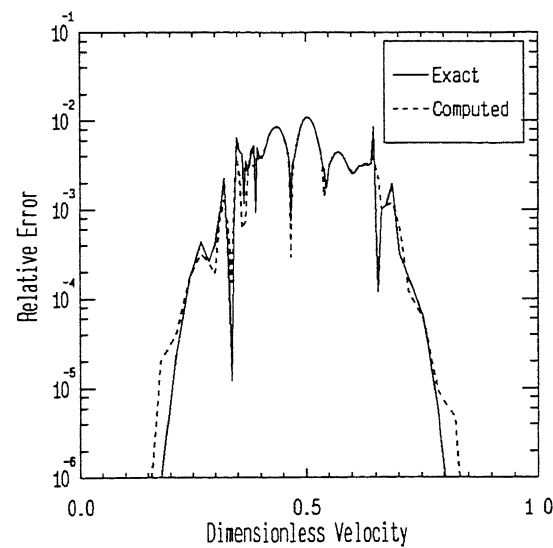


b) Optimal grid

Figure 4.6: Exact and estimated errors for a Maxwellian distribution using five-point difference formula



a) Uniform grid



b) Optimal grid

Figure 4.7: Comparison of exact and estimated errors for a Gaussian distribution using central differences

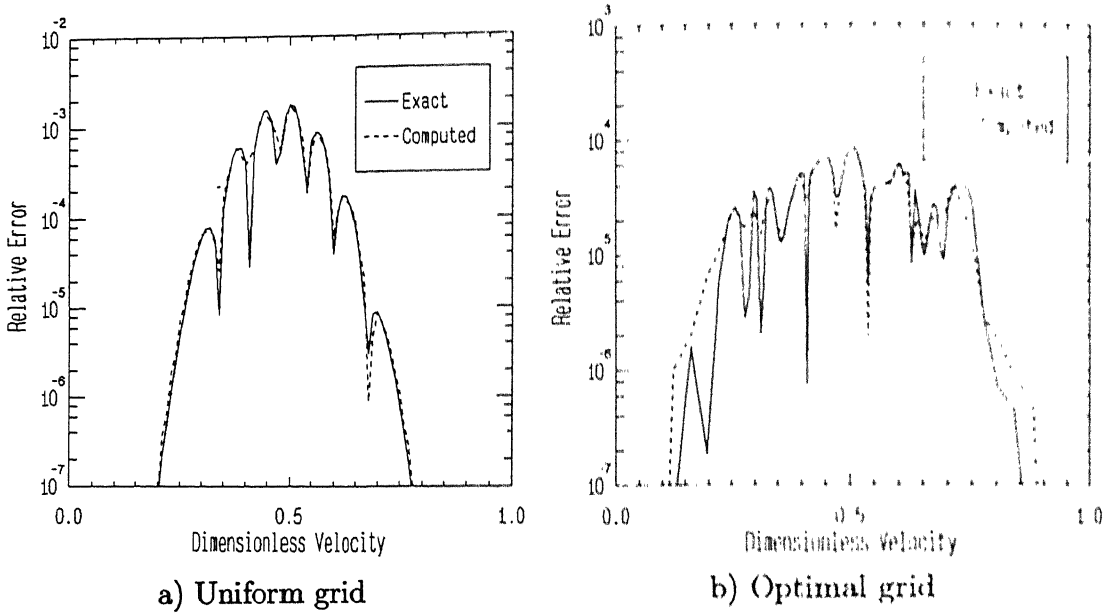
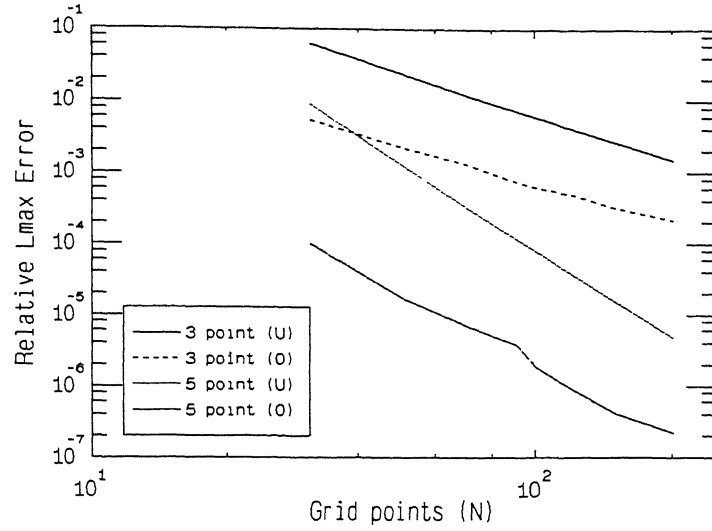
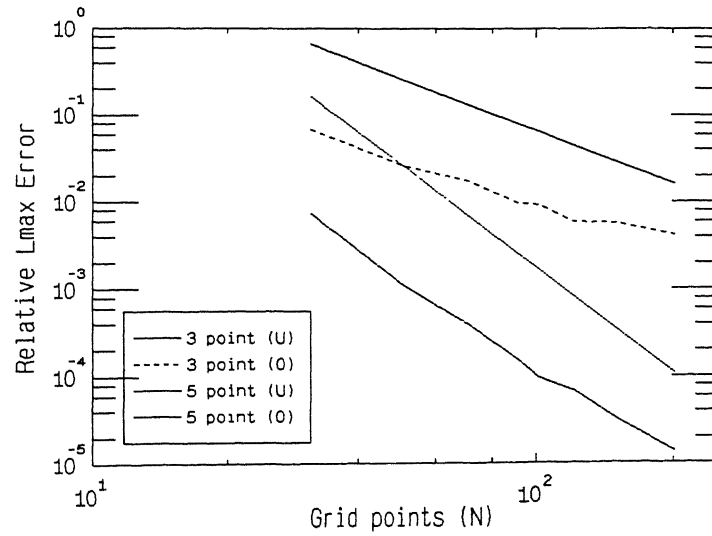


Figure 4.8: Exact and estimated errors for a Gaussian distribution using higher order difference formulae

spacings on the uniform and optimal grids. The reduction in discretization errors achieved by an optimal distribution of nodes is clearly brought out in this figure for all values of the grid spacing. The order of convergence n both for the three-point and five-point finite difference formulae can be estimated from this figure. It is found to be ≈ 2 for the first case and varies between 3 and 4 for the second case. It may be mentioned here that the number of iterations required based on eq. (4.8) are relatively insensitive to the exact value of n . Further, the exact value of n is not required in eq. (4.7), as only the relative distribution of the errors is of consequence. Finally, Fig. 4.10 compares the errors for a Maxwellian distribution with a large velocity cut-off, which is sometimes needed to represent a background cold plasma species. It is seen that the reduction in ϵ_{max} is significantly larger (more than two orders of magnitude) in this case if an optimal grid is used.



a) For a Maxwellian distribution



b) For a Gaussian distribution

Figure 4.9: Variation of L_{\max} error with grid spacing: (U) Uniform grid, (O) Optimal grid

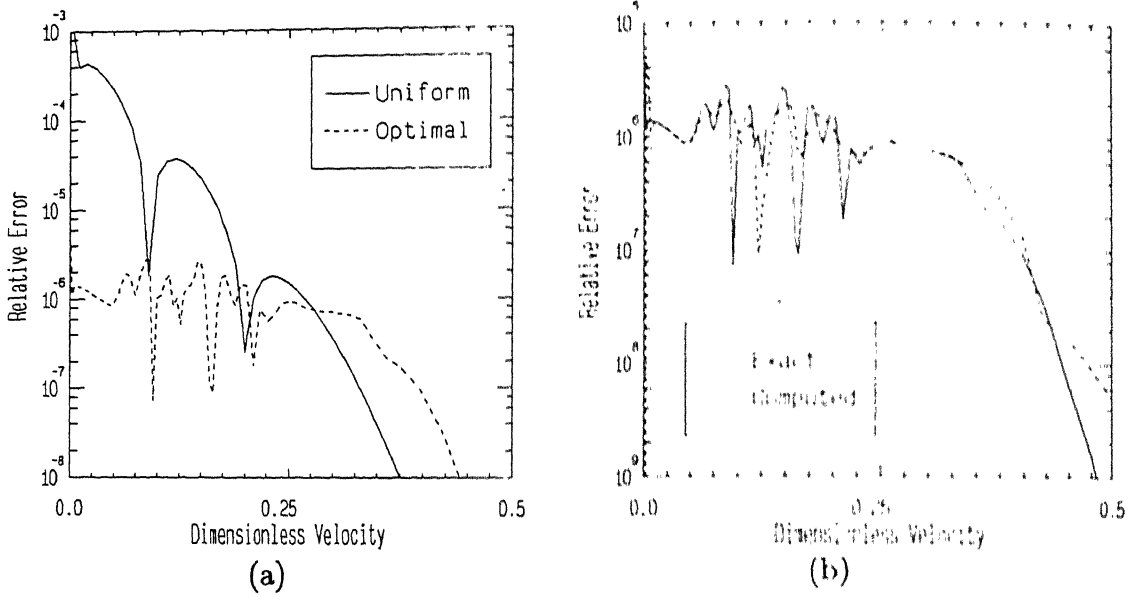


Figure 4.10: Comparison of discretization errors for a Maxwellian distribution with a large velocity cut-off

4.5 Comparison of Errors for Ions and Electrons

As has been mentioned in the earlier chapters, and in the introduction to the present chapter, a characteristic dimensionless velocity scale, x , extending from 0.0 to 1.0, has been used in this work to represent all plasma species. Since the physical cut-off velocities for ions and electrons are very different, the discretization errors for the two species were calculated separately along the lines already discussed in the previous sections. The same number of nodes were used for both the species. The calculations were done using both the three-point central differences as well as a five-point Lagrangian interpolation formula.

The results are shown in Fig. 4.11. It can be seen that if a dimensionless velocity scale is used, the discretization errors are quite comparable for ions and electrons using the same number of nodes. This is true both on the uniform grid as well as on the optimal grid. The reduction in ϵ_{max} by a factor of 7 to 12 in going from a uniform to an optimal grid can be easily observed.

Figure 4.12 shows changing distribution of nodes as a Gaussian distribution

4.5. COMPARISON OF ERRORS FOR IONS AND ELECTRONS

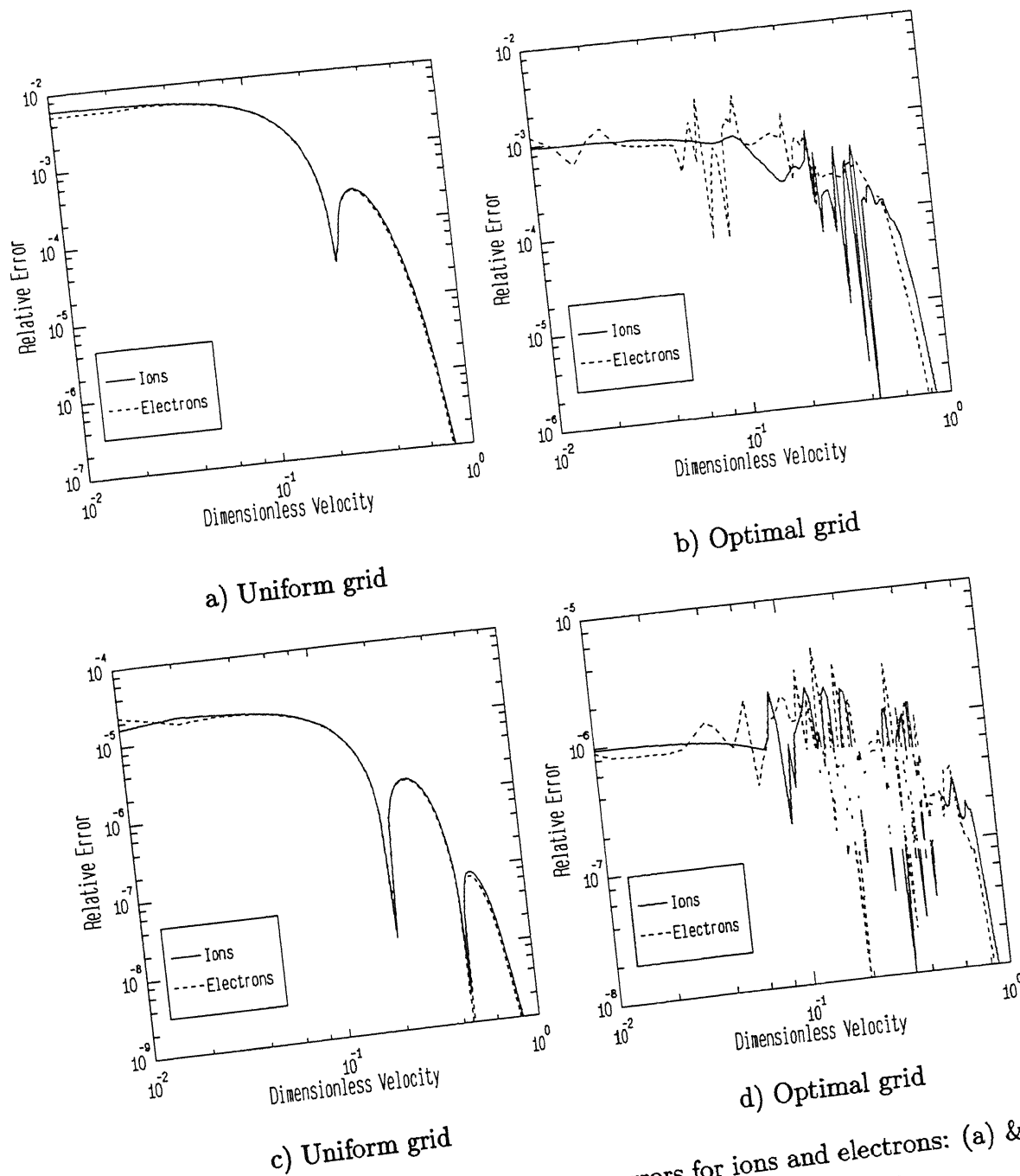


Figure 4.11: Comparison of discretization errors for ions and electrons: (a) & (b) - Standard central difference, (c) & (d) - five-point difference formulae

evolves to a Maxwellian at different times. The number of nodes used is 101, and the grid is adapted after every three time steps. The gaps between the dots along the x-axis represent the grid spacing at the various stages of relaxation (τ is the relaxation time). This figure indicates that the error estimates and the method for grid adaptation presented here can be used for studying the plasma evolution starting from a highly peaked distribution to a near-Maxwellian equilibrium distribution.

4.6 Interpolation and Quadrature Errors

In grid adaptation, as the grid is changed from the old to the new, the distribution functions as well as the coefficients in the Fokker-Planck equations have to be obtained on the new grid. Since this has to be done a large number of times, the projection errors must be kept small. In order to project the values from one grid to other, two points on the old grid closest to the desired point on the new grid are located for the purpose of interpolation. Both linear and cubic (Hermitian and Lagrangian) polynomials have been used for this purpose. The errors involved in one such step are shown in Table 4.1. It can be seen that the maximum error per step is 0.1% if linear interpolation is used. These errors can be reduced to a negligible level if cubic polynomials are used. It should be mentioned here that when different velocity scales are used for different species, such interpolations are required at each step for the computation of the Fokker-Planck coefficients. However, since these coefficients involve the integrals, errors are generally small. These are shown in Table 4.2 for 31 grid points. In most of the calculations, the number of grid points used is larger than 31 and the actual errors are even smaller than shown in the table.

4.7 Adaptive Time Stepping Based on Energy Error

As mentioned in Section 3.5, a numerical solution of the Fokker-Planck equation does not conserve densities and energy exactly. This is due to the discretization

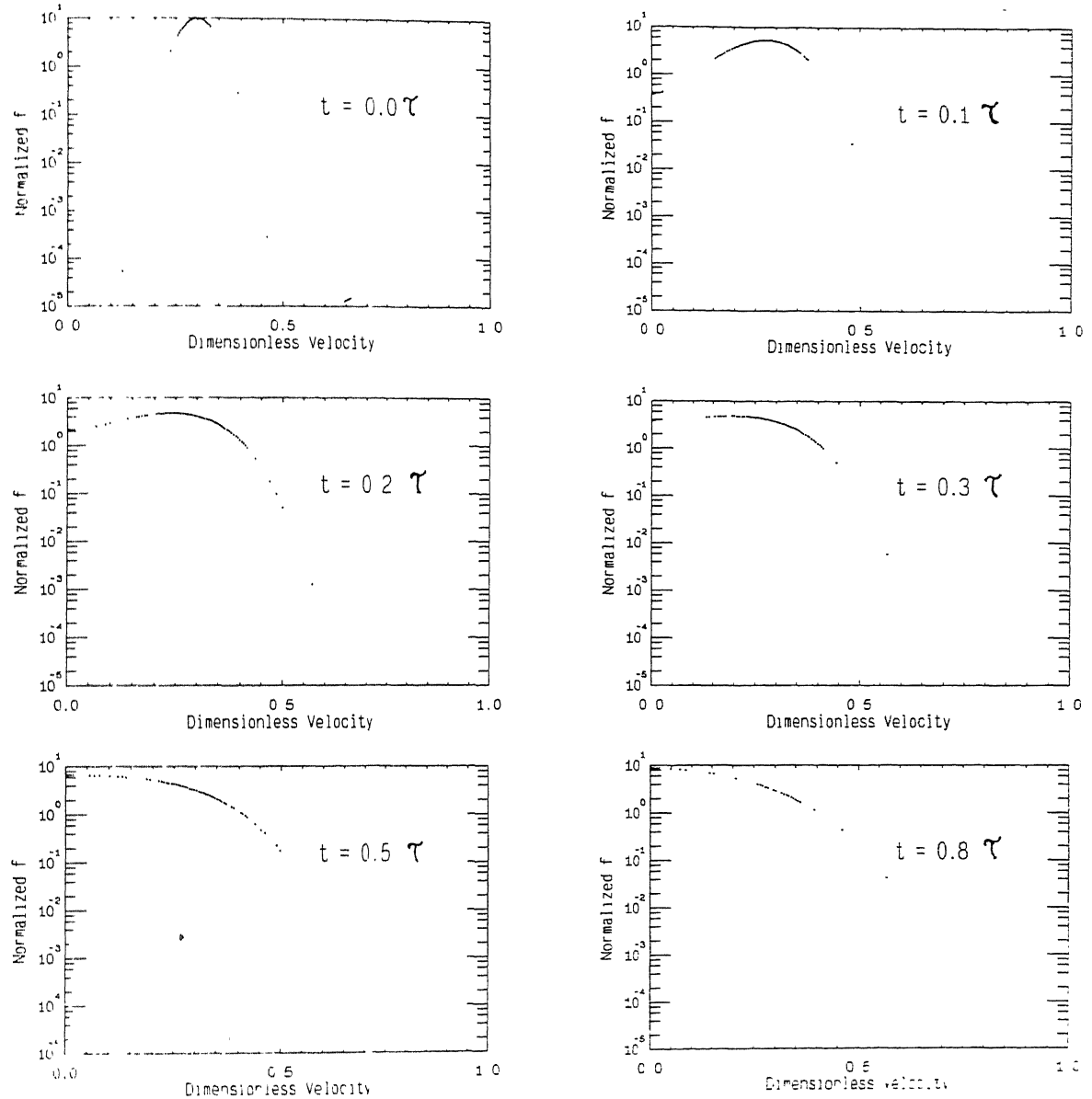


Figure 4.12: Optimal distribution of nodes for the evolution of a Gaussian at different times

errors in the velocity space as well as due to a finite time step used in time marching. The velocity space errors can be reduced by using a larger number of grid points (see Fig. 4.9). In order to control the errors due to time stepping, an adaptive time stepping scheme based on the norm of the energy error in the computed solution has been used. This is done in addition to the renormalization of the densities and energy as explained in Section 3.5. This controls the energy error in each step, avoids the cumulative errors in density and energy, and generally reduces the number of time steps required.

Table 4.3 shows the density and energy errors for a single species at each time step. It can be seen that the density is almost exactly conserved, while the maximum energy error is approximately 0.4%. The corresponding renormalization factors a and b based on eqs. (3.42)-(3.43) are also shown in the table. It can be seen that for a single species 51 grid points are adequate, while for a multispecies plasma simulation involving different types of distribution functions, generally a larger number of grid points are required. The error also depends on the time step $\Delta\tau$. While the energy error per step is small, unless renormalized to the desired value, the cumulative error in, say, 100 steps can become significant. The table also shows that, as expected, $a \approx 1.0$, $b = 0.0$.

The energy error shown in Table 4.3 has been used to control the time step size. Table 4.4 shows the number of time steps required to evolve a Gaussian species for 1 s, starting with $\Delta\tau = 0.1$. If a constant step size is used, 287 steps are required. The number of steps required in the adaptive time stepping depends on the energy error, $\Delta E/E$, tolerated per step. For $\Delta E/E = 0.5$ to 1.0 %, the number of steps required is in the range of 40 to 50, while for $\Delta E/E = 0.05$ to 0.1%, the steps required are between 400 to 500. For other values of $\Delta E/E$, the number of steps required are given in the table. It is seen that if reasonable limits for energy error are specified, the number of steps required and therefore computational time can be significantly reduced.

Table 4.3: Density and energy errors per time step and the renormalization constants a and b

N	$\Delta\tau$	Density error %	Energy error %	a	b
51	0.05	0.00001	0.0028	0.9999	0.00016
	0.10	0.00002	0.0115	0.9996	0.00070
	0.20	0.00006	0.0521	0.9980	0.00320
	0.50	0.00037	0.3829	0.9854	0.02390
101	0.05	0.0	0.0028	0.9999	0.00016
	0.10	0.0	0.0115	0.9996	0.00070
	0.20	0.0	0.0521	0.9980	0.00320
	0.50	0.00033	0.3774	0.9856	0.02390
151	0.05	0.0	0.0028	0.9999	0.00016
	0.10	0.0	0.0115	0.9996	0.00070
	0.20	0.0	0.0517	0.9980	0.00320
	0.50	0.00030	0.3791	0.9855	0.02365

Table 4.4: Number of time steps required for the evolution of a Gaussian species starting with $\Delta\tau = 0.1$ for $t_{max} = 1.0$ s

Number of grid points	Constant $\Delta\tau$	Adaptive $\Delta\tau$			
		$\Delta E/E$			
		0.5-1.0%	0.5-0.25%	0.25-0.125%	0.10-0.05%
31	287	52	103	189	512
51		50	102	183	506
71		46	89	200	470
101		44	93	163	445
151		44	81	161	416
201		41	79	168	403

4.8 Summary

In this chapter the discretization errors in the velocity space have been studied. A strategy to redistribute the nodes iteratively to minimize the errors has been described and implemented. The maximum error can be reduced by an order of magnitude or more if an optimal grid is used instead of a uniform one. The error estimates used in the grid adaptation are checked against the exact errors, where possible. The convergence of ϵ_{max} with the number of grid points has also been presented. The discretization errors for ions and electrons have been compared. Finally, an adaptive time stepping scheme based on the energy error in the computed solution has been presented.

Chapter 5

Numerical Solution of 2-D Fokker-Planck Equations

5.1 Introduction

Numerical simulations using one dimensional analogue of a complex physical situation are naturally useful and make the problem tractable. Such models also reveal the intricacies involved in the process of simulation. Once the 1-D models are developed and implemented successfully, the next logical step in the course of the simulation studies is to extend the numerical models to the next higher dimension. This is essential to obtain more realistic answers to the actual physical situations. From the computational point of view, such answers should be obtained at an acceptable effort. This gives an opportunity to devise new numerical schemes, in addition to improving the existing ones wherever possible, that converge to the correct answers more rapidly.

Numerical simulations of 2-D Fokker-Planck equations are presented in this chapter. The equations are solved by both the Galerkin finite element method and the finite difference method. Five types of quadrilateral elements namely, linear, and the complete and incomplete quadratic and cubic finite elements, are used. Discretization of the spatial part of the Fokker-Planck equation is given in detail. The equations are advanced in time by the one step Θ method. In the case of the finite difference method the equations are integrated by the fully implicit and the

alternating direction implicit methods. As in the previous chapters, a dimensionless velocity scale and a dimensionless time most appropriate for each species is used. Further, the operators used are as obtained in Chapter 2, that is, without singularities at $x = 0$ and $\theta = 0$ and π .

5.2 Finite Element Solution in 2-D

Galerkin finite element formulation of the 2-D Fokker-Planck equations in (v, θ) geometry proceeds on similar steps as in the case of 1-D formulations. Here the computational domain is a semi circle with radius x_{max} (which is equal to 1.0), and the pitch angle θ is between 0 and π . The domain is divided into $N_x N_\theta$ curved quadrilateral elements, where N_x and N_θ are the number of elements in x and θ directions respectively. A typical domain and the mesh partitioning is shown in Fig. 5.1. The elements that have been tried out in this work are also illustrated in Fig. 5.1. The nodes in each element are numbered as shown in the same figure. The incomplete quadratic and cubic elements do not have interior nodes.

It is possible to use either triangular elements completely or a combination of both triangular and rectangular elements to discretize the domain. In this work only quadrilateral elements are used. The curved elements are mapped into quadrilateral elements using isoparametric transformations.

5.2.1 Formulation

The 2-D Fokker-Planck equation to be solved for a single species is of the form

$$\frac{\partial f}{\partial \tau} = \left(\frac{1}{x^2} \frac{\partial G}{\partial x} + \frac{1}{x^2 \sin \theta} \frac{\partial H}{\partial \theta} \right) + Qf + S, \quad (5.1)$$

where

$$G = Af + B \frac{\partial f}{\partial x} + C \frac{\partial f}{\partial \theta}, \quad (5.2)$$

$$H = Df + E \frac{\partial f}{\partial x} + F \frac{\partial f}{\partial \theta}. \quad (5.3)$$

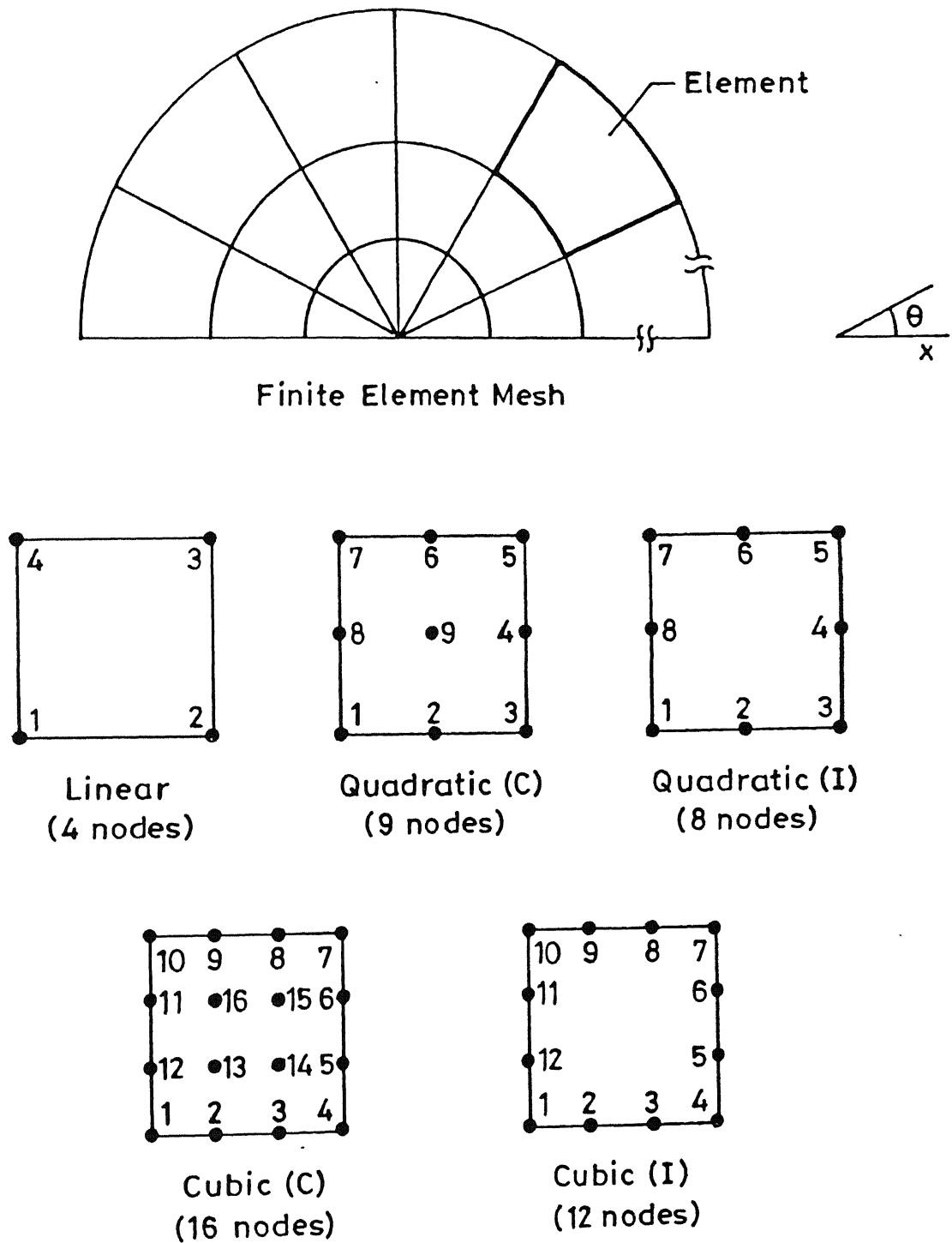


Figure 5.1: Finite element computational domain and various types of quadrilateral finite elements

The symbols have their usual meanings as given in Chapter 2. The boundary conditions are as given in eqs. (2.69)-(2.72). The residue R is

$$R = \frac{\partial \bar{f}}{\partial \tau} - \left(\frac{1}{x^2} \frac{\partial \bar{G}}{\partial x} + \frac{1}{x^2 \sin \theta} \frac{\partial \bar{H}}{\partial \theta} \right) - Q \bar{f} - S, \quad (5.4)$$

and its integral is minimized as

$$\int_0^1 \int_0^\pi W_i R 2\pi x^2 \sin \theta d\theta dx = 0, \quad i=1, \dots, n \quad (5.5)$$

where the factor $2\pi x^2 \sin \theta$ is the 2-D differential area element in radial geometry. The approximate solution \bar{f} at a time τ is written over an element e as

$$\bar{f}^e = \sum_{j=1}^m f_j(\tau) \phi_j(x, \theta), \quad (5.6)$$

where the shape functions ϕ_j are functions of x and θ , and f_j , the nodal values of the distribution function f , are functions of time τ . The number of nodes per element is m . Choosing $W_i = \phi_i$ and substituting eq. (5.4) in eq. (5.5),

$$\int \int^e \left[\frac{\partial \bar{f}}{\partial \tau} - \left(\frac{1}{x^2} \frac{\partial \bar{G}}{\partial x} + \frac{1}{x^2 \sin \theta} \frac{\partial \bar{H}}{\partial \theta} \right) - Q \bar{f} - S \right] \phi_i x^2 \sin \theta d\theta dx = 0, \quad i = 1, \dots, m. \quad (5.7)$$

Integration of the above equation by parts for an element e leads to

$$\begin{aligned} & \int \int^e \phi_i \frac{\partial \bar{f}}{\partial \tau} x^2 \sin \theta d\theta dx + \int \int^e \frac{\partial \phi_i}{\partial x} \bar{G} \sin \theta d\theta dx \\ & + \int \int^e \frac{\partial \phi_i}{\partial \theta} \bar{H} d\theta dx - \int \int^e \phi_i Q \bar{f} x^2 \sin \theta d\theta dx \\ & - \int \int^e \phi_i S x^2 \sin \theta d\theta dx - \int_{\theta_e}^{\theta_{e+1}} \left[\phi_i \bar{G} \sin \theta \right]_{x_e}^{x_{e+1}} d\theta \\ & - \int_{x_e}^{x_{e+1}} \left[\phi_i \bar{H} \right]_{\theta_e}^{\theta_{e+1}} dx = 0, \quad i = 1, \dots, m \end{aligned} \quad (5.8)$$

where x_e, x_{e+1} and θ_e, θ_{e+1} are the global x and θ coordinates of the corner nodes of the element e . Substitution of eq. (5.6) in the above equation leads to

$$\begin{aligned} & \sum_{j=1}^m \left[\left(\int \int^e \phi_i \phi_j x^2 \sin \theta d\theta dx \right) \frac{df_j}{d\tau} + (I_1 + I_2 + I_3 + I_4 + I_5 + I_6 + I_7) f_j \right] \\ &= \sum_{j=1}^m \left[\int \int^e \phi_i S x^2 \sin \theta d\theta dx + \int_{\theta_e}^{\theta_{e+1}} \left[\phi_i \bar{G} \sin \theta \right]_{x_e}^{x_{e+1}} d\theta + \int_{x_e}^{x_{e+1}} \left[\phi_i \bar{H} \right]_{\theta_e}^{\theta_{e+1}} dx \right], \\ & \quad i = 1, \dots, m \end{aligned} \quad (5.9)$$

where

$$I_1 = \int \int^e \frac{\partial \phi_i}{\partial x} B \frac{\partial \phi_j}{\partial x} \sin \theta d\theta dx, \quad (5.10)$$

$$I_2 = \int \int^e \frac{\partial \phi_i}{\partial x} A \phi_j \sin \theta d\theta dx, \quad (5.11)$$

$$I_3 = \int \int^e \frac{\partial \phi_i}{\partial x} C \frac{\partial \phi_j}{\partial \theta} \sin \theta d\theta dx, \quad (5.12)$$

$$I_4 = \int \int^e \frac{\partial \phi_i}{\partial \theta} F \frac{\partial \phi_j}{\partial \theta} d\theta dx, \quad (5.13)$$

$$I_5 = \int \int^e \frac{\partial \phi_i}{\partial \theta} D \phi_j d\theta dx, \quad (5.14)$$

$$I_6 = \int \int^e \frac{\partial \phi_i}{\partial \theta} E \frac{\partial \phi_j}{\partial x} d\theta dx, \quad (5.15)$$

$$I_7 = - \int \int^e \phi_i Q \phi_j x^2 \sin \theta d\theta dx. \quad (5.16)$$

By using the boundary conditions eqs. (2.69)-(2.72) and the values of the coefficients A through F at the boundaries, it can be shown that

$$\int_0^{1.0} \phi_i \bar{H} \Big|_0^\pi dx = 0, \quad (5.17)$$

because $H = 0$ at $\theta = 0$ and π . Similarly

$$\int_0^\pi \phi_i \bar{G} \sin \theta \Big|_0^{1.0} d\theta = 0, \quad (5.18)$$

since G is zero at $x = 0$ and $\bar{f} = 0$ at $x = 1$. The equations (5.9) can then be written as

$$\mathbf{t} \frac{d\mathbf{f}}{d\tau} + \mathbf{u}\mathbf{f}(\tau) = \mathbf{v}(\tau), \quad (5.19)$$

where

$$t_{ij} = \int \int^e \phi_i \phi_j x^2 \sin \theta d\theta dx, \quad (5.20)$$

$$u_{ij} = I_1 + I_2 + I_3 + I_4 + I_5 + I_6 + I_7, \quad (5.21)$$

$$\begin{aligned} v_i = & \int \int^e \phi_i S x^2 \sin \theta d\theta dx + \int_{\theta_e}^{\theta_{e+1}} \left[\phi_i \bar{G} \sin \theta \right]_{x_e}^{x_{e+1}} d\theta \\ & + \int_{x_e}^{x_{e+1}} \left[\phi_i \bar{H} \right]_{\theta_e}^{\theta_{e+1}} dx. \end{aligned} \quad (5.22)$$

Element matrices are generated for all the elements in the mesh. These matrices are assembled to form the global finite element discretized equations (Dhatt and Touzot, 1985) given by

$$\mathbf{T} \frac{d\mathbf{f}}{d\tau} + \mathbf{U}\mathbf{f} = \mathbf{V}. \quad (5.23)$$

Equation (5.23) represents a system of coupled ordinary differential equations. This system is solved using the one step Θ -method (time marching scheme).

5.2.2 Evaluation of Element Matrices and Coefficients

Each of the elements shown in Fig. 5.1 is represented by isoparametric rectangular elements with local variables (ξ, η) in the x and θ directions. The transformation of global coordinates (x, θ) to local coordinates (ξ, η) can be written in terms of the

shape functions $\phi_i(\xi, \eta)$ as

$$x = \sum_{i=1}^m x_i \phi_i(\xi, \eta), \quad (5.24)$$

$$\theta = \sum_{i=1}^m \theta_i \phi_i(\xi, \eta), \quad (5.25)$$

where x_i and θ_i are global coordinates. With the help of above transformations, the integrals of element matrices in eqs. (5.20)-(5.22) can be evaluated using Gauss quadrature. The differential element area $dx d\theta$ is written as

$$dx d\theta = |\mathbf{J}| d\xi d\eta, \quad (5.26)$$

where $|\mathbf{J}|$ is the determinant of the Jacobian matrix

$$\mathbf{J} = \begin{bmatrix} \frac{\partial x}{\partial \xi} & \frac{\partial \theta}{\partial \xi} \\ \frac{\partial x}{\partial \eta} & \frac{\partial \theta}{\partial \eta} \end{bmatrix}. \quad (5.27)$$

The elements of \mathbf{J} can be obtained by differentiating eqs.(5.24) and (5.25). For rectangular elements $|\mathbf{J}|$ is the area of the element, which is known. The derivatives $\partial\phi/\partial x$ and $\partial\phi/\partial\theta$ are calculated using the following transformation

$$\begin{bmatrix} \frac{\partial \phi}{\partial x} \\ \frac{\partial \phi}{\partial \theta} \end{bmatrix} = \frac{1}{|\mathbf{J}|} \begin{bmatrix} \frac{\partial \theta}{\partial \xi} & -\frac{\partial \theta}{\partial \eta} \\ -\frac{\partial x}{\partial \xi} & \frac{\partial x}{\partial \eta} \end{bmatrix} \begin{bmatrix} \frac{\partial \phi}{\partial \xi} \\ \frac{\partial \phi}{\partial \eta} \end{bmatrix}. \quad (5.28)$$

Using equations (5.24) and (5.28), the integrals in eqs.(5.20)-(5.22) can be rewritten in terms of the variables (ξ, η) as

$$t_{ij} = \int_{-1}^{+1} \int_{-1}^{+1} \phi_i \phi_j |\mathbf{J}| x^2 \sin \theta d\xi d\eta, \quad (5.29)$$

$$u_{ij} = I_1 + I_2 + I_3 + I_4 + I_5 + I_6 + I_7, \quad (5.30)$$

$$\begin{aligned}
v_i &= \int_{-1}^{+1} \int_{-1}^{+1} \phi_i S |\mathbf{J}| x^2 \sin \theta d\xi d\eta + \frac{(\theta_{e+1} - \theta_e)}{2} \int_{-1}^{+1} [\phi_i \bar{G} \sin \theta]_{x_e}^{x_{e+1}} d\eta \\
&\quad + \frac{(x_{e+1} - x_e)}{2} \int_{-1}^{+1} [\phi_i \bar{H}]_{\theta_e}^{\theta_{e+1}} d\xi,
\end{aligned} \tag{5.31}$$

where

$$I_1 = \int_{-1}^{+1} \int_{-1}^{+1} \frac{\partial \phi_i}{\partial x}(\xi, \eta) B \frac{\partial \phi_j}{\partial x}(\xi, \eta) |\mathbf{J}| \sin \theta d\xi d\eta, \tag{5.32}$$

$$I_2 = \int_{-1}^{+1} \int_{-1}^{+1} \frac{\partial \phi_i}{\partial x}(\xi, \eta) A \phi_j(\xi, \eta) |\mathbf{J}| \sin \theta d\xi d\eta, \tag{5.33}$$

$$I_3 = \int_{-1}^{+1} \int_{-1}^{+1} \frac{\partial \phi_i}{\partial x}(\xi, \eta) C \frac{\partial \phi_j}{\partial \theta}(\xi, \eta) |\mathbf{J}| \sin \theta d\xi d\eta, \tag{5.34}$$

$$I_4 = \int_{-1}^{+1} \int_{-1}^{+1} \frac{\partial \phi_i}{\partial \theta}(\xi, \eta) F \frac{\partial \phi_j}{\partial \theta}(\xi, \eta) |\mathbf{J}| d\xi d\theta, \tag{5.35}$$

$$I_5 = \int_{-1}^{+1} \int_{-1}^{+1} \frac{\partial \phi_i}{\partial \theta}(\xi, \eta) D \phi_j(\xi, \eta) |\mathbf{J}| d\xi d\eta, \tag{5.36}$$

$$I_6 = \int_{-1}^{+1} \int_{-1}^{+1} \frac{\partial \phi_i}{\partial \theta}(\xi, \eta) E \frac{\partial \phi_j}{\partial x}(\xi, \eta) |\mathbf{J}| d\xi d\eta, \tag{5.37}$$

$$I_7 = - \int_{-1}^{+1} \int_{-1}^{+1} \phi_i(\xi, \eta) Q \phi_j(\xi, \eta) |\mathbf{J}| x^2 \sin \theta d\xi d\eta. \tag{5.38}$$

The 2-D integrals in the above equations are evaluated by Gauss quadrature. A general 2-D integral is evaluated as

$$\int_{-1}^{+1} \int_{-1}^{+1} z(\xi, \eta) d\xi d\eta = \sum_{i=1}^{N_g} \sum_{j=1}^{N_g} w_i w_j z(\xi_i, \eta_j), \tag{5.39}$$

where (ξ_i, η_j) are Gauss points and w_i, w_j are the corresponding weights. It is not necessary that same number of Gauss points N_g should be used for both directions.

An easy way to generate two dimensional basis functions is to form the product of two one dimensional basis functions. This is true for complete elements. However for incomplete elements without interior nodes, these functions differ slightly. The shape functions $\phi_i(\xi, \eta)$ for five types of elements considered in this work, viz., linear,

complete and incomplete quadratic and cubic elements are given in Appendix B.

The coefficients A through F appearing in the element matrices are approximated as described in Section 3.2.2. Their nodal values are interpolated for different values of (ξ_i, η_j) . The other coefficients Q and S are also handled in the same manner.

The elements at $x = 0$ require special mention. Here, collapsed rectangular elements are used for mapping. In this case, one side of the rectangular elements is collapsed onto a point by setting the global coordinates to be the same for all the nodes on that side. This approach is followed in order to use the same type of elements in the entire domain.

5.3 Accuracy and Numerical Results

5.3.1 Error Indicators and Relaxation Norms

The convergence and accuracy of the finite element solutions can be improved by using higher order elements, increasing number of elements and/or by decreasing the time step, etc. It is always desirable to obtain accurate numerical result at a minimum computational effort. The quality of the numerical solution of the 2-D Fokker-Planck equation is measured using the error norms as defined in Section 3.4.1. For 2-D these error indicators in percent can be written as

$$e_{\infty} = \frac{|\Delta f_{i,j}|_{max}}{f_{max}} \times 100, \quad (5.40)$$

$$e_1 = \frac{\int \int |\Delta f| x^2 \sin \theta d\theta dx}{\int \int f x^2 \sin \theta d\theta dx} \times 100, \quad (5.41)$$

$$e_2 = \left[\frac{\int \int |\Delta f|^2 x^2 \sin \theta d\theta dx}{\int \int f^2 x^2 \sin \theta d\theta dx} \right]^{1/2} \times 100, \quad (5.42)$$

$$e_{rms} = \left[\frac{1}{N_x N_{\theta}} \sum_{ij} |\Delta f_{ij}|^2 \right]^{1/2} \times 100. \quad (5.43)$$

with $\Delta f_{ij} = f_{ij}^{exact} - \bar{f}_{ij}$. f_{ij}^{exact} and \bar{f}_{ij} are the exact and computed solutions respectively, at the location (i, j) in the numerical grid. N_x and N_θ are the total number of nodes in the x and θ directions. As in 1-D, the norms defined above are also used to measure the degree of relaxation of an arbitrary distribution at different times. In this case f_{ij}^{exact} represents the Maxwellian to which the initial distribution function is expected to evolve. When used for this purpose, the norms are denoted by L_n

5.3.2 Performance of the Quadrilateral Finite Elements

As in Chapter 3, the performance of the various types of quadrilateral finite elements can be evaluated based on the errors introduced by numerical evolution and by studying the relaxation of a Gaussian distribution function. In the case of 2-D problems, as the order of the element increases, say from linear to quadratic etc, the CPU time also increases significantly. A major portion of the time is usually spent in solving the banded algebraic system of equations. Nevertheless higher order elements produce more accurate results. This fact has already been established with 1-D finite elements.

The size of the banded system also depends upon the way the nodes in the finite element mesh are numbered globally, either row wise or column wise. In the present problem the semicircular domain is discretized into a finite number of elements. Starting from $x = 0$, the nodes in the θ direction are numbered first in the ascending order from $\theta = 0$ to π . This has some advantage as the number of grid points in the θ direction is usually less than that in the x direction. This procedure reduces the bandwidth of the algebraic system. The bandwidth is determined from

$$NBW = \max_{\substack{1 \leq IE \leq N_x N_\theta \\ 1 \leq i, j \leq N_e}} [|NODE(IE, i) - NODE(IE, j)| + 1], \quad (5.44)$$

where the matrix $NODE(.,.)$ (known as the connectivity matrix) contains the information about the global node numbers in the IE^{th} element, N_e is the number of nodes in each element and i, j are the locations of the nodes. Total number of

elements ($N_x N_\theta$) is the product of the number of elements in the x and θ directions. It can be deduced that the bandwidth is minimum for the linear elements with 4 nodes and maximum for the cubic elements with 16 nodes. Further the bandwidths corresponding to the incomplete elements are less than the corresponding complete elements.

Spatial Convergence

The relaxation of an arbitrary distribution of the form

$$f(x, \theta) = \alpha \exp(-b(x - a)^2 - c(\sin \theta - d)^2) \quad (5.45)$$

has been studied to estimate the accuracy of the two dimensional quadrilateral finite elements. The constant c is varied from 2 to 20 with $d = 0$. In all the cases it was found that the initial distributions eventually reach to the steady state Maxwellian. Numerical results for one such case ($c = 20$) is shown in Fig. 5.2. The relaxation measures L_∞, L_1, L_2 , and L_{rms} are shown at 6τ (τ - relaxation time) for the Crank-Nicolson scheme. The number of nodes used in the θ direction is 31 and it is kept constant for all the cases.

The figure indicates that the linear elements with less number of nodes behave differently compared to the quadratic and cubic elements. However as the number of nodes is increased, the measures show a trend to move towards those obtained using the higher order elements. This behavior coincides with a similar observation made earlier in Section 3.4 with 1-D elements. The measures at 6τ are different corresponding to the different types of elements. Such differences will become much less if the number of elements in both x and θ directions are increased further. It is clear that the relaxation norms obtained by the use of incomplete quadratic and cubic elements are not much different from those of the corresponding complete elements. This is a useful observation as the bandwidth associated with the incomplete elements is less, as observed above. Similar results were observed with the fully implicit scheme too. It should be observed from the figures, that while using higher order elements, there is little advantage in going from 31 to 91 nodes. The degree of relaxation shown is more or less the same in all the four norms.

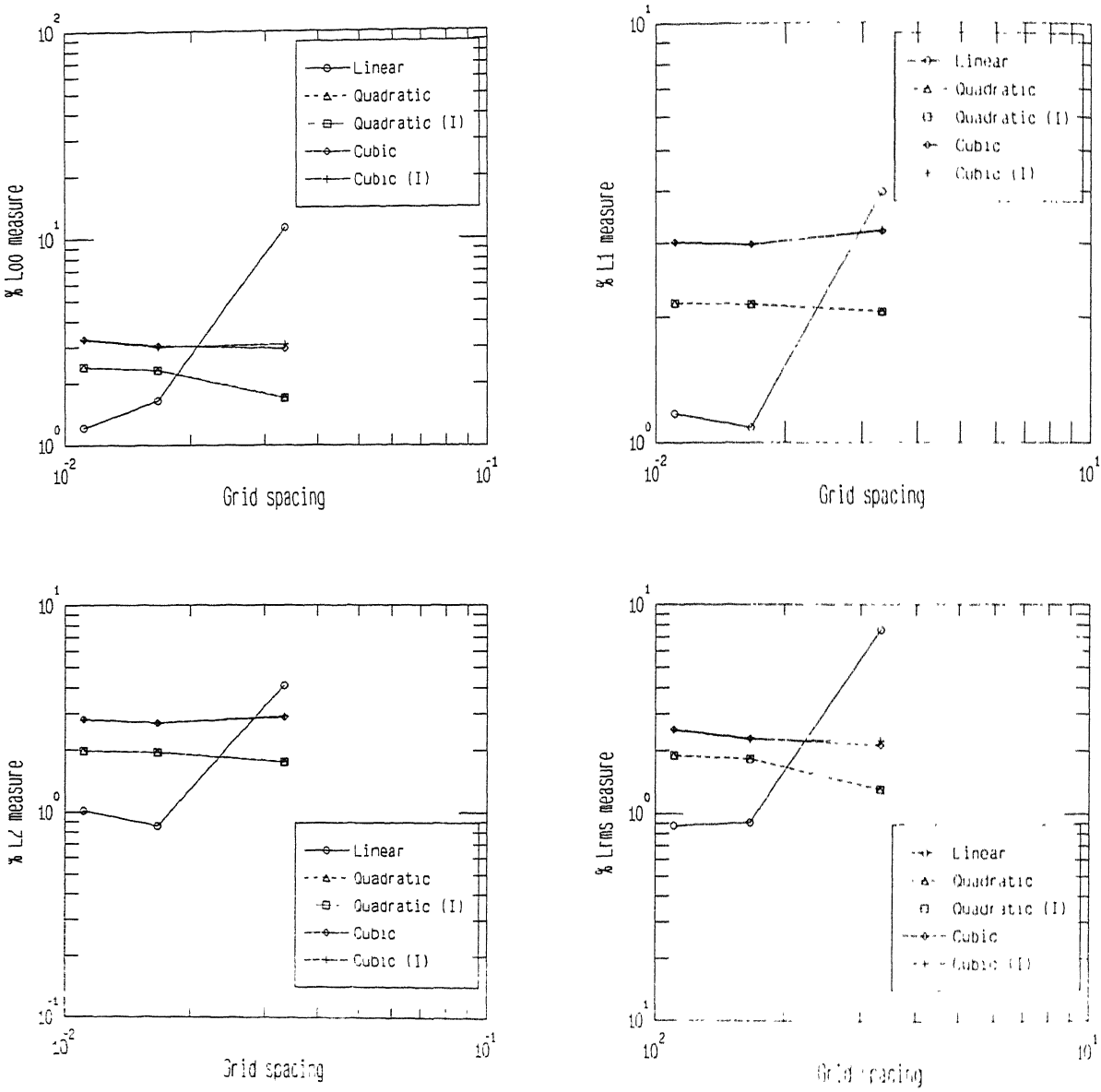


Figure 5.2: Spatial convergence of various types of quadrilateral finite elements

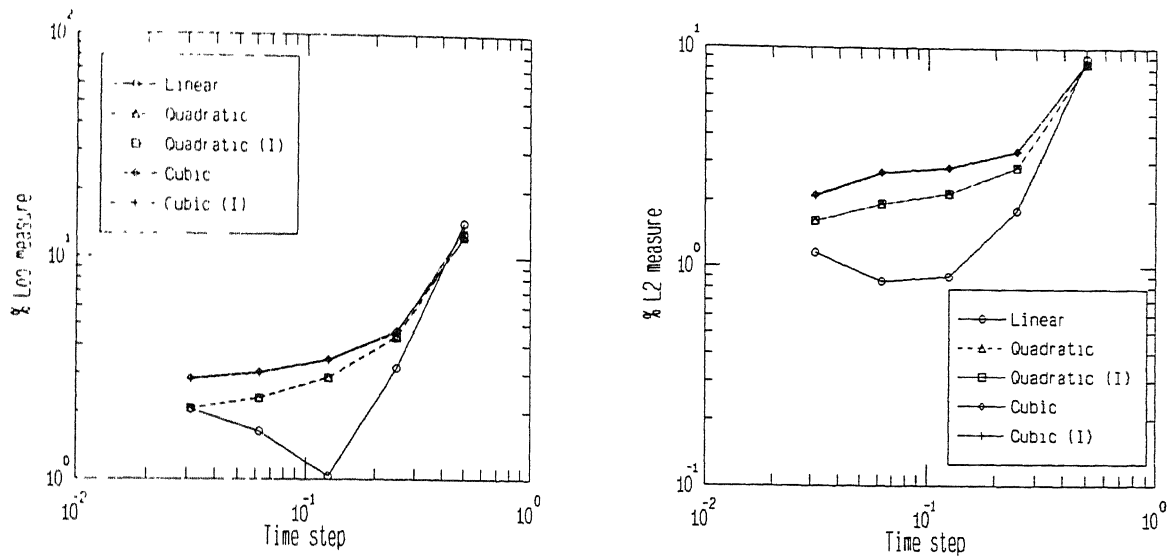


Figure 5.3: Temporal convergence of the quadrilateral finite elements

Temporal Convergence

Temporal convergence of the five types of quadrilateral finite elements is also studied by observing the relaxation of an arbitrary initial distribution. The results are illustrated in Fig. 5.3. The relaxation measures have been obtained with $d = 0$ in eq. (5.45) for a mesh of 61×31 (x, θ) nodes. Time step $\Delta\tau$ is varied from $1/2$ to $1/32 \tau$. The measures L_∞ and L_2 , shown in the same figure for the Crank-Nicolson scheme, indicate that when the time step is large ($\Delta\tau = 1/2$), all the elements slow down the relaxation. As the step size is made small, the linear elements show slightly different behavior between $\Delta\tau = 1/4$ and $1/16$. Eventually, for small $\Delta\tau$, they yield the same degree of relaxation as obtained using higher order elements.

Interestingly the incomplete elements have shown almost the same result as that obtained by the use of complete elements. When incomplete elements are used, the values at the interior nodes are obtained by interpolation. However, these values are needed only for the calculation of Fokker-Planck coefficients. Since the latter involve only the integrals, the error is relatively small.

Further the computational time is also an important aspect in judging the performance of the various elements. The relative CPU times required for 100 time

Table 5.1: CPU times for the quadrilateral finite elements with respect to the linear elements

No.	Element type	Time
1	Linear	1.00
2	Quadratic	1.99
3	Quadratic (I)	1.09
4	Cubic	3.92
5	Cubic (I)	1.02

steps on a mesh size of 61×31 nodes are given in Table 5.1. It is natural that the complete cubic elements, whose bandwidth (of the algebraic system) is maximum require the maximum time. Next in the row in terms of the computation time are the complete quadratic elements. However the incomplete elements take approximately the same time as that of the linear elements. This is true of both the quadratic and the cubic elements. In other words, roughly for the same amount of computational effort as required by the linear elements, it is possible to get more accurate results using the incomplete higher order elements.

Numerical Oscillations

The problem of the distribution function f becoming negative is investigated with a simple example. The number of nodes at which f is negative during the evolution of a highly peaked anisotropic distribution at each time step is shown in Fig. 5.4. The results are shown in fractions which are obtained as the ratio of the number of negative values to the total number of nodes in the mesh. The fractions show clearly that when the mesh is made finer from 61×31 (Fig. 5.4a) to 91×31 (Fig. 5.4b), the oscillations die out faster (in about 3τ in Fig. 5.4b as compared to 5τ in Fig. 5.4a). Further fine meshes also reduce the fractional negative values (Chang and Cooper, 1970; McCoy, Mirin and Killeen, 1981; Harrison, 1988). The incomplete elements, produce somewhat more negative values in the solution which take a little longer

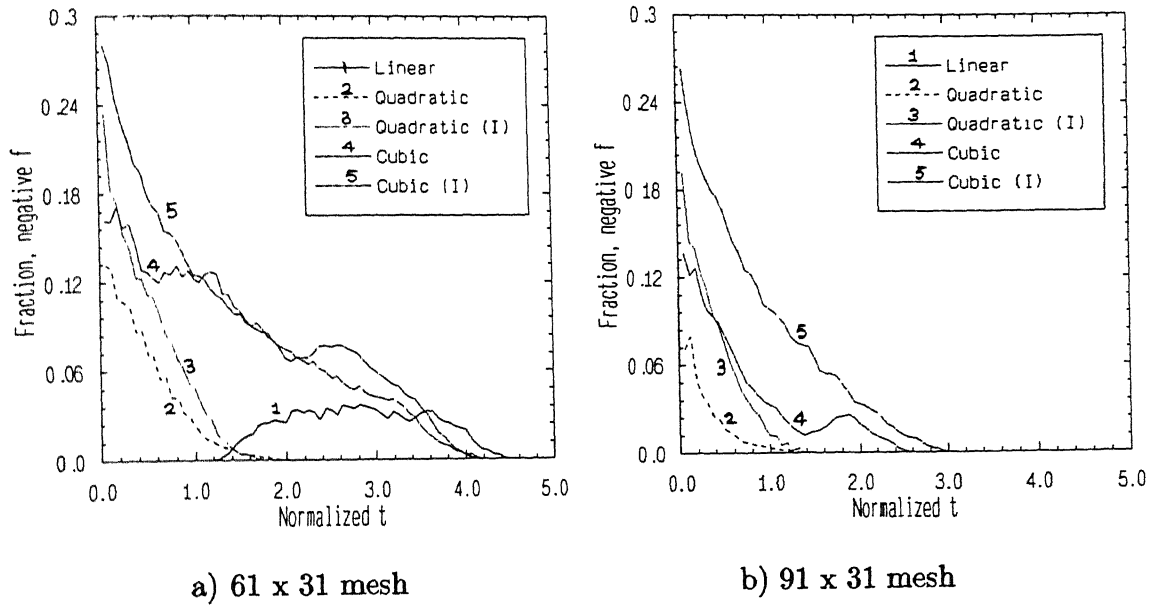


Figure 5.4: The distribution of fractional negative values of f in a 2-D evolution

to die out. However it can be visualized that once the spectrum becomes more or less smooth after a period of time all the elements show a consistent behavior, with incomplete elements yielding almost the same accuracy as the complete elements at a lesser cost.

In 1-D calculations in Chapter 3, fraction of negative f in a multispecies case in 250 steps (0.5 s) was presented in Table 3.4. The stepwise distribution is shown in Fig. 5.5 for $N = 61$ and 91 nodes. It is observed that coarse grids bring in fractionally more negative values in the solution. It is seen that the quadratic elements are better than the linear and cubic elements in terms of avoiding the spurious oscillations. These oscillations die out after a certain time.

5.4 Finite Difference Solutions

In the finite difference method the computational domain is represented by I and J grid points in the x and θ directions respectively. The derivatives are approximated at each grid point accurate to second order in both directions. The resulting alge-

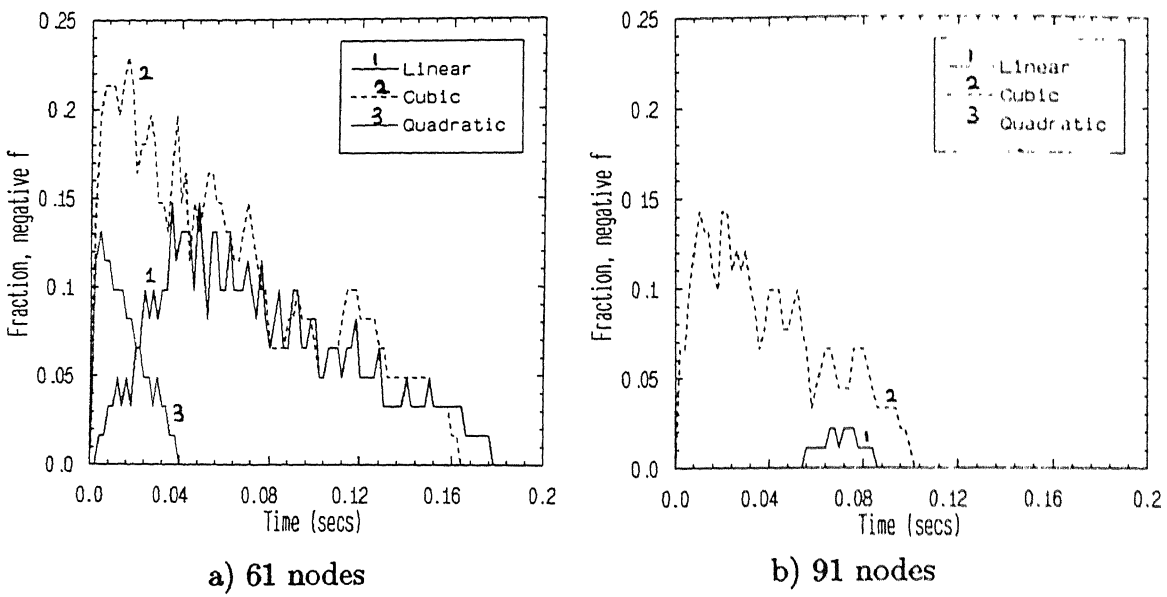


Figure 5.5: The distribution of fractional negative values of f in a 1-D multispecies problem

oratic equations are solved for the distribution functions at these grid points. The size of the system to be solved at every time step is dictated by the choice of the time stepping scheme.

The 2-D Fokker-Planck equation considered for the finite difference method of solution is as given in eq. (2.37). As elsewhere in this work, the dimensionless velocity and time scales for each species are based on the corresponding characteristic values. The x and θ derivatives are discretized at a node (i, j) in an unequally paced grid using the standard central finite differences (McCoy, Mirin and Killeen, 1981). They are

$$\left. \frac{\partial(Af)}{\partial x} \right|_{i,j} \approx (A_{i+1,j} f_{i+1,j} - A_{i-1,j} f_{i-1,j}) / 2\Delta x_i, \quad (5.46)$$

$$\begin{aligned} \left. \frac{\partial}{\partial x} \left(B \frac{\partial f}{\partial x} \right) \right|_{i,j} \approx & \frac{1}{\Delta x_i} \left[B_{i+1/2,j} \left(\frac{f_{i+1,j} - f_{i,j}}{\Delta x_{i+1/2}} \right) \right. \\ & \left. - B_{i-1/2,j} \left(\frac{f_{i,j} - f_{i-1,j}}{\Delta x_{i-1/2}} \right) \right], \end{aligned} \quad (5.47)$$

$$\begin{aligned} \left. \frac{\partial}{\partial x} \left(C \frac{\partial f}{\partial \theta} \right) \right|_{i,j} &\approx \frac{1}{2\Delta x_i} \left[C_{i+1,j} \left(\frac{f_{i+1,j+1} - f_{i+1,j-1}}{2\Delta \theta_j} \right) \right. \\ &\quad \left. - C_{i-1,j} \left(\frac{f_{i-1,j+1} - f_{i-1,j-1}}{2\Delta \theta_j} \right) \right], \end{aligned} \quad (5.48)$$

$$\left. \frac{\partial(Df)}{\partial \theta} \right|_{i,j} \approx (D_{i,j+1}f_{i,j+1} - D_{i,j-1}f_{i,j-1})/2\Delta \theta_j, \quad (5.49)$$

$$\begin{aligned} \left. \frac{\partial}{\partial \theta} \left(E \frac{\partial f}{\partial x} \right) \right|_{i,j} &\approx \frac{1}{2\Delta \theta_j} \left[E_{i,j+1} \left(\frac{f_{i+1,j+1} - f_{i-1,j+1}}{2\Delta x_i} \right) \right. \\ &\quad \left. - E_{i,j-1} \left(\frac{f_{i+1,j-1} - f_{i-1,j-1}}{2\Delta x_i} \right) \right], \end{aligned} \quad (5.50)$$

$$\begin{aligned} \left. \frac{\partial}{\partial \theta} \left(F \frac{\partial f}{\partial \theta} \right) \right|_{i,j} &\approx \frac{1}{\Delta \theta_j} \left[F_{i,j+1/2} \left(\frac{f_{i,j+1} - f_{i,j}}{\Delta \theta_{j+1/2}} \right) \right. \\ &\quad \left. - F_{i,j-1/2} \left(\frac{f_{i,j} - f_{i,j-1}}{\Delta \theta_{j-1/2}} \right) \right], \end{aligned} \quad (5.51)$$

where

$$B_{i\pm 1/2,j} = \frac{1}{2}(B_{i,j} + B_{i\pm 1,j}), \quad (5.52)$$

$$\Delta \theta_j = \frac{1}{2}(\theta_{j+1} - \theta_{j-1}), \quad (5.53)$$

$$\Delta \theta_{j\pm 1/2} = \pm (\theta_{j\pm 1} - \theta_j), \quad (5.54)$$

$$F_{i,j\pm 1/2} = \frac{1}{2}(F_{i,j} + F_{i,j\pm 1}), \quad (5.55)$$

and the Δx_i and $\Delta x_{i+1/2}$ are defined in eqs. (3.48)-(3.49).

5.4.1 Θ -method of Solution in 2-D

The 2-D Fokker-Planck equations can be integrated in time by different schemes including the one step Θ -method. As pointed out earlier the time stepping schemes

that have already been successfully implemented in the existing codes are, fully implicit method, alternating direction implicit method, and implicit operator splitting (McCoy, Mirin and Killeen, 1981; McKenzie, O'Brien and Cox, 1991). In the present work, two schemes have been tried, namely the Θ -method and the alternating direction implicit method. As in 1-D, the approximation at the boundaries can be purely numerical (similar to eq. (3.61)) or based on the analytical limits at $x = 0$, and $\theta = 0$ and π derived in Chapter 2 (eqs. (2.121)-(2.125), and (2.133)).

The Θ -Method

The Θ -method has already been introduced in Chapter 3. When this method is used, the 2-D equations are solved at all the grid points at the same time. The discretization procedure which is second order accurate in space is a nine-point difference algorithm. The resulting algebraic equation at each node (i, j) can be written as

$$\begin{aligned} \alpha_i^{j-1} f_{i+1,j-1}^{n+1} + \alpha_i^j f_{i+1,j}^{n+1} + \alpha_i^{j+1} f_{i+1,j+1}^{n+1} \\ \beta_i^{j-1} f_{i,j-1}^{n+1} + \beta_i^j f_{i,j}^{n+1} + \beta_i^{j+1} f_{i,j+1}^{n+1} \\ \gamma_i^{j-1} f_{i-1,j-1}^{n+1} + \gamma_i^j f_{i-1,j}^{n+1} + \gamma_i^{j+1} f_{i-1,j+1}^{n+1} = \delta_i^j. \end{aligned} \quad (5.56)$$

The nine banded structure of the above equation is the consequence of nine-point difference algorithm. The coefficients α, β, γ and δ are

$$\begin{aligned} \alpha_i^{j-1} &= -\Theta a_i^{j-1}; \quad \beta_i^{j-1} = -\Theta b_i^{j-1}; \quad \gamma_i^{j-1} = -\Theta c_i^{j-1}, \\ \alpha_i^j &= -\Theta a_i^j; \quad \beta_i^j = -\Theta b_i^j + \frac{1}{\Delta r}; \quad \gamma_i^j = -\Theta c_i^j, \\ \alpha_i^{j+1} &= -\Theta a_i^{j+1}; \quad \beta_i^{j+1} = -\Theta b_i^{j+1}; \quad \gamma_i^{j+1} = -\Theta c_i^{j+1}, \end{aligned} \quad (5.57)$$

and

$$\delta_i^j = (1 - \Theta)(a_i^{j-1} f_{i+1,j-1}^n + a_i^j f_{i+1,j}^n + a_i^{j+1} f_{i+1,j+1}^n$$

$$\begin{aligned}
& b_i^{j-1} f_{i,j-1}^n + b_i^j f_{i,j}^n + a_i^{j+1} f_{i,j+1}^n \\
& c_i^{j-1} f_{i-1,j-1}^n + c_i^j f_{i-1,j}^n + c_i^{j+1} f_{i-1,j+1}^n + \frac{1}{\Delta\tau} f_{i,j}^n,
\end{aligned} \tag{5.58}$$

with

$$a_i^{j-1} = -\frac{1}{x_j^2 4\Delta x_i \Delta\theta_j} \left(C_{i+1,j}^n + \frac{E_{i,j-1}^n}{\sin\theta_j} \right), \tag{5.59}$$

$$a_i^j = \frac{1}{x_i^2 \Delta x_i} \left(\frac{A_{i+1,j}^n}{2} + \frac{B_{i+1/2,j}^n}{\Delta x_{i+1/2}} \right), \tag{5.60}$$

$$a_i^{j+1} = +\frac{1}{x_j^2 4\Delta x_i \Delta\theta_j} \left(C_{i+1,j}^n + \frac{E_{i,j+1}^n}{\sin\theta_j} \right), \tag{5.61}$$

$$b_i^{j-1} = +\frac{1}{x_j^2 \Delta\theta_j \sin\theta} \left(-\frac{D_{i,j-1}^n}{2} + \frac{F_{i,j-1/2}^n}{\Delta\theta_{j-1/2}} \right), \tag{5.62}$$

$$\begin{aligned}
b_i^j = & -\frac{1}{x_i^2} \left[\frac{1}{\Delta x_i} \left(\frac{B_{i+1/2,j}^n}{\Delta x_{i+1/2}} + \frac{B_{i-1/2,j}^n}{\Delta x_{i-1/2}} \right) \right. \\
& \left. + \frac{1}{\Delta\theta_j} \left(\frac{F_{i,j+1/2}^n}{\Delta\theta_{j+1/2}} + \frac{F_{i,j-1/2}^n}{\Delta\theta_{j-1/2}} \right) \right],
\end{aligned} \tag{5.63}$$

$$b_i^{j+1} = +\frac{1}{x_j^2 \Delta\theta_j \sin\theta} \left(\frac{D_{i,j+1}^n}{2} + \frac{F_{i,j+1/2}^n}{\Delta\theta_{j+1/2}} \right), \tag{5.64}$$

$$c_i^{j-1} = \frac{1}{x_j^2 4\Delta x_i \Delta\theta_j} \left(C_{i-1,j}^n + \frac{E_{i,j-1}^n}{\sin\theta_j} \right), \tag{5.65}$$

$$c_i^j = \frac{1}{x_i^2 \Delta x_i} \left(-\frac{A_{i-1,j}^n}{2} + \frac{B_{i-1/2,j}^n}{\Delta x_{i-1/2}} \right), \tag{5.66}$$

$$c_i^{j+1} = -\frac{1}{x_j^2 4\Delta x_i \Delta\theta_j} \left(C_{i-1,j}^n + \frac{E_{i,j+1}^n}{\sin\theta_j} \right). \tag{5.67}$$

The final system is of the form

$$\mathbf{A}\mathbf{F}^{n+1} = \mathbf{B} \tag{5.68}$$

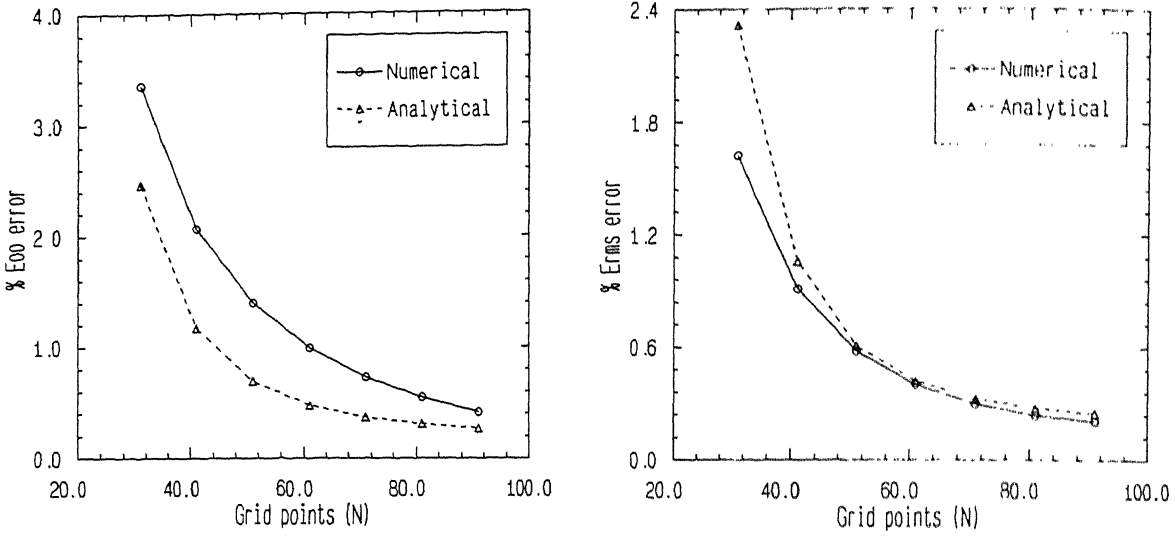


Figure 5.6: Comparison of numerical errors using different boundary approximations

where f^{n+1} is a vector with I times J components corresponding to grid points arranged row wise or column wise and A is a nine banded matrix.

Numerical Results

Figure 5.6 presents the errors introduced due to numerical evolution using the two different types of approximation at the boundaries, $x = 0$ and $\theta = 0$ and π . The results are presented for different number of grid points. The curves show that the approximation based on the analytical limits of the operator at the boundaries improves the e_{∞} error. The e_{rms} errors are almost the same in the two cases. This can be expected as the approximation at the boundaries affects only a few equations in the system (5.68). Convergence with increasing number of grid points is clearly brought out in these figures.

The relaxation of a Gaussian input distribution function in the form of eq. (5.45) has also been studied using both types of approximations at the boundary. The order of the Legendre polynomial used is $l = 4$. The relaxation measures L_{∞} and L_2 are given in Table 5.2 for a fixed $N_{\theta} = 31$. The measures show that both numerical

Table 5.2: Relaxation norms for a Gaussian input

N	<u>Numerical</u>		<u>Analytical</u>	
	L_∞	L_{rms}	L_∞	L_{rms}
31	1.514	1.361	3.288	3.131
41	1.714	1.436	2.413	2.273
51	1.854	1.623	2.162	2.009
61	1.961	1.755	2.081	1.918
71	2.045	1.845	2.059	1.886
81	2.110	1.906	2.062	1.876
91	2.162	1.949	2.074	1.876

and analytical approximations yield more or less the same degree of relaxation with $N_x \geq 71$. However when N_x is below 71, the evolution based on the purely numerical treatment at the boundaries is faster. Thus for coarser grid there is some merit in applying the analytical method at the boundaries. In all these cases the initial distribution approaches the steady state Maxwellian.

5.4.2 Alternating Direction Implicit Method

In this method, the equation is advanced in time in two steps. The equation is treated as explicit in θ and implicit in x direction in the first half time step, from n to $n + 1/2$. In the second half time step, that is from $n + 1/2$ to $n + 1$, the equation is implicit in θ direction and explicit in x . This method is stable and second order accurate in time. The advantage of this method is that it solves $I + J$ tridiagonal systems to advance one step in time. Therefore it is much faster than the Θ -method. The tridiagonal system of equations can be solved easily. Consequently, large matrices need not be stored or inverted, as in the case of Θ -method. The

equation for the first and second half time steps can be written as

$$\begin{aligned} \frac{f_{i,j}^{n+1/2} - f_{i,j}^n}{\Delta\tau/2} &= \frac{1}{x_i^2} \left[\frac{\partial}{\partial x} \left(A^n f^{n+1/2} + B^n \frac{\partial f^{n+1/2}}{\partial x} + C^n \frac{\partial f^n}{\partial \theta} \right) \right]_{i,j} \\ &\quad + \frac{1}{x_i^2 \sin \theta_j} \left[\frac{\partial}{\partial \theta} \left(D^n f^n + E^n \frac{\partial f^n}{\partial x} + F^n \frac{\partial f^n}{\partial \theta} \right) \right]_{i,j}, \end{aligned} \quad (5.69)$$

$$\begin{aligned} \frac{f_{i,j}^{n+1} - f_{i,j}^{n+1/2}}{\Delta\tau/2} &= \frac{1}{x_i^2} \left[\frac{\partial}{\partial x} \left(A^n f^{n+1/2} + B^n \frac{\partial f^{n+1/2}}{\partial x} + C^n \frac{\partial f^{n+1/2}}{\partial \theta} \right) \right]_{i,j} \\ &\quad + \frac{1}{x_i^2 \sin \theta_j} \left[\frac{\partial}{\partial \theta} \left(D^n f^{n+1} + E^n \frac{\partial f^{n+1/2}}{\partial x} + F^n \frac{\partial f^{n+1}}{\partial \theta} \right) \right]_{i,j} \end{aligned} \quad (5.70)$$

The mixed derivative terms are treated explicitly.

Numerical Results

It is known that the alternating direction implicit method is stable and has been used to solve the Fokker-Planck equations. The errors caused by the numerical and analytical approximations at the boundaries are shown in Table 5.3 for two species. The spacing in the x direction is varied from $1/30$ to $1/90$. The errors show that the analytical approximation has reduced the e_∞ errors in both the species. The rms errors are seen to be comparable. This is similar to the results obtained by the Runge-Kutta method.

The results of relaxation of a Gaussian using the alternating direction implicit method are presented in Table 5.4 for two N_θ values (31 and 61). The grid spacing in the x direction is varied from $1/30$ to $1/90$. While there is not a significant difference between $N_\theta = 31$ and 61, a uniform convergent trend is seen with both types of boundary approximations.

Table 5.3: Comparison of errors (percent) with different boundary approximations in the alternating direction method for two species ($\Delta\tau = 1/16$)

N	First species				Second species			
	<u>Numerical</u>		<u>Analytical</u>		<u>Numerical</u>		<u>Analytical</u>	
	e_∞	e_{rms}	e_∞	e_{rms}	e_∞	e_{rms}	e_∞	e_{rms}
31	6.403	2.263	3.207	3.147	3.771	1.879	2.162	1.957
41	2.838	1.174	1.402	1.311	2.368	1.054	1.013	0.858
51	1.611	0.709	0.762	0.686	1.615	0.665	0.560	0.503
61	1.151	0.468	0.490	0.436	1.157	0.453	0.404	0.356
71	0.850	0.329	0.358	0.320	0.856	0.328	0.312	0.282
81	0.641	0.246	0.287	0.261	0.647	0.253	0.261	0.240
91	0.490	0.198	0.247	0.227	0.495	0.209	0.232	0.215

Table 5.4: Relaxation norms for a Gaussian distribution with different boundary approximations ($\Delta\tau = 1/16$)

N	Theta grid points = 31				Theta grid points = 61			
	<u>Numerical</u>		<u>Analytical</u>		<u>Numerical</u>		<u>Analytical</u>	
	L_∞	L_{rms}	L_∞	L_{rms}	L_∞	L_{rms}	L_∞	L_{rms}
31	3.064	1.500	2.407	2.249	2.973	1.451	2.471	2.325
41	1.703	0.915	1.470	1.320	1.544	0.839	1.535	1.397
51	0.973	0.782	1.144	1.027	0.802	0.715	1.211	1.104
61	0.915	0.791	1.031	0.920	0.856	0.739	1.097	0.998
71	0.960	0.830	0.981	0.880	0.904	0.787	1.050	0.957
81	0.997	0.866	0.963	0.865	0.941	0.826	1.033	0.943
91	0.956	0.828	0.960	0.862	0.891	0.781	1.029	0.937

5.5 Background Species and Energy Transfer

In plasmas fast ions which arise out of neutral beam injection and as charged fusion reaction products transfer their energy to the background ions and electrons. In fusion related plasmas the self equilibration time of electrons is of the order of microseconds. Therefore the electron population thermalizes rapidly on a faster time scale compared to the ions. In general the background species, which are at lower temperatures than the high energy species, can be treated as Maxwellian. The interaction between fast ions and the cold ions and electrons (Maxwellian) can be taken into account easily through the Fokker-Planck coefficients as described in Section 2.3.2. This improves the efficiency of computations. The two possible approaches are discussed below.

5.5.1 Fixed Background Species

Two representative runs are shown in Fig. 5.7 for a single fixed background species. Figure 5.7a is shown for the case of fast ion density, $n_D(\text{fast}) = 0.2 n_D(\text{background})$, with an initial fast ion energy of 75 keV. The initial energy of the background ions is 15 keV. The results have been obtained using the 1-D finite element code in the absence of source and loss terms. Since the energy transferred to the cold species is ignored, the fast ions eventually reach the steady state value of 15 keV. A similar run with two fast ion species (deuterons and tritons) with densities $n_D(\text{fast}) = n_T(\text{fast}) = 0.2 n_D(\text{background})$ is shown in Fig. 5.7b. The transfer of energy from the hot species is shown for about 0.5 s.

5.5.2 Energy Transfer between the Species

The temperature of the background species can be modified if the energy transfer rates are known correctly. When arbitrary number of species are modeled the energy transfer rates should be known individually. The rate of energy density gained or lost by the species a due to the collision with species b is equal to the second moment of the Coulomb operator which represents the collision between species a and b (McCoy, Mirin and Killeen, 1981; Killeen, Kerbel, *et al.*, 1986) and is given

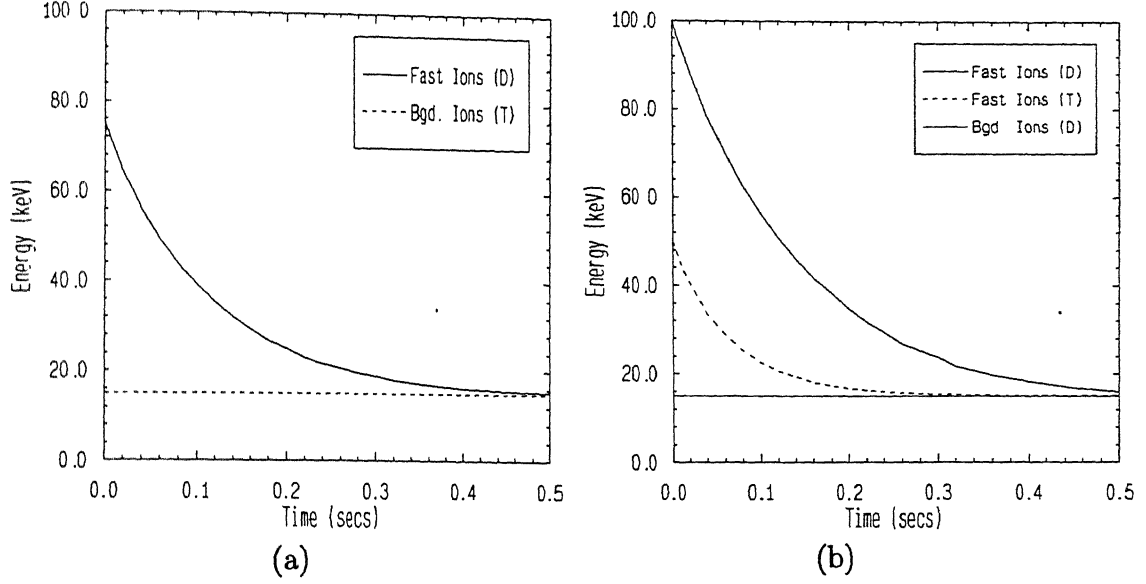


Figure 5.7: Energy loss from a general species in the presence of a fixed background species

by

$$Q_{ab} = \pi m_a \int \int \left(\frac{\partial f}{\partial t} \right)^b v^4 \sin \theta \, dv \, d\theta, \quad (5.71)$$

$$= -2\pi m_a \Gamma_a \int \sin \theta \, d\theta \int G_a^b v \, dv, \quad (5.72)$$

where G_a^b is the corresponding portion of G_a which depends on the species b . G_a is defined in eq. (2.9). The transfer rate in terms of the dimensionless variables is

$$Q_{ab} = -2\pi m_a \Gamma_a C \int_0^\pi \sin \theta \, d\theta \int_0^1 G_a^b x_a \, dx_a, \quad (5.73)$$

where $C = n_a^2 / \bar{v}_a$. \bar{v}_a and n_a are the velocity and density normalization constants of the species a . When both species a and b are isotropic, the above equation reduces

to

$$Q_{ab} = - (4\pi)^2 m_a \left(\frac{\Gamma_a n_a n_b}{\bar{v}_a} \right) \left(\frac{Z_b}{Z_a} \right)^2 \ln \Lambda_{ab} \left[\int_0^1 x dx \left(\frac{m_a}{m_b} N_0(f^b) f_a + \frac{1}{3} \frac{\bar{v}_b}{\bar{v}_a} \left(\frac{E_0(f^b)}{u} + u^2 M_0(f^b) \right) \frac{\partial f_a}{\partial x} \right) \right] \quad (5.74)$$

Further, if the species b is Maxwellian, and the species a is isotropic, then

$$Q_{ab} = - (4\pi)^2 m_a \left(\frac{\Gamma_a n_a n_b}{\bar{v}_a} \right) \left(\frac{Z_b}{Z_a} \right)^2 \ln \Lambda_{ab} \left[\int_0^1 N_0(f^b) \left(\frac{m_a}{m_b} f_a + \frac{T_b}{m_b \bar{v}_a^2} \frac{\partial f_a}{\partial x} \right) dx \right], \quad (5.75)$$

where the functionals M , N , and R are as defined in eqs. (2.56)-(2.59). T_b is the temperature of the species b . It may be noted that when many species are considered in the simulation, calculation of energy transfer rates at each time step would require considerable run time. Provisions have been made in the computer programs to calculate the transfer rates. If only one background species is considered, its energy can be updated easily without the knowledge of the energy transfer rates. Since the energy conservation can be maintained, both in the presence and absence of source and loss terms, through the procedure outlined in Section 3.5.1, the difference in the total energy of the general species can be added to the background species. This has been done particularly to treat electrons as background species, if desired.

Fig. 5.8 illustrates the energy transfer from a general fast ion species to a background species where the energy is updated as explained above. Fast deuterons with a density of $n_D = 0.2 n_T$ sharing their energy with background tritons is shown in Fig. 5.8a. It can be seen that the energies of both the species approach the average value of 25 keV in about 0.5 s. Another typical situation is illustrated in Fig. 5.8b. In this case two general species, deuterons and tritons, are allowed to gain energy from the background deuterons. These results are shown to establish

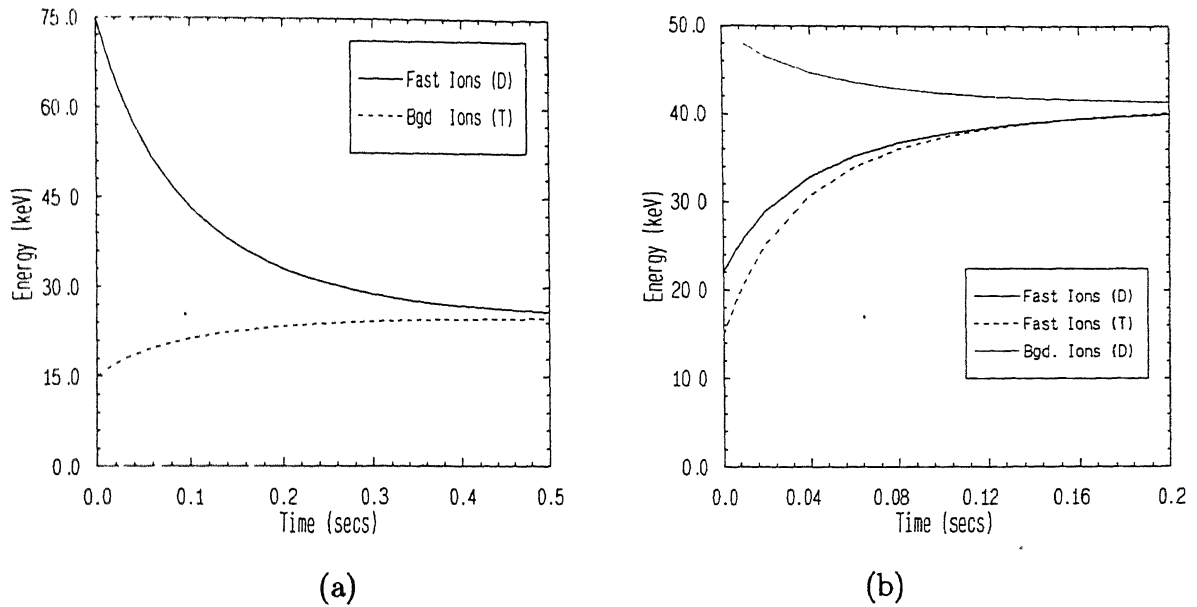


Figure 5.8: Energy transfer between general species and a varying background species

that the models used for the background species adequately and accurately account for the energy exchange.

To study the possibilities of treating electrons as background species, a deuteron-electron plasma was considered with an average energy of 45 keV. Initially the fast ions having 75 keV were allowed to relax their energy with background electrons (15 keV). The energy exchange is shown in Fig. 5.9. The deuterons and electrons are shown in solid and broken lines. The same study was performed treating both electrons and ions as general species. The results are shown as circles and triangles in the same figure. It can be seen that treating electrons as background species may not raise any serious errors in the numerical simulations. This approach will reduce the computation time considerably because the Fokker-Planck equations can be integrated on the ion time scale throughout the evolution.

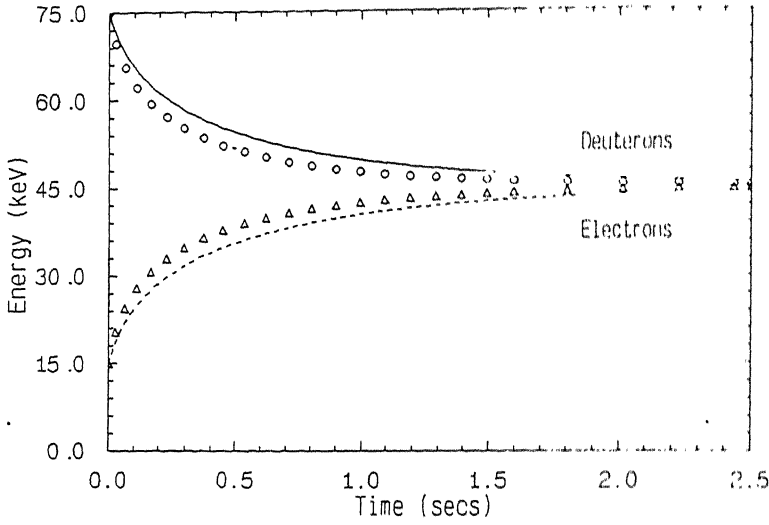


Figure 5.9: Energy transfer between ions and electrons

5.6 Summary

Fokker-Planck equations in 2-D have been solved by the finite element and the finite difference methods. The finite element computational domain is a semi circle and is discretized into a number quadrilateral elements. The equations have been integrated in time by the one step Θ method. The relative performance of the various finite elements has been assessed. Alternating direction implicit method has also been applied in the finite difference method. The main points of the present chapter can be summarized as follows:

- i. Multi-velocity scale Fokker-Planck equation in two dimensions have been solved using five types of quadrilateral elements namely, linear, and complete and incomplete quadratic and cubic finite elements.
- ii. Based on the L_n relaxation measures for Gaussian distribution functions, it is found that the performance of the quadratic and cubic finite elements is better than the linear elements. Further, the incomplete elements are found to compare well with the corresponding complete elements.

- iii. The quadratic elements are preferable among the higher order elements. The problem of numerical oscillations in the case of quadratic elements is much less compared to the cubic elements. For approximately the same computational effort as that for the linear elements, incomplete elements can be used to solve the equations to obtain more accurate results.
- iv. The analytical limits of the collision operator at the boundaries, $x = 0$, and $\theta = 0$ and π , have been implemented for the 2-D Fokker-Planck equations.
- v. Background species with fixed as well as varying temperature have been modeled in the finite element method. Numerical experiments show that the electrons can generally be treated as background species unless the electron distribution is explicitly required.

Chapter 6

Fusion Reactivities and Fast Ion Interactions

6.1 Introduction

As stressed earlier accurate description of plasma behavior requires considerable effort in terms of understanding and modeling. A realistic representation of plasma within the frame work of kinetic models should take into account the various mechanisms that occur in plasmas. Therefore, in addition to the modeling of Coulomb interactions in velocity space using the Fokker-Planck collision operator, other mechanisms/processes should also be included in the simulation. Even though an accurate modeling of the relevant processes may be quite complex, in general representative models can always be used in a broad manner in order to ascertain their impact on the distribution functions of charged species in fusion plasmas.

Shape of the distribution functions of a species is important under non-Maxwellian conditions. Changes in the fusion reactivities due to tail formation, and energy gain or loss are some of the examples which are affected by the actual shape of the distribution functions of the interacting species. Tails are mostly formed due to auxiliary heating and the reaction products. Under such scenarios, the numerical models that describe these processes should be explored fully. This may be achieved by studying/varying the different parameters pertaining to each of the source/sink models considered in the simulation of fusion plasmas.

In this chapter, an improved fusion reaction loss model is presented. Fast ion sources, and particle and energy sinks are also included. Fusion reactivities are calculated in the presence of sources and sinks. The shapes of the distribution functions in some of the transient scenarios are also illustrated.

3.2 Reaction Losses

A general form of the Fokker-Planck equation with source and sinks for each species can be written as

$$\frac{\partial f_a}{\partial t} = \left(\frac{\partial f_a}{\partial t} \right)_c + S_{aF} + S_{aR} - \left(\frac{\partial f_a}{\partial t} \right)_L^P - \left(\frac{\partial f_a}{\partial t} \right)_L^E - \left(\frac{\partial f_a}{\partial t} \right)_L^R, \quad (6.1)$$

where the first term in the right hand side of the above equation is the Fokker-Planck collision term, the second and third terms correspond to fast ion and reaction sources, and the last three terms represent the particle, energy, and reaction sinks. For each species a , the eq. (6.1) is solved with the relevant source and loss terms.

3.2.1 Killeen's Model

The fuel ions in a multispecies plasma deplete due to fusion reactions. The reaction sinks are calculated using the loss coefficient. The loss coefficient for species a due to reaction with species b is denoted by L_{ab} . According to Killeen, Kerbel, *et al.* (1986), L_{ab} is given by

$$L_{ab} = n_b < \sigma v >_{ab}, \quad (6.2)$$

where n_b is the density of the reacting species b , and $< \sigma v >_{ab}$ is the fusion reactivity between species a and b . The above approach is referred as Killeen's model in this work. The reactivity $< \sigma v >$ is defined as

$$< \sigma v >_{ab} = \frac{1}{n_a n_b} \int \int d\mathbf{v} d\mathbf{v}' f_a(\mathbf{v}) f_b(\mathbf{v}') \sigma(u) u, \quad (6.3)$$

where f_a and f_b are the distribution functions, $\sigma(u)$ is the reaction cross section which is a function of the relative velocity u . The above integral can be evaluated easily using the procedures suggested by Marx, Mirin, *et al.* (1976), and Cordey, Marx, *et al.* (1978).

The reaction loss coefficient in eq. (6.2) is independent of energy. This implies that the fraction of particles lost of species a is taken to be constant for all x_a (the dimensionless velocity scale for species a).

6.2.2 Improved Model

In fusion plasmas high energy fuel ions react faster with each other due to higher fusion cross-section. The ions in the high energy region are burnt more due to fusion reactions than the low energy ions. Therefore the losses at all the energy levels need not be uniform. In order to represent the reaction losses more accurately the model given in eq. (6.2) can be improved. An improved model is presented here for this purpose and also implemented in the codes developed in the present work. The reaction losses for the 2-D problems are described in the nondimensional variables by using the loss coefficient

$$L_{ab}(x_a, \theta) = 2\pi n_b \int_0^\infty dx_b x_b^2 \int_0^\pi d\theta_{12} \sin \theta_{12} \int_0^{2\pi} d\phi_{12} f_b(x_b, \theta') \sigma(u) u, \quad (6.4)$$

and in case of 1-D models

$$L_{ab}(x_a) = 4\pi n_b \int_0^\infty dx_b x_b^2 \int_0^\pi d\theta_{12} f_b(x_b) \sigma(u) u \sin \theta_{12} \quad (6.5)$$

where the symbols have their usual meaning. The relative velocity u is written as

$$u = [\bar{v}_a^2 x_a^2 + \bar{v}_b^2 x_b^2 - 2\bar{v}_a \bar{v}_b x_a x_b \cos \theta_{12}]^{1/2}, \quad (6.6)$$

and θ_{12} is the polar angle between the velocity vectors representing x_a and x_b . Here L_{ab} is a function of dimensionless velocity x_a and the integrals on the right hand sides of eqs. (6.4)-(6.5) are evaluated for each value of x_a . For 2-D problems, it also becomes a function of the pitch angle θ .

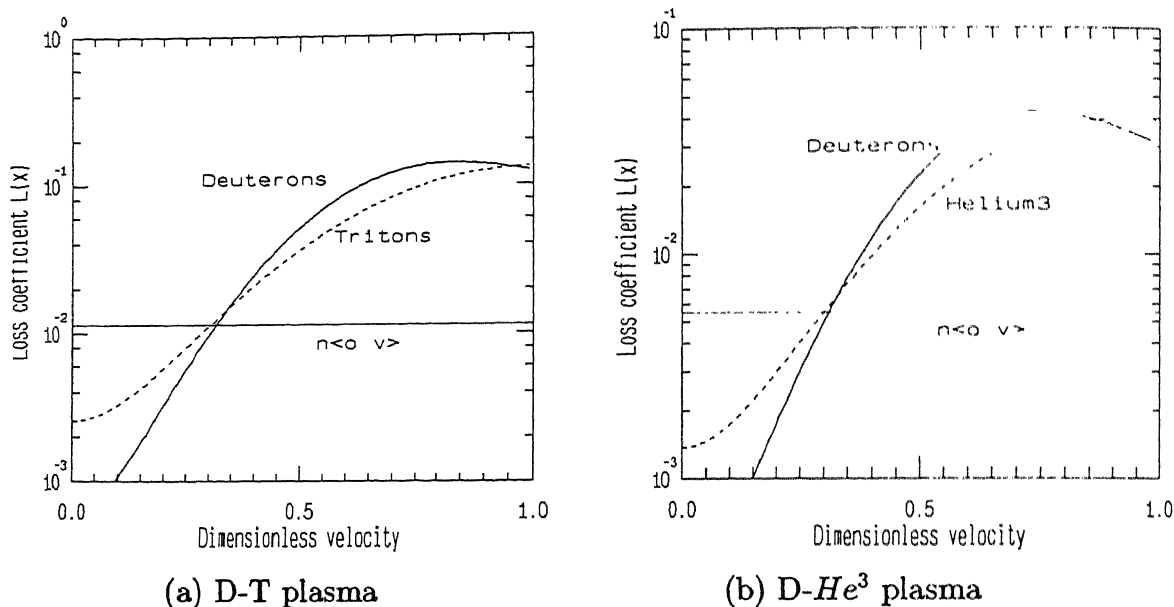


Figure 6.1: Reaction loss coefficients of fuel ions in D-T and D- He^3 plasmas

The loss coefficients L_{ab} are shown in Fig. 6.1 for D-T (15 keV) and D- He^3 (50 keV) plasmas. Densities of the species are 10^{20} m^{-3} ($n_D = n_T = n$). The corresponding $n\langle\sigma v\rangle$ values, as obtained by the Killeen's model (6.2), are also shown in the figure. It is evident from the figures that there will be a significant error if the loss coefficient is taken to be constant over the velocity (shown as $n\langle\sigma v\rangle$ in the figure). The model presented here correctly accounts for the fraction of particles at all energies, which is significantly higher at higher energies, as expected. The loss coefficient shown in Fig. 6.1 was obtained for Maxwellian distributions.

In order to see the effect of the shape of the distribution function on the loss coefficient, distributions with tails are chosen. A typical distribution function with tail is shown in Fig. 6.2. The tail has been introduced artificially. The shape has been modified to appear similar to the one observed elsewhere (Cordey, 1975; Eckert, 1979). The increase in the average (kinetic) temperature due to the tail is less than 10%. The corresponding loss coefficients L_{ab} are shown in Fig. 6.3 for D- and D- He^3 fuel ions. The presence of the tail, while it enhances the reaction rates at the high energy end, does not drastically effect the fractional losses. However

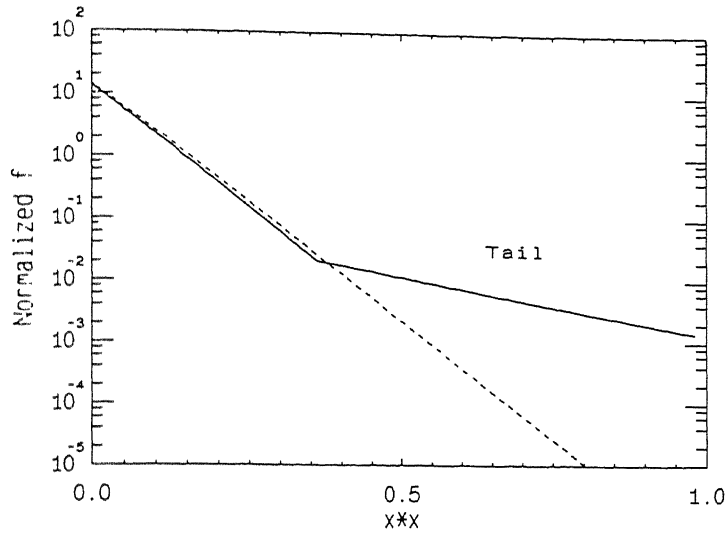


Figure 6.2: Distribution function with a tail

some effect on the fraction of particles lost in the low energy region is clearly visible in the figures. This is due to the interaction between the tail and the slow ions, leading to enhanced burn up slow ions.

In view of the above observations, the reaction loss term included in the Fokker-Planck equation (6.1) is of the form

$$\left(\frac{\partial f_a}{\partial \tau} \right)_L^R = \tau_a \sum_b L_{ab} f_a, \quad (6.7)$$

where the sum over b is for all the relevant reactions, and τ_a is the characteristic time constant for ions.

The impact of the improved reaction loss model on the reactivities is studied with a D-T plasma. For different temperatures, the deuterons and tritons were allowed to react without any other source/sink, over a period of 5.0 s. The results are shown in Table 6.1. The reactivities have been obtained (in units of $m^3 s^{-1}$) using both the Killeen's model and the model presented above. The differences in the reactivities between the two models are presented in terms of a parameter ϵ defined as $\epsilon = (\langle \sigma v \rangle_K - \langle \sigma v \rangle_I) / \langle \sigma v \rangle_I$. Here the subscripts K and I correspond to

Table 6.1: Comparison of fusion reactivities in a D-T plasma as obtained by Killeen's and Improved reaction loss models

T in keV	$t = 1 \text{ s}$			$t = 5 \text{ s}$		
	$\langle \sigma v \rangle_K$	$\langle \sigma v \rangle_I$	ϵ in %	$\langle \sigma v \rangle_K$	$\langle \sigma v \rangle_I$	ϵ in %
5	0.1282e-22	0.1276e-22	0.05	0.9567e-23	0.9370e-23	2.1
10	0.1120e-21	0.1096e-21	2.19	0.1032e-21	0.9288e-22	11.1
15	0.2735e-21	0.2658e-21	2.90	0.2649e-21	0.2302e-21	15.1
20	0.4346e-21	0.4234e-21	2.60	0.4281e-21	0.3771e-21	13.5
25	0.5689e-21	0.5576e-21	2.03	0.5643e-21	0.5121e-21	10.2
30	0.6723e-21	0.6630e-21	1.40	0.6693e-21	0.6255e-21	7.0

where \dot{S} denotes the birth rate of the corresponding fast ions. The distributions of the source ions are denoted by w_d and w_T respectively, and are taken as a highly peaked Gaussian functions, with peaks corresponding to the birth energies of the fast ions.

To study the change in the distribution functions of interacting species in a plasma, the evolution of a deuteron-electron plasma with fast ions (source) is followed for 2 s. This is done by treating the fast ions as a general species but with zero initial density. The ion source is added to this species. The electron population is modified to satisfy the neutrality condition. The electron density is adjusted suitably without changing the average energy of electrons at each time step. The distribution functions are shown in Fig. 6.4 for the fast ions and electrons. The results are given for the fast ion energy of 200 keV and birth rate $0.5 \times 10^{20} \text{ m}^{-3} \text{ s}^{-1}$. The Maxwellian distributions corresponding to the temperatures at 2 s are also shown in the same figure by dashed curves. It can be observed (Fig. 6.4a) that slightly more number of particles are in the low energy region compared to that of Maxwellian, and a slight depletion is at the tail end. If the fast ion source is switched off after 2 s, the Coulomb collisions will eventually bring the species into equilibrium. It may be observed that in general the shapes of the distribution

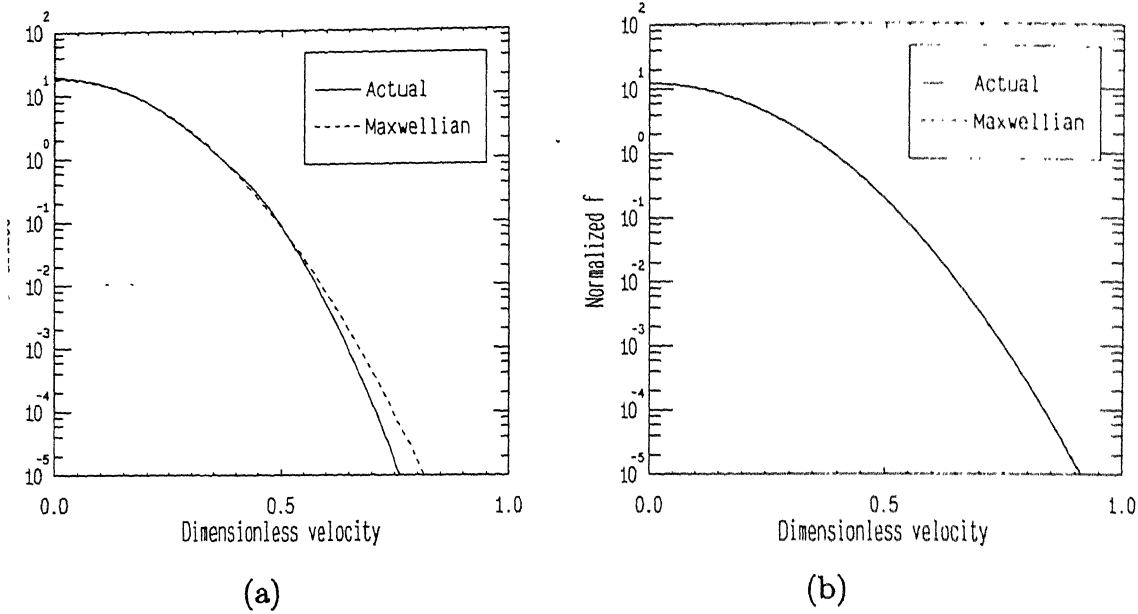


Figure 6.4: Distributions of fast ions and electrons in a D-e plasma

action remain close to Maxwellian after sufficient time.

Figure 6.4b shows the distribution function for electrons. It is evident from the figure that the distribution is not any different from the Maxwellian, which is also shown in the same figure. This is because the electrons interact and thermalize on a shorter time scale compared to the ions. Therefore electrons can as well be treated as a background species. To appreciate this further, the above experiment was repeated for different energies (E_F) of fast ions by treating the electrons as a general background species (see Section 5.5). The results are shown in Table 6.2. It can be seen that both the treatments have shown almost the same results. The distribution function also confirms this (Fig. 6.4b). The net fraction of energy transferred from fast ions to electrons is in the range of 30-35%. These observations suggest that for many applications electrons can be treated as background species, with varying energy.

Table 6.2: Comparison of energies of different species obtained by treating electrons as a general and a background species (Gen-General and Bgd-Background).

t in s	E_F in keV	Deuterons		Fast ions		Electrons	
		Gen	Bgd	Gen	Bgd	Gen	Bgd
1.0	50	14.50	14.15	14.98	14.73	12.46	12.96
	100	24.92	24.38	27.63	27.42	19.05	19.79
	150	35.38	34.66	42.69	42.58	24.64	25.59
	200	45.56	44.62	60.22	60.21	29.48	30.64
2.0	50	19.55	19.41	19.65	19.60	17.74	18.06
	100	35.60	35.81	36.55	36.95	29.37	29.40
	150	52.27	52.96	55.03	56.02	39.47	39.02
	200	69.19	70.46	74.94	76.56	48.39	47.39

6.3.2 Reaction Products

The generation of high energy reaction products is also modeled in the same manner as described in the above section. In a D-T plasma, the D-T and D-D reactions produce respectively 3.52 MeV alphas, and 1.01 MeV tritons and 0.82 MeV He^3 ions as reaction products. The generation rates (birth rates) of alphas and tritons are given by

$$\text{For alphas } \dot{S}_\alpha = n_D n_T \langle \sigma v \rangle_{DT}, \quad (6.9)$$

$$\text{For tritons } \dot{S}_T = 0.5 n_D^2 \langle \sigma v \rangle_{DD}, \quad (6.10)$$

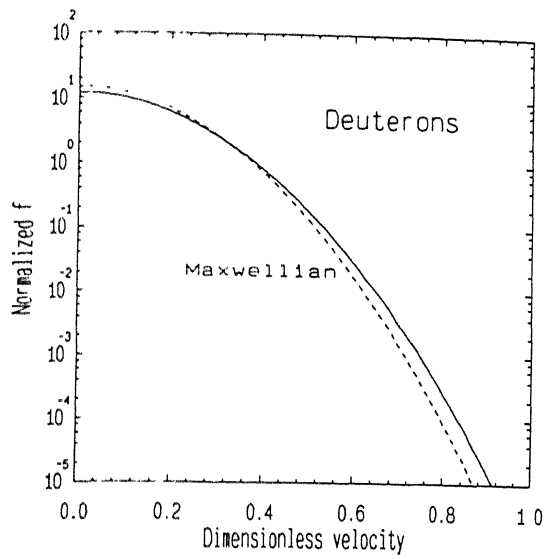
where n denotes the density of respective species. These rates are used in the reaction source term (S_{aR} in eq. (6.1)). The distribution functions w_α and w_T for the reaction products are also modeled as highly peaked Gaussians, as in the case of fast ions.

A simulation experiment was conducted to study the evolution of plasma comprising four general species which include electrons also. The other species are

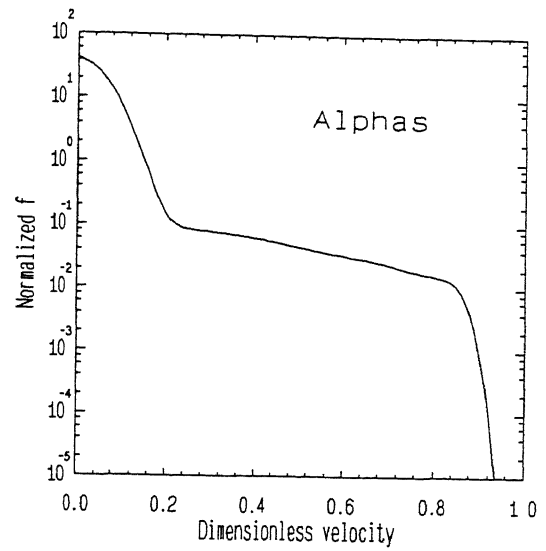
neutrons, tritons, and alphas. All the species are represented on their characteristic velocity scales. Only reaction source for alphas and the loss of fuel ions due to reactions are included in the simulation. Initial density of alphas is taken as 10^{20} m^{-3} . The transient behaviors of deuterons and alphas at 1.5 s are shown in Fig. 6.5. It can be seen that the distribution function of deuterons, denoted by solid line in Fig 6.5a, remains close to Maxwellian. The Maxwellian distribution at the corresponding temperature is shown in the same figure by dashed curve. It may be noted that, compared to the Maxwellian, the population in the high energy region is slightly more indicating a tail like formation. This confirms the fact that high energy reaction products do modify the distribution function in the high energy region, although marginally in this case. The distributions of tritons and electrons are also found to be close to Maxwellian similar to those shown in Fig. 6.5a.

The distribution of alphas at 1.5 s (Fig. 6.5b) shows that beyond a certain velocity range ($v = 0.8\bar{v}_\alpha$), the distribution function falls-off rapidly. Thus, it is equivalent to choose \bar{v}_α just two times the velocity corresponding to the birth energy 3.52 MeV. The figure also indicates that although alphas are born relatively at a very high energy, due to Coulomb interactions some alphas still gain more energy. This is mainly due to $\alpha - \alpha$ interactions. Due to transfer of energy from alphas to other species, the buildup of alphas at low energy is evident from the distribution function.

The change in the fusion reactivity $\langle \sigma v \rangle$ at different times due to alpha heating in the above simulation is shown in Table 6.3. There is a steady increase in the fusion reactivity up to 2 s. The burn up is also shown in the same table for initial density of $n_D = 10^{20} \text{ m}^{-3}$, ($n_D = n_T$). The burn up has gone up to 5% in 2 s due to alpha heating. It can be seen that the fusion reactivity shows decreasing trend at 2 s. This is due to the fact that fuel ions have gained sufficiently high energy by this time and further gain in energy does not lead to increase in reactivity due to the nature of D-T cross-sections. In this simulation, the particle and energy transport mechanisms were not included.



(a)



(b)

Figure 6.5: Distribution functions at 1.5 s in the presence of reaction products

Table 6.3: Increase in the fusion reactivity due to alpha heating in a D-T plasma

time s	$\langle \sigma v \rangle$ $m^3 s^{-1}$	Burn up %
0.171	0.140e-21	0.21
0.266	0.160e-21	0.31
0.485	0.220e-21	0.76
0.775	0.297e-21	1.54
0.972	0.332e-21	2.08
1.529	0.358e-21	3.79
1.937	0.413e-21	5.19
2.000	0.385e-21	5.41

4 Particle Loss

The particle loss term used in eq. (6.1) is of the form (McCoy, Mirin and Killeen, 1981; Matsuura, Nakao and Kudo, 1992),

$$\left(\frac{\partial f_a}{\partial t} \right)_L^R = \frac{f_a}{\tau_P(x)}, \quad (6.11)$$

where $\tau_P(x)$ is the particle confinement time and is velocity dependent. It is given in terms of the dimensionless velocity variable x as

$$\tau_P(x) = \tau_0^P \max[1, cx]^\beta. \quad (6.12)$$

The velocity dependence of the confinement time is achieved by varying the parameter β . τ_0^P can be adjusted to keep the total loss of particles constant (Matsuura, Nakao and Kudo, 1992; Matsuura, Nakao, *et al.*, 1993). The constant c is related to the ratio of the maximum cut-off to the thermal velocity.

For a single species, when confinement time is kept constant, i.e., $\beta = 0$, and only the fast ion source and particle loss terms, the Fokker-Planck equation (6.1) can be integrated to obtain both density and energy. That is, the density at time t is given by

$$n(t) = [n(0) - \tau_P \dot{S}_F] \exp^{-t/\tau_P} + \tau_P \dot{S}_F, \quad (6.13)$$

where $n(0)$ and \dot{S}_F are the initial density and the birth rate of the fast ions respectively. The average energy can be calculated by using

$$E(t) = ([nE(0) - \tau_P \dot{S}_F E_F] \exp^{-t/\tau_P} + \tau_P \dot{S}_F E_F) / n(t), \quad (6.14)$$

where the values at $t = 0$ are specified.

The effect of parameter β is shown in Fig. 6.6. Computational results for a single species are shown for $\beta = 0$ to 4. The fast ions are added to the bulk ions at a rate of $\dot{S} = 0.5 \times 10^{20} \text{ m}^{-3} \text{ s}^{-1}$. The results are shown for $\tau_0^P = 2.0 \text{ s}$. The straight line corresponding to $\beta = 0$ in Fig 6.6a shows that the particle loss is balanced by

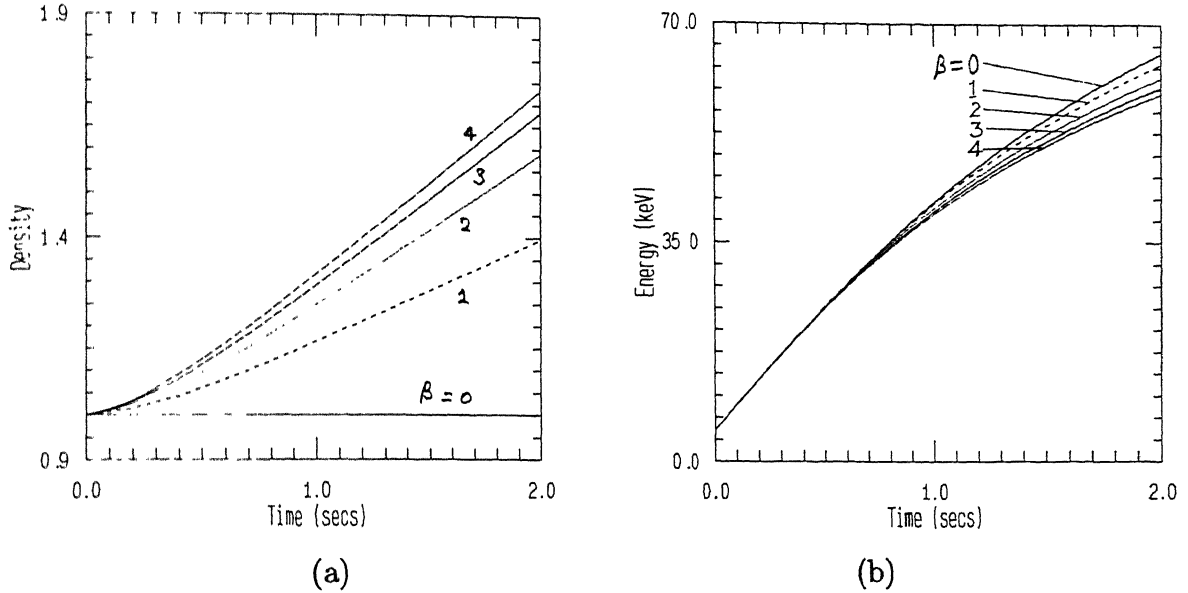


Figure 6.6: Variation in density and energy for a single species with particle sink

the fast ion source, as is evident from eq. (6.13). As β increases, the number of particles lost in the high energy region becomes less compared to the leakage of the low energy particles. This results in a net increase in density as shown in the figure. The average energy of the species is shown in Fig. 6.6b, and shows a relatively less variation with the parameter β .

Single species calculations were also made to observe the shape of the distribution functions during evolution in the presence of particle sinks. A fast ion source with energy $E_F = 200$ keV is added to the bulk deuterons. The results are shown in Fig 6.7 for two cases: (i) fast ion source only (Fig. 6.7a), and (ii) fast ion source and particle sink $\beta = 1$ (Fig. 6.7b). The corresponding Maxwellians are also shown in the same figures by dashed curves. Reactivity calculations performed for a D-T plasma at different temperatures, under the above mentioned conditions, have not shown appreciable differences from those of the corresponding Maxwellian values. Thus if the energy loss term is not included, the effect of the parameter β on the distribution function or the reactivities appears to be small.

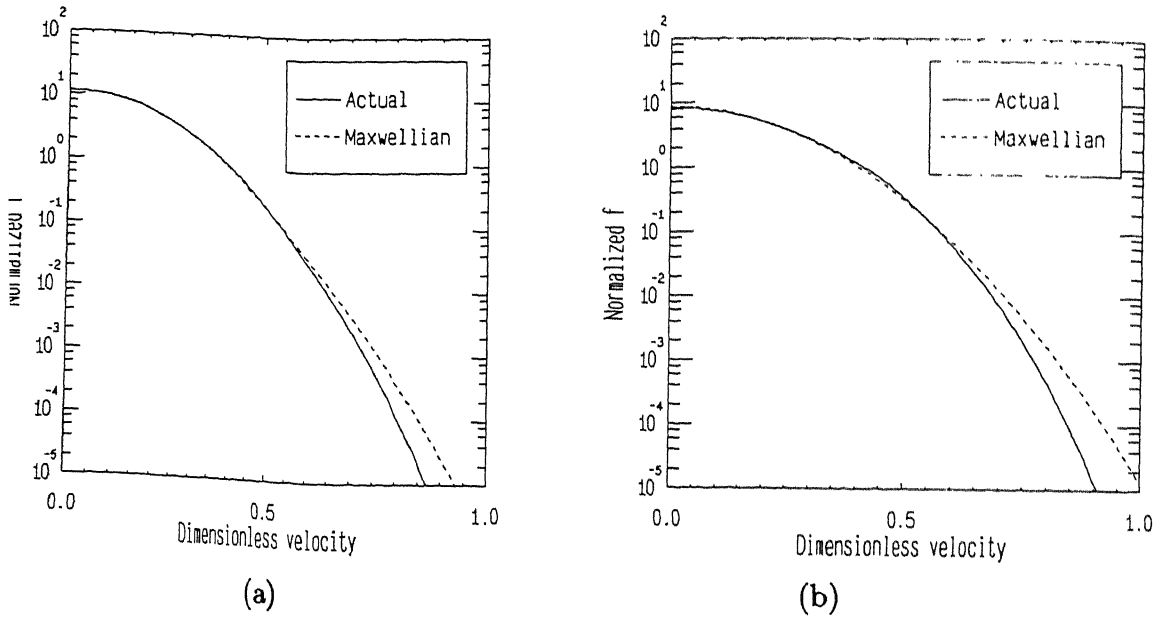


Figure 6.7: Distribution function of deuterons in the presence of particle sink

3.5 Energy Loss

The energy loss term used in the dimensionless velocity variable is given by (Matsuura, Nakao and Kudo, 1992)

$$\left(\frac{\partial f}{\partial t}\right)_L^E = -\frac{1}{x^2} \frac{\partial}{\partial x} \left[\frac{x^2}{2\tau_E(x)} f_a \right], \quad (6.15)$$

where τ_E represents the velocity dependent energy confinement time and is written

$$\tau_E(x) = \tau_0^E \max[1, cx]^\beta. \quad (6.16)$$

β can be adjusted to keep the velocity integrated energy loss constant.

For a single species, the Fokker-Planck equation with fast ion source and particle and energy sinks can be integrated to obtain energy and density for $\beta = 0$.

- i. When fast ion source and only energy sink terms are present:

$$E(t) = ([nE(0) - \tau_E \dot{S}_F E_F] e^{-t/\tau_E} + \tau_E \dot{S}_F E_F) / n(t). \quad (6.17)$$

Here $n(t)$ is the density at time t as obtained in eq. (6.13).

ii. When fast ion source, and both particle and energy sinks are included:

$$E(t) = ([nE(0) - \tau_{eff} \dot{S}_F E_F] e^{-t/\tau_{eff}} + \tau_{eff} \dot{S}_F E_F) / n(t), \quad (6.18)$$

where $n(t)$ is as in eq. (6.13), and τ_{eff} is given by

$$\frac{1}{\tau_{eff}} = \frac{1}{\tau_P} + \frac{1}{\tau_E}. \quad (6.19)$$

The effect of the parameter β on the energy loss in a single species in the presence of fast ion source is shown in Fig. 6.8 for $\tau_P = \tau_E = 2.0$ s. It can be seen that for $\beta > 2$, there is not much change in the average energy of the species. This also does not change the distribution functions appreciably. This fact can be seen from Table 6.4 in which the relative increase in the fusion reactivities for different β 's and also for different E_F 's, the fast ion energies, are given. The relative $\langle \sigma v \rangle$ values are shown in terms of $\langle \sigma v \rangle$ for $\beta = 0$. These values are shown at 1 s and 2 s for two different fast ion energies. It is observed that the enhancement in the reactivity is about 18% for $\beta = 0$ to 2, compared to 1% for $\beta = 3$ to 4. The comparisons of these reactivities with the respective Maxwellian values at the same kinetic temperature indicate negligible differences. This indicates that the fast ions, added to the bulk ions, obtain a distribution close to Maxwellian in 1 to 2 s.

6.6 Summary

An improved reaction loss model which correctly calculates the particle loss due to fusion reactions at different energies has been implemented. Its impact on reactivity at different temperature is shown. The sources and sinks in the simulation studies are fast ion sources including the reaction products, and particle and energy losses. It is found that the high energy fusion product alphas can be represented

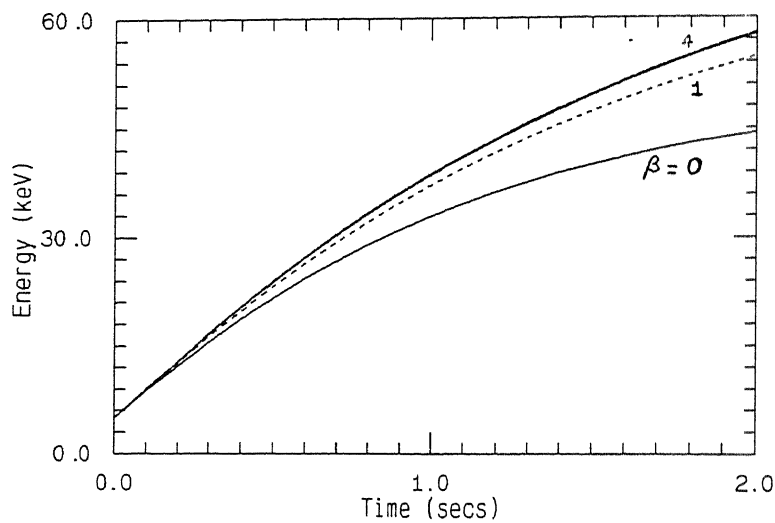


Figure 6.8: Variation in energy of the species (bulk+fast) in the presence of sinks

Table 6.4: Effect of parameter β on $\langle \sigma v \rangle$ in time dependent calculations of D-T plasmas with particle and energy sinks

β	$E_F = 100 \text{ keV}$		$E_F = 150 \text{ keV}$	
	1 s	2 s	1 s	2s
0.0	1.0	1.0	1.0	1.0
1.0	1.144	1.148	1.078	1.050
2.0	1.185	1.181	1.091	1.054
3.0	1.194	1.183	1.092	1.054
4.0	1.193	1.180	1.091	1.053

adequately in the velocity space by choosing a cut-off twice the velocity at their birth energy. The distribution function for alphas indicates that $\alpha - \alpha$ interactions yield some α particles above their birth energy. The simulation studies conducted by treating electrons as a general species also suggest that electrons can be treated as a background species with varying energy. The shapes of the distribution functions and their role in the calculation of fusion reactivities in the presence of velocity dependent loss mechanisms are studied. Generally, the difference in the bulk ion reactivities compared to the corresponding Maxwellian reactivities at the same temperatures is not significant.

Chapter 7

Concluding Remarks

7.1 Summary and Conclusions

In the present work various computational aspects pertaining to the numerical solutions of Fokker-Planck equations have been investigated. The central idea behind this effort is to improve the method of modeling the multispecies fusion plasmas, and also to enhance the accuracy in the computed solutions, where possible. The contributions of the present work are detailed in the following paragraphs:

- The concept of multi-velocity and time scales in Fokker-Planck equations using characteristic velocities and relaxation times for each species has been presented. The dimensionless Fokker-Planck equations and the Rosenbluth potentials in 1-D and 2-D velocity space are given. These equations can be used for an arbitrary number of general and background species. In the case of background species, separate expressions for the coefficients have been arrived at. These equations are solved by the finite element and the finite difference methods, using Crank-Nicolson and fully implicit time stepping schemes.
- One dimensional multi-velocity scale Fokker-Planck equations have been solved by the Galerkin finite element method using linear, quadratic, and cubic elements. It is found that the quadratic and cubic elements perform better than linear elements in terms of computational efficiency and convergence with

mesh refinement and time increment. In the case of 2-D, the equations are solved using five types quadrilateral elements namely, linear, and complete and incomplete quadratic and cubic elements. Based on the relaxation norms for Gaussian distribution functions, it is again concluded that the performance of the quadratic and cubic elements is better as compared to the linear elements. Further, the incomplete elements are found to compare well with the corresponding complete elements. It is seen that for approximately the same computational effort as that for the linear elements, incomplete elements can be used to solve the equations to obtain more accurate results.

- The distribution functions becoming negative (erroneous numerical oscillations) at the tail end has been studied in the multi-velocity scale finite element solutions. It is observed that the choices of the characteristic velocity normalization constants (cut-offs) reduce the numerical oscillations significantly. This fact is more evident from the numerical experiments in which considerable reduction in the negative values was seen when the velocity cut-offs were refined/changed during evolution.
- Electrons have been treated as a general species together with ions. In the multi-velocity scale model, the energy transfer between ions and electrons can be studied using the same number of grid points. The results of Spitzer model which is valid under Maxwellian approximation are found to be in good agreement with the corresponding Fokker-Planck solutions. It may be added that the finite element results show better agreement with the Spitzer model compared to the finite difference method.
- Background species with fixed as well as varying temperature have been modeled in the finite element method. Numerical results indicate that electrons can be treated as background species unless the electrons distribution function is explicitly required. It is observed in the simulation experiments that the transient distribution function of electrons remains close to Maxwellian in general.

- The Fokker-Planck collision operators both in 1-D and 2-D have singularities at the boundaries. The singularities have been removed analytically and the non-singular operators to be applied at the boundaries have been given. These operators have been implemented in both 1-D and 2-D. In case of 2-D it has been implemented both in the Θ -method and the alternating direction implicit method.
- Comparison of the efficiency of the finite element method with the finite difference method indicates that for the same computational effort, the former method performs better than the latter. The experience of using electrons as a general species also supports this as seen in the experiments with Spitzer model.
- In the multi-velocity scale approach the nodes for different species do not correspond to the same physical velocities and interpolations have to be used in the calculation of Rosenbluth potentials for the Fokker-Planck coefficients. In order to improve the accuracy, higher order schemes have been used both for interpolation and quadrature. It is found that the cubic polynomials based Hermite and Lagrangian schemes improve the accuracy in the numerical solutions as compared to the trapezoidal method. The projection errors are seen to be negligible with cubic polynomials.
- In the present work both densities and total energy are conserved exactly during the evolution. This has been achieved by imposing the appropriate constraints in density and energy after each time step or a fixed number of time steps. This avoids the cumulative build up of density and energy errors in the computed solutions.
- Local discretization errors have been computed at each node in the computational domain. It is shown that by suitably relocating a fixed number of nodes, the maximum error can be reduced by an order of magnitude or even more. The reliability of the error estimates used in the grid adaptation is checked against the exact errors where possible.

- A scheme has been presented to accelerate the time marching in the simulation. This scheme is based on the energy error in the computed solution. The results indicate that the number of time steps, and consequently the computational time, can be reduced significantly.
- An improved reaction loss model which correctly calculates the fractional particle loss due to fusion reactions at different energies has been presented. It is seen that there can be appreciable error if the loss coefficient is taken to be a constant as it is done elsewhere. In addition, fast ions sources, reaction products, and sinks represented by velocity dependent particle and energy losses are also implemented in the codes developed.

7.2 Observations and Suggestions

A few observations and suggestions which may be useful in extending the present work are given below:

- In the present work, in solving the 2-D Fokker-Planck equations using the finite element method, the Θ -method has been used. The alternating direction implicit scheme may have some advantages from the viewpoint of computational efficiency and should be tried in the finite element method.
- Moving finite elements in 2-D should be attempted. An infinite element to represent the velocity space beyond the cut-off(s) may also be useful and should be tried.
- In the present work the importance of the convective and diffusive terms in the Fokker-Planck equations has not been studied. This may have some impact on the numerical solutions and it should be studied in detail.
- The Fokker-Planck equations using the velocity variables have been employed in this work. While some work has been reported in the literature using energy as the independent variable, more work is needed to investigate the relative

merits of using the velocity or the energy variable in a multispecies plasma from a computation viewpoint.

- RF heating should be included to study the combined auxiliary heating effectively. Additional source/loss mechanisms/models can be added where needed to improve the accuracy and to make the simulation more realistic.
- The multi-velocity Fokker-Planck equations should be coupled with radial transport models to be able to study the effect of radial transport on heating and current drive in magnetically confined plasmas.

Bibliography

- Altas, I. and Stephenson, J. W. (1991). A two-dimensional adaptive mesh generation method. *Journal of Computational Physics*, **94**:201–224.
- Andrade, A. and Oliphant, T. A. (1981). Solution of Fokker-Planck transport equation by matrix factorization. *Journal of Computational Physics*, **42**:367–381.
- Apostol, T. M. (1962). *Calculus*, volume I. Asia Publishing House, Bombay.
- Arney, D. C. and Flaherty, J. E. (1986). A two-dimensional mesh moving technique for time-dependent partial differential equations. *Journal of Computational Physics*, **67**:124–144.
- BenDaniel, D. J. and Allis, W. P. (1962). Scattering loss from magnetic mirror systems-I. *Plasma Physics (Journal of Nuclear Energy Part C)*, **4**:31–51.
- Berger, M. J. and Olinger, J. (1984). Adaptive mesh refinement for hyperbolic partial differential equations. *Journal of Computational Physics*, **53**:484–512.
- Bickerton, R. J. (1979). Review of the physics of neutral beam injection in tokamaks, in *Heating in toroidal plasmas* (edited by T. Consoli), pages 3–17. Pergamon Press.
- Bing, G. F. and Roberts, J. E. (1961). End-Losses from mirror machines. *The Physics of Fluids*, **4**:1039–1046.
- Bittoni, E., Cordey, J. G. and Cox, M. (1980). The distortion of the thermal-ion distribution during neutral-injection heating. *Nuclear Fusion*, **20**:931–938.

- Bosch, H. S. and Hale, G. M. (1992). Improved formulas for fusion cross-sections and thermal reactivities. *Nuclear Fusion*, **32**:611–631.
- Brebbia, C. A. and Aliabadi, M. H. (1993). *Adaptive finite and boundary element methods*. Computational Mechanics Publications, Southampton and Elsevier Applied Science, United Kingdom.
- Carey, G. F. and Oden, J. T. (1984). *Finite elements: Computational aspects*, volume III. Prentice-Hall, Inc., New Jersey.
- Chang, J. S. and Cooper, G. (1970). A practical difference scheme for Fokker-Planck equations. *Journal of Computational Physics*, **6**:1–16.
- Chong, T. H. (1978). A variable mesh finite difference method for solving a class of parabolic differential equations in one space variable. *SIAM Journal of Numerical Analysis*, **15**:835–857.
- Cordey, J. G. (1975). The distortion of the plasma ion distribution during neutral beam injection heating, in *Plasma Physics and Controlled Nuclear Fusion Research 1974, volume I*, pages 623–632. International Atomic Energy Agency.
- Cordey, J. G., Marx, K. D., *et al.* (1978). A new expansion method for computing $\bar{\sigma}v$ for reactant distribution functions. *Journal of Computational Physics*, **8**:115–121.
- Croyle, J. M., Flaherty, J. E. and Ludwig, R. (1986). On the stability of mesh redistribution strategies for time-dependent partial differential equations. *Journal of Computational Physics*, **62**:26–39.
- Corrington, H. J. and Dalton, C. (1971). Errors in the use of nonuniform mesh systems. *Journal of Computational Physics*, **7**:32–45.
- Ciarra, P. (1992). Iterative schemes and algorithms for adaptive grid generation in one dimension. *Journal of Computational Physics*, **100**:284–293.

- Dawson, J. M., Furth, H. P. and Tenney, F. H. (1971). Production of thermonuclear power by non-maxwellian ions in a closed magnetic field configuration. *Physical Review of Letters*, **26**:1156-1160.
- de Rivas, E. K. (1972). On the use of nonuniform grids in finite-difference equations. *Journal of Computational Physics*, **10**:202-210.
- Denny, V. E. and Landis, R. B. (1972). A new method for solving two-point boundary value problems using optimal node distribution. *Journal of Computational Physics*, **9**:120-137.
- Dhatt, G. and Touzot, G. (1985). *The finite element method displayed*. John Wiley and Sons, New York. translated by G. Cantin.
- Dnestrovskii, Y. N. and Kostomarov, D. P. (1986). *Numerical simulation of plasmas*. Springer-Verlag, Heidelberg, Germany.
- Dwyer, H. A., Kee, R. J. and Sanders, B. R. (1980). Adaptive grid method for problems in fluid mechanics and heat transfer. *AIAA Journal*, **18**:1205-1212.
- Fornberg, B. (1988). Generation of finite difference formulas on arbitrarily spaced grids. *Mathematics of Computation*, **51**:699-706.
- Fornberg, B. (1990). Rapid generation of weights in finite difference formulas, in *Numerical analysis 1989* (edited by D. F. Griffiths and G. A. Watson), pages 105-121. Longman Group UK Ltd., England.
- Fowler, R. H., Smith, J. and Rome, J. A. (1978). FIFPC - A fast ion Fokker-Planck code. *Computer Physics Communications*, **13**:323-340.
- Fowler, T. K. and Rankin, M. (1966). Fusion energy balance in mirror machines. *Plasma Physics (Journal of Nuclear Energy Part C)*, **8**:121-128.
- Fraga, E. S. and Morris, J. L. (1992). An adaptive mesh refinement method for nonlinear dispersive wave equations. *Journal of Computational Physics*, **101**:94-103.

Futch Jr., A. H., Holdren, J. P., *et al.* (1972). Multi-species Fokker-Planck calculations for D-T and D-³He mirror reactors. *Plasma Physics*, **14**:211–244.

Fyfe, D., Weiser, A., *et al.* (1981). A finite element solution of a reduced Fokker-Planck equation. *Journal of Computational Physics*, **42**:327–336.

Gardner, L. R. T., Gardner, G. A. and Zaki, S. I. (1993). Collisional effects in plasmas modelled by a simplified Fokker-Planck equation. *Journal of Computational Physics*, **107**:40–50.

Golias, N. A. and Tsiboukis, T. D. (1993). Adaptive refinement strategies in three dimensions. *IEEE Transactions on Magnetics*, **29**:1886–1889.

Harrison, G. W. (1988). Numerical solution of Fokker-Planck equation using moving finite elements. *Numerical Methods for Partial Differential Equations*, **4**:219–232.

Hassan, O., Probert, E. J., *et al.* (1993). Adaptive finite element methods for transient compressible flow problems, in *Adaptive finite and boundary element methods* (edited by C. A. Brebbia and M. H. Aliabadi), chapter 4. Computational Mechanics Publications, Southampton and Elsevier Applied Science, United Kingdom.

Hawken, D. F., Gottlieb, J. J. and Hansen, J. S. (1991). Review of some adaptive node-movement techniques in finite-element and finite-difference solutions of partial differential equations. *Journal of Computational Physics*, **95**:254–302.

Hively, L. M. (1977). Convenient computational forms for Maxwellian reactivities. *Nuclear Fusion*, **17**:873–876.

Jassby, D. L. (1977). Neutral-beam-driven tokamak fusion reactors. *Nuclear Fusion*, **17**:309–365.

Jassby, D. L. and Towner, H. H. (1976). Fusion reactivities and power multiplication factors of beam-driven toroidal reactors with both D and T injection. *Nuclear Fusion*, **16**:911–924.

- Karney, C. F. F. (1986). Fokker-Planck and quasilinear codes. *Computer Physics Reports*, **4**:183-244.
- Killeen, J. and Futch, A. H. (1968). Numerical solution of the Fokker-Planck equations for a hydrogen plasma formed by neutral injection. *Journal of Computational Physics*, **2**:236-254.
- Killeen, J. and Marx, K. D. (1970). The solution of the Fokker-Planck equation for a mirror confined plasma. *Methods in Computational Physics*, **9**:421-489.
- Killeen, J., Heckrotte, W. and Boer, G. (1962). Energy transfer from hot ions to cold electrons in a plasma. *Nuclear Fusion: Supplement Part*, **1**:183-191.
- Killeen, J., Kerbel, G. D., et al. (1986). *Computational methods for kinetic models of magnetically confined plasmas*. Springer-Verlag, New York.
- Killeen, J., Mirin, A. A. and Rensink, M. E. (1976). The solution of the kinetic equations for a multispecies plasma. *Methods in Computational Physics*, **16**:389-431.
- Larsen, E. W., Levermore, C. D., et al. (1985). Discretization methods for one-dimensional Fokker-Planck operators. *Journal of Computational Physics*, **61**:359-390.
- Lee, D. and Tsuei, Y. M. (1992). A formula for estimation of truncation errors of convection terms in a curvilinear coordinate system. *Journal of Computational Physics*, **98**:90-100.
- Marx, K. D., Mirin, A. A., et al. (1976). Calculation of $(\bar{\sigma}v)_{DT}$ for anisotropic mirror and toroidal distributions. *Nuclear Fusion*, **16**:702-706.
- Matsuda, Y. and Stewart, J. J. (1986). A relativistic multiregion bounce-averaged Fokker-Planck code for mirror plasmas. *Journal of Computational Physics*, **66**:197-217.
- Matsuura, H., Nakao, Y. and Kudo, K. (1992). Ion tail formation and its effect on 14-MeV neutron generation in D-³He plasmas. *Fusion Technology*, **22**:329-333.

- Matsuura, H., Nakao, Y., *et al.* (1993). Effective ion tail formation during startup neutral beam heating in D-³He plasmas. *Fusion Technology*, **24**:17-27.
- McCoy, M. G., Mirin, A. A. and Killeen, J. (1981). FPPAC: A two-dimensional multispecies nonlinear Fokker-Planck package. *Computer Physics Communications*, **24**:37-61.
- McKenzie, J. S., O'Brien, M. R. and Cox, M. (1991). Solution of three-dimensional Fokker-Planck equations for tokamak plasmas using an operator splitting technique. *Computer Physics Communications*, **66**:194-206.
- Mirin, A. A. (1975). HYBRID-II, A two-dimensional multispecies Fokker-Planck computer code. Report UCRL-51615. Rev. 1, Lawrence Livermore National Laboratory.
- Mirin, A. A. and Tomaschke, G. P. (1982). Is fusion reactivity in TFTR affected by distortions of bulk ions from Maxwellians? *Nuclear Fusion*, **22**:1380-1382.
- Mirin, A. A., McCoy, M. G., *et al.* (1988). FPPAC88: A two-dimensional multispecies nonlinear Fokker-Planck package. *Computer Physics Communications*, **51**:373-380.
- Niikura, S. and Nagami, M. (1988). Enhancement of fusion power multiplication factor. *Fusion Engineering and Design*, **6**:109-122.
- Niikura, S. and Nagami, M. (1990). Improvement of fusion reactivity and fusion power multiplication factor in the presence of fast ions. *Fusion Engineering and Design*, **12**:467-480.
- Niikura, S., Nagami, M. and Horiike, H. (1988). Characteristics of fusion reaction rate and neutron yield in deuterium plasma. *Fusion Engineering and Design*, **6**:181-191.
- O'Brien, M. R., Cox, M. and Start, D. F. H. (1986). Fokker-Planck calculations of rf heating in tokamaks. *Computer Physics Communications*, **40**:123-129.

- Prudnikov, A. P., Brychkov, Yu. A. and Marichev, O. I. (1986). *Integrals and series*, volume I. Gordon and Breach Science Publishers, New York.
- Reddy, J. N. (1984). *An introduction to the finite element method*. McGraw-Hill Book Co., Singapore.
- Richtmyer, R. D. and Morton, K. D. (1967). *Difference methods for initial value problems*. Wiley-Interscience Publishing, New York.
- Rosenbluth, M. N., MacDonald, W. M. and Judd, D. L. (1957). Fokker-Planck equation for an inverse-square force. *The Physical Review*, **107**:1-6.
- Roth, J. Reece (1986). *Introduction to fusion energy*. Ibis Publishing, Charlottesville, Virginia.
- Russell, R. D. and Christiansen, J. (1978). Adaptive mesh selection strategies for solving boundary value problems. *SIAM Journal of Numerical Analysis*, **15**:59-80.
- Sanz-Serna, J. M. and Christie, I. (1986). A simple adaptive technique for nonlinear wave problems. *Journal of Computational Physics*, **67**:348-360.
- Schonauer, W., Raith, K. and Glotz, G. (1981). The principle of the difference of difference quotients as a key to the self-adaptive solution of nonlinear partial differential equations. *Computer Methods in Applied Mechanics and Engineering*, **28**:327-359.
- Shoucri, M., Fuchs, V. and Bers, A. (1987). The application of the finite element library TWODEPEP for the numerical solution of the relativistic Fokker-Planck equation. *Computer Physics Communications*, **46**:337-344.
- Shoucri, M., Shkarofsky, I., *et al.* (1989). A quasilinear Fokker-Planck code for the numerical solution of the lower-hybrid current-drive problem in the presence of electron cyclotron heating. *Computer Physics Communications*, **55**:253-268.
- Sigmar, D. J. and Joyce, G. (1971). Plasma heating by energetic particles. *Nuclear Fusion*, **11**:447-456.

Slaughter, D. (1983). Fusion reactivities for several beam and target ion distributions. *Journal of Applied Physics*, **54**:1209–1217.

Spitzer Jr., L (1962). *Physics of fully ionized gases*. Wiley-Interscience Publishers Inc., New York.

Succi, S., Appert, K., *et al.* (1986). Computational models for wave-particle interactions. *Computer Physics Communications*, **40**:137–151.

Tsuji, H., Katsurai, M., *et al.* (1976). Time-dependent solution of Fokker-Planck equation for alpha particles and its effect on alpha-particle heating characteristics in a D-T fusion reactor. *Nuclear Fusion*, **16**:287–293.

Whitney, J. C. (1970). Finite difference methods for the Fokker-Planck equation. *Journal of Computational Physics*, **6**:483–509.

Yasar, O. and Moses, G. A. (1992). Explicit adaptive-grid generation-magnetohydrodynamics. *Journal of Computational Physics*, **100**:38–49.

Appendix A

Legendre Polynomials and their Derivatives

The Legendre polynomials of order up to 8 and their derivatives are listed here. Legendre polynomial of order l , and its n th derivative are denoted by $P_l(\theta)$ and $P_l^n(\theta)$ respectively.

- $l = 0$

$$P_0(\theta) = 1.0$$

$$P_0^1(\theta) = P_0^2(\theta) = P_0^3(\theta) = 0$$

- $l = 1$

$$P_1(\theta) = \cos \theta$$

$$P_1^1(\theta) = -\sin \theta; \quad P_1^2(\theta) = -\cos \theta; \quad P_1^3(\theta) = \sin \theta$$

- $l = 2$

$$P_2(\theta) = (3 \cos 2\theta + 1)/4$$

$$P_2^1(\theta) = (-6 \sin 2\theta)/4$$

$$P_2^2(\theta) = -3 \cos 2\theta$$

$$P_2^3(\theta) = 6 \sin 2\theta$$

• $l = 3$

$$P_3(\theta) = (5 \cos 3\theta + 3 \cos \theta)/8$$

$$P_3^1(\theta) = (-15 \sin 3\theta - 3 \sin \theta)/8$$

$$P_3^2(\theta) = -\frac{1}{8}(45 \cos 3\theta + 3 \cos \theta)/8$$

$$P_3^3(\theta) = (135 \sin 3\theta + 3 \sin \theta)/8$$

• $l = 4$

$$P_4(\theta) = (35 \cos 4\theta + 20 \cos 2\theta + 8)/64$$

$$P_4^1(\theta) = (-140 \sin 4\theta - 40 \sin 2\theta)/64$$

$$P_4^2(\theta) = (-560 \cos 4\theta - 80 \cos 2\theta)/64$$

$$P_4^3(\theta) = (2240 \sin 4\theta + 160 \sin 2\theta)/64$$

• $l = 5$

$$P_5(\theta) = (63 \cos 5\theta + 35 \cos 3\theta + 30 \cos \theta)/128$$

$$P_5^1(\theta) = (-135 \sin 5\theta - 105 \sin 3\theta - 30 \sin \theta)/128$$

$$P_5^2(\theta) = (-1575 \cos 5\theta - 315 \cos 3\theta - 30 \cos \theta)/128$$

$$P_5^3(\theta) = (7875 \sin 5\theta + 945 \sin 3\theta + 30 \sin \theta)/128$$

• $l = 6$

$$P_6(\theta) = (231 \cos 6\theta + 126 \cos 4\theta + 105 \cos 2\theta + 50)/512$$

$$P_6^1(\theta) = (-1386 \sin 6\theta - 504 \sin 4\theta - 210 \sin 2\theta)/512$$

$$P_6^2(\theta) = (-8316 \cos 6\theta - 2016 \cos 4\theta - 420 \cos 2\theta)/512$$

$$P_6^3(\theta) = (49896 \sin 6\theta + 8064 \sin 4\theta + 840 \sin 2\theta)/512$$

• $l = 7$

$$P_7(\theta) = (429 \cos 7\theta + 231 \cos 5\theta + 189 \cos 3\theta + 175 \cos \theta)/1024$$

$$P_7^1(\theta) = (-3003 \sin 7\theta - 1155 \sin 5\theta - 567 \sin 3\theta - 175 \sin \theta)/1024$$

$$P_7^2(\theta) = (-21021 \cos 7\theta - 5775 \cos 5\theta - 1701 \cos 3\theta - 175 \cos \theta)/1024$$

$$P_7^3(\theta) = (147147 \sin 7\theta + 28875 \sin 5\theta + 5103 \sin 3\theta + 175 \sin \theta)/1024$$

• $l = 8$

$$P_8(\theta) = (6435 \cos 8\theta + 3432 \cos 6\theta + 2772 \cos 4\theta + 2520 \cos 2\theta + 1225)$$

$$P_8^1(\theta) = (-51480 \sin 8\theta - 20592 \sin 6\theta - 11088 \sin 4\theta - 5040 \sin 2\theta)/c$$

$$P_8^2(\theta) = (-411840 \cos 8\theta - 123552 \cos 6\theta - 44352 \cos 4\theta \\ - 10080 \cos 2\theta)/c$$

$$P_8^3(\theta) = (3294720 \sin 8\theta + 741312 \sin 6\theta + 177408 \sin 4\theta \\ + 20160 \sin 2\theta)/c$$

where $c = 16384$.

Appendix B

Finite Element Shape Functions

1-D Shape Functions

Shape functions for various 1-D elements are given below (Dhatt and Touzot, 1985):

- *Linear Elements (2 nodes)*

$$\phi_1 = (1 - \xi)/2$$

$$\phi_2 = (1 + \xi)/2$$

- *Quadratic Elements (3 nodes)*

$$\phi_1 = -\xi(1 - \xi)/2$$

$$\phi_2 = (1 - \xi^2)$$

$$\phi_3 = \xi(1 + \xi)/2$$

- *Cubic Elements (4 nodes)*

$$\phi_1 = -(1 - \xi)(1 - 9\xi^2)/16$$

$$\phi_2 = 9(1 - \xi^2)(1 - 3\xi)/16$$

$$\phi_3 = 9(1 - \xi^2)(1 + 3\xi)/16$$

$$\phi_4 = -(1 + \xi)(1 - 9\xi^2)/16$$

2-D Shape Functions

The shape functions ϕ 's for all the five types of quadrilateral elements considered in the present work are listed here (Dhatt and Touzot, 1985; Reddy, 1984). The nodes in each element are numbered as shown in Fig. (5.1). The shape function ϕ_i corresponds to the node i in each type of the finite element.

- *Linear Elements (4 nodes)*

$$\phi_1 = (1 - \xi)(1 - \eta)/4$$

$$\phi_2 = (1 + \xi)(1 - \eta)/4$$

$$\phi_3 = (1 + \xi)(1 + \eta)/4$$

$$\phi_4 = (1 - \xi)(1 + \eta)/4$$

- *Complete Quadratic Elements (9 nodes)*

$$\phi_1 = (1 - \xi)(1 - \eta)\xi\eta/4$$

$$\phi_2 = -(1 - \xi^2)(1 - \eta)\eta/2$$

$$\phi_3 = -(1 + \xi)(1 - \eta)\xi\eta/4$$

$$\phi_4 = (1 + \xi)(1 - \eta^2)\xi/2$$

$$\phi_5 = (1 + \xi)(1 + \eta)\xi\eta/4$$

$$\phi_6 = (1 - \xi^2)(1 + \eta)\eta/2$$

$$\phi_7 = -(1 - \xi)(1 + \eta)\xi\eta/4$$

$$\phi_8 = -(1 - \xi)(1 - \eta^2)\xi/2$$

$$\phi_9 = (1 - \xi^2)(1 - \eta^2)$$

- *Incomplete Quadratic Elements (8 nodes)*

$$\phi_1 = (1 - \xi)(1 - \eta)(1 + \xi + \eta)/4$$

$$\phi_2 = (1 - \xi^2)(1 - \eta)/2$$

$$\phi_3 = -(1 + \xi)(1 - \eta)(1 - \xi + \eta)/4$$

$$\phi_4 = (1 + \xi)(1 - \eta^2)/2$$

$$\phi_5 = -(1 + \xi)(1 + \eta)(1 - \xi - \eta)/4$$

$$\phi_6 = (1 - \xi^2)(1 + \eta)/2$$

$$\phi_7 = -(1 - \xi)(1 + \eta)(1 + \xi - \eta)/4$$

$$\phi_8 = (1 - \xi)(1 - \eta^2)/2$$

- *Complete Cubic Elements (16 nodes)*

$$\phi_1 = N_1(\xi) N_1(\eta)$$

$$\phi_2 = N_2(\xi) N_1(\eta)$$

$$\phi_3 = N_3(\xi) N_1(\eta)$$

$$\phi_4 = N_4(\xi) N_1(\eta)$$

$$\phi_5 = N_4(\xi) N_2(\eta)$$

$$\phi_6 = N_4(\xi) N_3(\eta)$$

$$\phi_7 = N_4(\xi) N_4(\eta)$$

$$\phi_8 = N_3(\xi) N_4(\eta)$$

$$\phi_9 = N_2(\xi) N_4(\eta)$$

$$\phi_{10} = N_1(\xi) N_4(\eta)$$

$$\phi_{11} = N_1(\xi) N_3(\eta)$$

$$\phi_{12} = N_1(\xi) N_2(\eta)$$

$$\phi_{13} = N_2(\xi) N_2(\eta)$$

$$\phi_{14} = N_3(\xi) N_2(\eta)$$

$$\phi_{15} = N_3(\xi) N_3(\eta)$$

$$\phi_{16} = N_2(\xi) N_3(\eta)$$

where

$$N_1(\xi) = -(1 - \xi)(1 - 9\xi^2)/16$$

$$N_2(\xi) = 9(1 - \xi^2)(1 - 3\xi)/16$$

$$N_3(\xi) = 9(1 - \xi^2)(1 + 3\xi)/16$$

$$N_4(\xi) = -(1 + \xi)(1 - 9\xi^2)/16$$

• *Incomplete Cubic Elements (12 nodes)*

$$\phi_1 = 9(1 - \xi)(1 - \eta)\lambda/32$$

$$\phi_2 = 9(1 - 3\xi)(1 - \xi^2)(1 - \eta)/32$$

$$\phi_3 = 9(1 + 3\xi)(1 - \xi^2)(1 - \eta)/32$$

$$\phi_4 = 9(1 + \xi)(1 - \eta)\lambda/32$$

$$\phi_5 = 9(1 + \xi)(1 - 3\eta)(1 - \eta^2)/32$$

$$\phi_6 = 9(1 + \xi)(1 + 3\eta)(1 - \eta^2)/32$$

$$\phi_7 = 9(1 + \xi)(1 + \eta)\lambda/32$$

$$\phi_8 = 9(1 + 3\xi)(1 - \xi^2)(1 + \eta)/32$$

$$\phi_9 = 9(1 - 3\xi)(1 - \xi^2)(1 + \eta)/32$$

$$\phi_{10} = 9(1 - \xi)(1 + \eta)\lambda/32$$

$$\phi_{11} = 9(1 - \xi)(1 + 3\eta)(1 - \eta^2)/32$$

$$\phi_{12} = 9(1 - \xi)(1 + 3\eta)(1 - \eta^2)/32$$

with

$$\lambda = (-10/9 + \xi^2 + \eta^2).$$

Gauss Points and weights

Gauss points ξ_k and their corresponding weights w_k used for numerical integration in the finite element method are given in Table B.1. The Gauss points and weights are given for different number of points N .

Table B.1: Gauss points and weights

N	ξ_k	w_k
4	-0.86113631159405	0.34785484513745
	-0.33998104358486	0.65214515486255
	0.33998104358486	0.65214515486255
	0.86113631159405	0.34785484513745
5	-0.90617984593866	0.23692688505619
	-0.53846931010568	0.47862867049937
	0.0	0.56888888888889
	0.53846931010568	0.47862867049937
	0.90617984593866	0.23692688505619
6	-0.93246951420315	0.17132449237917
	-0.66120938646626	0.36076157304814
	-0.23861918608320	0.46791393457269
	0.23861918608320	0.46791393457269
	0.66120938646626	0.36076157304814
	0.93246951420315	0.17132449237917

